Journal of Magnetic Resonance **155,** 157–216 (2002)
doi:10.1006/jmre.2001.2341, available online at http://www.idealibrary.com on IDEAL®

ADVANCES IN MAGNETIC RESONANCE

Nuclear Magnetic Resonance of Laser-Polarized Noble Gases in Molecules, Materials, and Organisms

Boyd M. Goodson[1]

Materials Sciences Division, Lawrence Berkeley National Laboratory and Department of Chemistry, University of California, Berkeley, California 94720-1460

Received May 15, 2000

The sensitivity of conventional nuclear magnetic resonance (NMR) techniques is fundamentally limited by the ordinarily low spin polarization achievable in even the strongest NMR magnets. However, by transferring angular momentum from laser light to electronic and nuclear spins, optical pumping methods can increase the nuclear spin polarization of noble gases by several orders of magnitude, thereby greatly enhancing their NMR sensitivity. This review describes the principles and magnetic resonance applications of laser-polarized noble gases. The enormous sensitivity enhancement afforded by optical pumping can be exploited to permit a variety of novel NMR experiments across numerous disciplines. Many such experiments are reviewed, including the void-space imaging of organisms and materials, NMR and MRI of living tissues, probing structure and dynamics of molecules in solution and on surfaces, NMR sensitivity enhancement via polarization transfer, and low-field NMR and MRI. © 2002 Elsevier Science (USA)

Contents.

I. INTRODUCTION

The phenomenon of nuclear magnetic resonance (NMR) is the basis for many of the most powerful analytical tools in the spectroscopist's arsenal. Over the 55-year history of its study, countless NMR techniques have been developed to permit, for example, the detailed study of structure and dynamics of molecules in solution, the characterization of the bulk and surface properties of materials, and the noninvasive imaging of tissues in living organisms. However, conventional NMR methods suffer from a common drawback that in many circumstances can limit their power and applicability—a notorious lack of sensitivity. This fundamental insensitivity originates from the miniscule size of nuclear magnetic moments, which results in an exceedingly small equilibrium nuclear spin polarization in even the largest magnets.

In certain systems, however, the sensitivity of NMR spectroscopy and magnetic resonance imaging (MRI) can be greatly enhanced via optical pumping. With optical pumping, angular momentum is transferred from laser photons to electronic and nuclear spins, thereby temporarily enhancing the nuclear spin polarization in these systems by four to five orders of magnitude.

This review[3] surveys the field of optically pumped NMR (OPNMR) using "laser-polarized" noble gases, from its inception

[1] Current address: NSF Laboratory for Molecular Sciences and Department of Chemistry, A. A. Noyes Laboratory, California Institute of Technology, Pasadena, CA 91125.

Permanent address (post August 2002): Department of Chemistry, Neckers Hall, Illinois University, Carbondale, IL 62901-4409.

[3] Portions of this review were presented previously in Refs. (*1, 2*).

1090-7807/02 $35.00
© 2002 Elsevier Science (USA)
All rights reserved.

roughly 10 years ago, to the present (May 2000; see Note added in proof). However, space does not permit a detailed description of all of the work that has been performed in this growing field; instead, examples from the Berkeley laboratory and elsewhere are highlighted that demonstrate the promise of various novel approaches. Additionally, while general knowledge of NMR principles and techniques is assumed, portions of NMR theory and experiment that are particularly relevant to the material presented in this review will be described later within the context of such work. When greater depth into NMR and MRI theory and practice is required, the reader is directed to Refs. (*3–11*) for a selection of NMR books and monographs.

This review is organized as follows. In Sections II and III, relevant portions of theoretical and experimental aspects of OPNMR and the properties of laser-polarized noble gases are briefly reviewed. Sections IV and V are concerned with using laser-polarized xenon to probe structure and dynamics of molecules in solution. Of particular interest is the so-called spin polarization-induced nuclear Overhauser effect (SPINOE). The SPINOE can result in polarization transfer from laser-polarized xenon to solution species, thereby enhancing their NMR signals in a manner dictated by the relative distance and dynamics between xenon and the molecules under study.

Sections VI and VII describe how laser-polarized gases can be used to characterize materials via a number of imaging and spectroscopic techniques, including enhanced ^{129}Xe NMR spectroscopy of porous materials and surfaces, polarization transfer to surface spins via SPINOE and cross-polarization, studies of boundary restricted diffusion, void-space imaging, and the visualization of flow through porous materials.

Section VIII presents selected work from the fastest growing segment of the OPNMR field: the application of laser-polarized gases for biomedical and clinical studies. Following a description of *in vivo* void-space imaging, recent studies using laser-polarized gases to probe living tissues will be presented. The ninth and final section of this work describes low/zero-field experiments permitted by the inherent nonequilibrium nature of the gases' laser-induced polarization, providing one of the most promising future directions of this exciting field.

II. OPTICAL PUMPING OF NOBLE GASES

A. Introduction

Consider a collection of spin $I = 1/2$ nuclei with polarization, P, given by

$$P = \frac{N_\uparrow - N_\downarrow}{N_\uparrow + N_\downarrow}, \qquad [1]$$

where $N_\uparrow$ and $N_\downarrow$ are respectively the numbers of spins in the $m_I = 1/2$ and $m_I = -1/2$ states. The magnitude of the observable magnetization $\mathbf{M}_0$ is proportional to P,

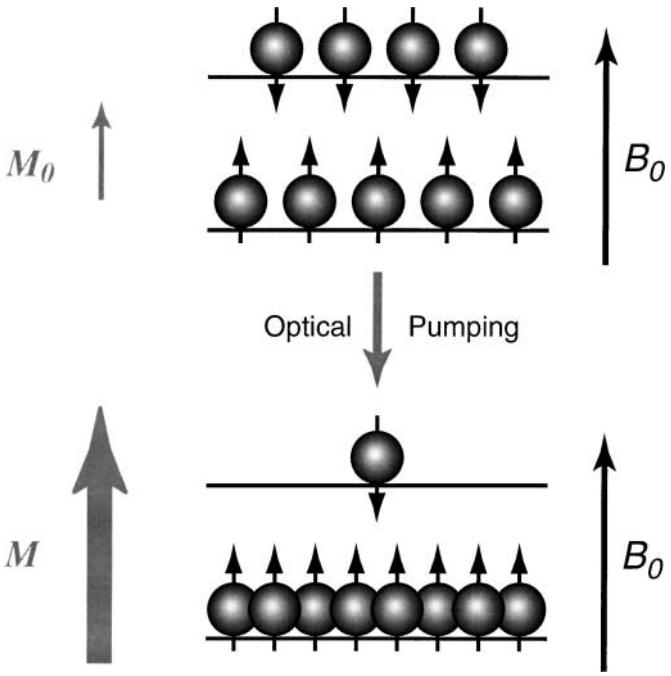

FIG. 1. Cartoon depicting the effect of laser-polarization for a collection of spin-1/2 nuclei (assuming positive gyromagnetic ratio). Normally, the number of spins aligned antiparallel to the magnetic field (B_0) is nearly equal to the number of spins aligned with B_0, leading to a tiny detectable magnetization, M_0. However, with optical pumping the population distribution of the spins can be driven far away from equilibrium, thereby increasing the magnetization to order unity. Figure adapted from Ref. (*12*).

$$M_0 = \frac{1}{2} N_s \gamma \hbar P, \qquad [2]$$

where N_s is the number nuclear spins and γ is the gyromagnetic ratio. If the ensemble is at thermal equilibrium with a strong external magnetic field of magnitude B_0 and at temperature T (as shown in the top portion of the cartoon in Fig. 1), the functional form of P is given by

$$P = \tanh\left(\frac{\gamma \hbar B_0}{2kT}\right), \qquad [3]$$

where k is Boltzmann's constant.

Because of the relative weakness of nuclear magnetic moments, it is generally true that $\gamma \hbar B_0 / kT \ll 1$, yielding

$$P \approx \frac{\gamma \hbar B_0}{2kT}. \qquad [4]$$

For example, Eq. [4] gives $P \approx 3.2 \times 10^{-5}$ for a collection of protons at room temperature in a field of 9.4 T. Naturally, the polarization would be even lower for samples in the weaker fields used in most medically related experiments, or when observing

nearly all other NMR-active nuclei. Thus, according to Eqs. [2]–[4] improving the equilibrium magnetization for a given sample can be performed only by increasing B_0 (which grows progressively expensive and difficult), or by drastically lowering T (inappropriate for various types of samples, especially living organisms).

Instead, a different approach would be to achieve high nuclear polarization by some *nonequilibrium* means, even if the polarization would eventually succumb to spin–lattice relaxation. If useful experiments can be performed faster than such relaxation occurs, it may well be worth the trouble to "beat" Boltzmann, even if only for a short time.

Optical pumping methods can be utilized to obtain highly nonequilibrium nuclear spin polarizations, thereby increasing M by four to five orders of magnitude (shown in the bottom portion of Fig. 1). Optical pumping methods achieve highly non-Boltzmann population distributions by exploiting the quantum mechanical selection rules of angular momentum. For an in depth introduction into the physics of optical pumping in general, the reader is directed to the monograph of Bernheim (*13*).

It was first shown by Kastler (*14–16*) that circularly polarized light could be used to pump *electronic* spins of gaseous metal vapors into nonequilibrium population distributions, an accomplishment which earned him the Nobel Prize. Later work (*17, 18*) showed that the *nuclear* spin polarization of noble gases present as buffer gases in the pumping cell could be greatly enhanced through collision and spin exchange with electronically spin-polarized alkali atoms. This process has since been studied in considerable detail by Happer and co-workers (see, for example, Refs. (*19–21*)), with one original motivation being the creation of spin-polarized targets for particle physics experiments. A second method for optically pumping helium directly called metastability exchange has also been developed (*22–25*). Metastability exchange does not require the presence of alkali metal atoms, is only useful to optically pump helium.

It should be mentioned that the NMR signals of other systems besides gas-phase monatomic species have been successfully enhanced through optical pumping. For example, the optical pumping of nuclear spins in certain semiconductors (e.g., GaAs and InP) has permitted a variety of novel studies of these materials, most notably the use of optical pumped semiconductor quantum wells to study the effects of reduced dimensionality on the fundamental behavior of electrons within these structures (for review, see Refs. (*26, 27*). Semiconductor OPNMR has yet to see wider application to other fields (although the potential for using optically pumped semiconductor wafers as substrates for polarization transfer to species (e.g., proteins and other biological molecules of interest) adsorbed upon their surfaces has recently been discussed (*28*). High polarization can also be achieved by immersing substances with favorable relaxation characteristics (like noble gases) in high magnetic fields and at ultra-low cryogenic temperatures for extended periods of time; the highly polarized substance could then be warmed and subsequently transferred to NMR samples for study. This approach has also been the subject of recent work (*29, 30*), but is beyond the scope of this review.

B. Alkali Metal Spin Exchange

Alkali metal spin exchange is a robust method for generating optically pumped noble gases, capable of achieving moderate to high levels of nuclear spin polarization in both xenon and helium under a wide range of conditions (e.g., temperature, gas pressure, and field strength). For a recent review of alkali metal spin exchange optical pumping, see Ref. (*21*).

The two-step process that comprises alkali metal spin exchange is shown schematically in Fig. 2. In the first step, the spins of unpaired electrons of alkali metal atoms are polarized with laser light (Fig. 2a). By applying circularly polarized light tuned to the D_1 transition of the alkali metal (e.g., 794.7 nm for Rb), population can be selectively depleted from one of the m_J sublevels in the ground state (neglecting the hyperfine coupling with the nuclear spin of the metal); as shown in Fig. 2a, σ^+ light drives population from $m_J = -1/2$ in the ground state into $m_J = 1/2$ in the excited state. Collisions with other gas-phase species equalize the populations of the excited-state sublevels, equilibrating the relaxation rates to the ground m_J sublevels. The depletion of the ground $m_J = -1/2$ sublevel (and subsequent accumulation of population in the ground $m_J = 1/2$ sublevel) rapidly reaches steady state, leaving the metal vapor electronically spin-polarized.

Often, nitrogen is added to the gas mixture to quench the fluorescence of the electronically excited alkali metal atoms, which would otherwise work to depolarize the electron spins. The probability for radiative decay for the electronically excited Rb is given by the branching ratio, w_γ (*31*),

$$w_\gamma \approx \frac{3}{3 + 7.5\frac{p_{N_2}}{\text{kPa}}}, \qquad [5]$$

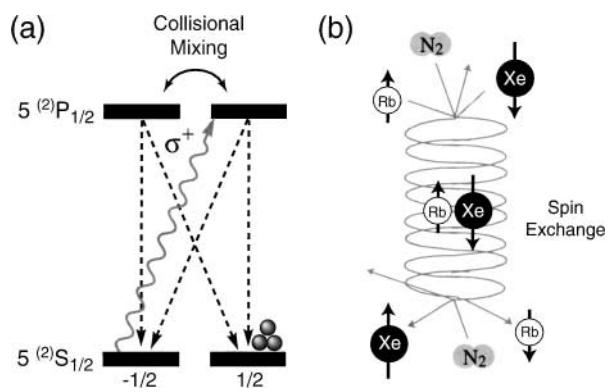

FIG. 2. Cartoons of the alkali-metal optical-pumping/spin-exchange processes (after Ref. (*20*)). (a) Optical pumping of the electronic spins of the alkali atoms (neglecting the hyperfine ($F = I + J$) couplings between the electronic and nuclear spins of the alkali metal atom). (b) Polarization of the xenon nuclei via collision and spin exchange.

where p_{N_2} is the partial pressure of nitrogen at 300 K. Thus, a nitrogen partial pressure of about 40 kPa would give, $w_\gamma \approx 0.01$.

In the second step of the optical pumping process (Fig. 2b), collisions between unpolarized noble gas atoms and electronically spin-polarized alkali metal atoms permit spin exchange via Fermi-contact hyperfine interactions between the electron spins (S) and the noble gas nuclear spins (I) (*32*),

$$\alpha \mathbf{S} \cdot \mathbf{I} = \frac{\alpha}{2}[S_+ I_- + S_- I_+] + \alpha S_z I_z, \qquad [6]$$

where the "flip-flop" term in brackets gives the spin exchange between the alkali metal and the noble gas, and the coupling constant α is proportional to the probability of finding the unpaired electron of the alkali atom at the nucleus of the noble gas atom, and is given by

$$\alpha = \frac{8\pi}{3}\gamma_S \gamma_I \hbar^2 \delta(r); \qquad [7]$$

here $\delta(r)$ is the Dirac delta function depending upon the relative distance between the electron and the nucleus.

The collisions may be three-body (as shown in the figure, with nitrogen molecules participating in the formation and destruction of the complex) or two-body in nature, depending on the species and experimental conditions involved. However, the overall spin exchange may be effectively treated as a two-body process under conditions typically encountered for NMR applications (*21*). The nuclear polarization P of the noble gas after a given duration of optical pumping (t) is governed by the relation

$$P = \frac{\rho_{SE}}{\rho_{SE} + \rho_o} P_{\mathrm{Rb}}\left[1 - e^{-(\rho_{SE}+\rho_o)t}\right], \qquad [8]$$

where P_{Rb} is the electron spin polarization of the Rb, ρ_{SE} is the rate of spin exchange between the noble gas nuclei and the rubidium electrons, and ρ_o contains all other contributions to the longitudinal relaxation of the noble gas nuclei (e.g., wall collisions). P_{Rb} is determined by

$$P_{\mathrm{Rb}} = \frac{\rho_{OP}}{\rho_{OP} + \rho_{SD}}, \qquad [9]$$

where ρ_{OP} is the rate at which the Rb electronic state becomes spin polarized via optical pumping, and ρ_{SD} is the "spin-destruction" rate, or spin-relaxation rate of the alkali metal atoms. Near the walls of the pumping cell P_{Rb} drops to zero, as the residence time of the alkali metal atoms is long enough to permit significant depolarization. Under normal optical pumping conditions far from the walls of the pumping cell, ρ_{SD} results mostly from collisions between Rb and gas atoms in the pumping cell. ρ_{SE} is proportional to the alkali atom density,

$$\rho_{SE} = \kappa_{SE}[\mathrm{Rb}], \qquad [10]$$

where the proportionality constant, κ_{SE}, is the spin-exchange cross section. Over time (seconds to hours, depending upon the experimental conditions), the nuclear polarization of the noble gas will accumulate, yielding values as high as several tens of percent.

The enhanced polarization can be calibrated with a variety of methods (see, for example, Refs. (*21, 33*)). The signal enhancement generated with optical pumping is trivially calculated from the polarization (or vice versa); for ^{129}Xe polarized to 10%, the enhancement is ≈11,000 compared to ^{129}Xe at equilibrium in a 9.4-T magnet at room temperature.

C. Metastability Exchange

An alternative method for producing laser-polarized helium directly (i.e., without the need for an alkali vapor intermediary) known as metastability exchange was developed soon after alkali metal spin exchange was first observed (*22*). The process of metastability exchange optical pumping is shown schematically in Fig. 3. Before the helium gas can be optically pumped, a small portion of the gas must first be excited from the ground electronic

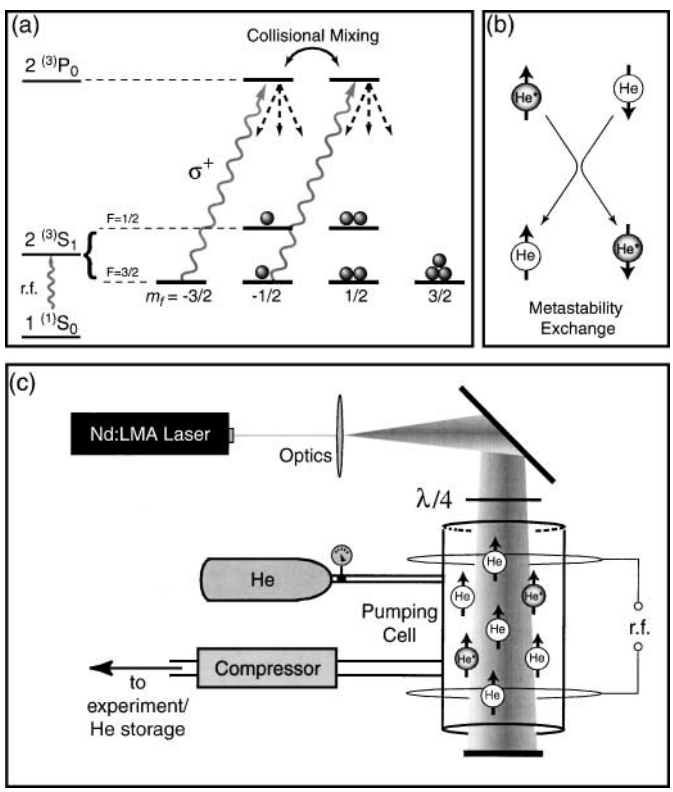

FIG. 3. Metastability exchange. (a) Cartoon showing the relevant energy levels involved in the creation and subsequent nuclear spin polarization of metastable helium-3 gas (after Ref. (*23*)). (b) He*–He collisions permitting energy-conserving metastability exchange. (c) Schematic showing relevant portions of a metastability exchange optical pumping apparatus. The weak external magnetic field, *in situ* polarization calibration equipment, and the details of the helium compressor have been omitted (for more details, see Refs. (*23*, *24*)).

state (1^1S_0) into the metastable state $2\,^3S_1$; this is achieved by applying a weak RF discharge to the optical pumping cell (*23*). Metastable atoms can then be optically pumped by absorbing circularly polarized laser light tuned to the C_8/C_9 lines (1083 nm), which drives population from the $2\,^3S_1$ ($F = 1/2$) level (via C_8) or the $2\,^3S_1$ ($F = 3/2$) level (via C_9) to the $^3P_0$ ($F = 1/2$) level. For example, as shown in Fig. 3a, σ^+ light hitting the C_9 line would selectively drive population from $m_F = -3/2$ $(-1/2)$ in the $2\,^3S_1$ state into $m_F = -1/2$ $(1/2)$ in the $^3P_0$ state, thereby conserving angular momentum.

Collisions effectively mix the $^3P_0$ m_F levels, and the populations in these sublevels relax via isotropic spontaneous emission distributed across all the emission lines. Subsequent optical pumping of the $2\,^3S_1$, $F = 3/2$ level further depletes the $m_F = -3/2, -1/2$ sublevels, leaving the metastable atoms in a highly polarized state. Thus in metastability exchange optical pumping, nuclear spin polarization is achieved via efficient hyperfine coupling between the electronic and nuclear spins of metastable atoms. However, as with alkali metal spin exchange, collisions are still necessary to produce laser-polarized helium. Spin-polarized ground state helium atoms are created via angular momentum-conserving metastability exchange collisions between oriented metastable atoms and disoriented ground-state atoms (Fig. 3b); for example,

$$^3\mathrm{He}\left(m_F = -\frac{1}{2}\right) + {}^3\mathrm{He}^*(m_F') \rightarrow {}^3\mathrm{He}^*(m_F' - 1) + {}^3\mathrm{He}\left(m_F = \frac{1}{2}\right). \qquad [11]$$

Thus, the products of such a collision are a ground-state helium atom with a spin-polarized nucleus and a depolarized metastable atom. The depolarized metastable atom can then absorb a photon of circularly polarized light to sustain the optical pumping process.

D. Experimental Methods

1. Metastability Exchange Apparatus

A simplified schematic of a metastability exchange optical pumping apparatus is shown in Fig. 3c. A high-power (multi-Watt) $La_{0.85}Nd_{0.15}MgAl_{11}O_{19}$ (Nd:LMA) laser produces 1083-nm light that is expanded with optics and becomes circularly polarized by passing through a quarter-wave plate. This laser light then passes into the optical pumping cell containing a small amount of ^{3}He gas. The cell is placed in a homogeneous external magnetic field of a few Gauss (not shown). The RF coils induce the discharge needed to create the metastable atoms. The cell may be closed, or may incorporate a supply line from a helium reservoir with subsequent collection of the polarized helium with a compressor.

While not as commonly implemented as alkali metal spin exchange, recent technological advancements have drawn increasing interest towards using metastability exchange to produce significant quantities of laser-polarized helium. The greatest advantage of this technique is that the spin exchange rate is about 20,000 times greater than that obtained between helium and rubidium in alkali-metal spin exchange (*23*). This high rate of polarization transfer permits a helium spin polarization of ~60% to accumulate in about 1 minute in a closed cell (several hours are required to pump helium to such polarizations using alkali metal spin exchange). However, two disadvantages (other than that the technique is limited to producing laser-polarized helium) must be mentioned: (1) high-powered sources of 1083-nm laser-light are not currently as readily available as the ubiquitous sources of 795-nm light needed to pump Rb; and (2) the relatively low pressure of helium that must be maintained in the cell in order to obtain efficient optical pumping can complicate the production of enough laser-polarized helium to perform most desired NMR experiments.

The density of helium gas in the pumping cell is chosen to optimize two opposing effects: the pressure must be low enough to maintain the metastable state, but high enough to give a sufficient optical density of metastable atoms. Best results have been achieved using helium pressures of ~1 torr (*23*). The density of metastable atoms is typically on the order of $\sim 10^{10}$/cc (or about 1 ppm). Because only a very small amount of laser-polarized helium is present in the optical pumping cell at any given time (a limitation which can be partially mitigated by using large pumping cells), one must implement some kind of compression and storage apparatus in order to create the large quantity of laser-polarized helium required for most medical imaging experiments. Moreover, such a compressor must be comprised of materials that are completely free of paramagnetic centers in order to prevent the high polarization from being lost prematurely to relaxation. The state-of-the-art metastability exchange OP apparatus at Mainz, carefully constructed in light of the unique requirements of metastability exchange, can produce ~0.5–1 L/h of laser-polarized helium with a nuclear spin polarization approaching 50% (even higher polarization values can be reached with lower polarized helium volume rates) (*25*).

Finally, recent work has been directed toward the development of a simpler, less-expensive metastability exchange OP apparatus that offers greater flexibility and portability (*34*). In the new NIST design the polarized helium compressor and gas recirculation apparatus can fit within a 30 × 30 × 30-cm cube. This apparatus is capable of producing 15% polarized helium at a rate of ~1 L/h.

2. Alkali Metal Spin Exchange: The Batch Optical Pumping Apparatus

There are several variants of the experimental setups used for optically pumping noble gases via alkali metal spin exchange; however, these methods usually fall within one of two categories. The first, which will be referred to as the "batch" method, is shown in Fig. 4; the particular optical pumping setup shown in

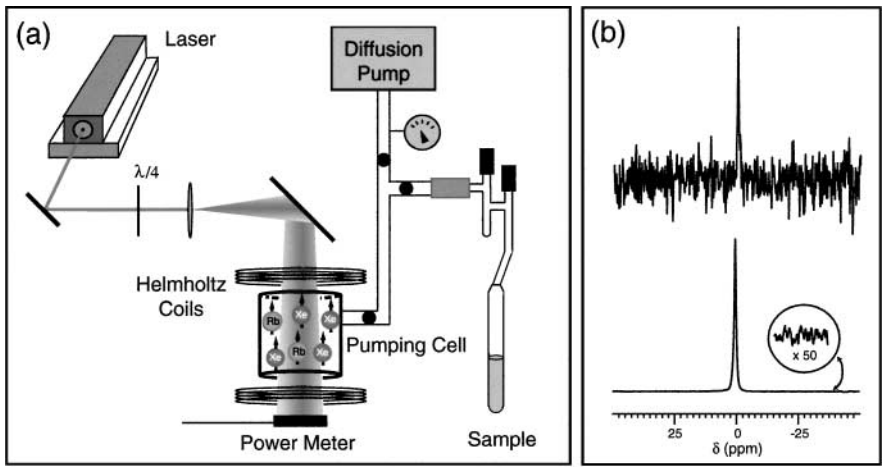

FIG. 4. (a) Schematic of the classic "batch" optical pumping apparatus (see, for example, Refs. (*35, 36*)). (b) OPNMR of laser-polarized xenon gas prepared with batch setup. ^{129}Xe NMR signal from xenon gas, obtained with (bottom) and without (top) laser-polarization. Bottom, one scan from a sample containing 2×10^{17} Xe atoms; top, one scan from a sample containing 5×10^{19} Xe atoms. The bottom spectrum reflects a ^{129}Xe NMR signal enhancement of ∼55,000 given a magnetic field of about 7 T, corresponding to a ^{129}Xe nuclear spin polarization of ∼35% (*37*). Figure courtesy of Holly Gaede and Alex Pines.

the figure is similar to that originally used at Berkeley for the first ^{129}Xe NMR studies of materials surfaces with laser-polarized xenon (*35*). The batch method is the simplest and is normally used for polarizing small amounts of the noble gas at low field (and at relatively low total pressure if very high polarization is required).

A narrow-bandwidth continuous-wave laser (usually a Ti: Sapphire or diode laser) produces a beam tuned to the D_1 resonance of Rb. The laser beam becomes circularly polarized by passing through a quarter-wave plate. Once expanded with optics, the beam is directed into a glass pumping cell residing in a weak (∼20–30 G) but homogeneous magnetic field produced by a Helmholtz coil pair; the pumping cell usually contains a few hundred torr of xenon (for example), a drop of Rb, and a small amount of nitrogen buffer gas. By uniformly heating the cell (usually to 60–100°C), a small amount of Rb will be vaporized so that it may be optically pumped by the laser. The Rb partial pressure, p_{Rb}, can be estimated using the relation (*32*):

$$\log\left(\frac{p_{\mathrm{Rb}}}{\mathrm{Pa}}\right) \approx 9.318 - \frac{4040}{\frac{T}{\mathrm{K}}} \qquad [12]$$

when performing optical pumping between the melting point of Rb (312.46 K) and about 550 K. Ideally, the "dark space" in the pumping cell (i.e., regions not illuminated by the pumping laser) should be minimized.

Throughout the optical pumping process, the gas line is evacuated (ideally to $\sim 10^{-5}$ torr or less) in order to minimize oxygen contamination of the laser-polarized xenon during transfer to the sample. Once the gas has been polarized, the pumping cell is rapidly cooled to condense the Rb. The laser-polarized xenon may be removed from the cell and transported to the NMR magnet via a direct transfer line and a pump, or as in the case shown in the figure, the xenon may be cryopumped into an NMR sample tube by immersing the sample's cold-finger in liquid nitrogen. Indeed, one key feature of laser-polarized xenon that permits its use in NMR experiments is that it can be accumulated and stored in the solid phase for hours, as first demonstrated by the Princeton group (*38, 39*). Once the laser-polarized xenon has been frozen into the cold-finger, the sample tube may be transported at leisure to the NMR magnet, where for experiments involving liquid samples (see Sections IV, V, and VIII) the xenon is rapidly sublimated and delivered to the solution prior to signal acquisition. The high xenon polarization can be maintained in the cold finger for long periods of time by exposing the frozen xenon to a strong magnetic field (≥500 G (*39*)), as discussed in the next section.

Alternatively, the noble gas may be optically pumped at high field within an NMR magnet if the laser beam can be directed into a pumping cell placed within the magnet's bore, as first shown by the Wuhan group (*40, 41*). Following optical pumping of Cs atoms with *linearly* polarized light within a 4.7-T NMR magnet (the strong field allows the Cs electronic sublevels to be spectrally resolved, permitting them to be selectively pumped—in this case, obviating the need for circularly polarized light), the Wuhan group was able to measure NMR signals from low-pressure (∼15 torr) laser-polarized xenon gas ($P \sim 1\%$) at high field. For a detailed description of high-field alkali metal spin exchange OPNMR experiments, the reader is directed to the more recent work performed at Yale (*42–44*).

Such "batch" optical pumping apparati as those shown in Fig. 4a are capable of producing xenon with nuclear polarization on the order of tens of percent, as shown by the ^{129}Xe NMR spectra in Fig. 4b. In fact, following careful optimization of the experimental conditions and the design of the apparatus, a batch

optical pumping setup has recently been developed in Marburg to produce small amounts of xenon with a nuclear spin polarization approaching 70% (*45, 46*). The authors of this work argue that such high polarization should produce detectable ^{129}Xe NMR signals from only $\sim 10^{13}$ xenon spins, thereby permitting (very low surface-area) single crystal surfaces to be probed with sub-monolayer (0.02) xenon occupancy.

3. *Alkali Metal Spin Exchange: The Continuous-Flow Apparatus*

A second type of apparatus first developed at Princeton for producing large quantities of polarized xenon is shown schematically in Fig. 5a, and will be referred to as the "continuous-flow" setup (*47*). In the Berkeley continuous-flow apparatus (*48, 49*), 5–10 atm of a gas mixture (comprised of ~1% Xe and ~1% N_2, with the remainder being helium-4) first flows through a heated chamber containing Rb (~1 g) precondensed on glass wool; the gas mixture becomes saturated with Rb, and then flows into the pumping cell. The Rb is optically pumped with a wide-bandwidth, high-power ($\geq$100 W) laser diode array (for a review of optical pumping with high-power diode arrays, see Ref. (*31*)). However, such high power is apparently unnecessary, as a reduction in laser power by half results in only a small reduction in spin polarization. Too much laser power can also cause overheating problems within the pumping cell, and one must guard carefully against explosions. The purpose of the helium buffer gas is to pressure-broaden the Rb absorption line, increasing the pumping efficiency of the wide-bandwidth (~2 nm) output of the laser. In the near future, more efficient high-power diode laser designs will likely be available with far narrower bandwidths, obviating the need for the high-pressure buffer gas, and reducing the degree of cell heating from excess incident laser radiation (see, for example, the recent work at Michigan (*50*)).

Once polarized in the cell, the xenon may be collected in a U-tube immersed in liquid N_2, while the buffer gas is released into the atmosphere. Alternatively, the U-tube may be removed and the gas flow may be directed into the NMR magnet for studying surfaces under continuous-flow conditions; in fact, the polarized gas flow may be recirculated for optical pumping *ad infinitum* by adding a recirculating pump after the NMR magnet and closing the loop by redirecting the exit flow into the pumping cell (*48, 49*). Figure 5b shows ^{129}Xe NMR spectra of laser-polarized xenon gas delivered to the NMR magnet under continuous-flow conditions. The steady-state nonequilibrium ^{129}Xe nuclear spin polarization attainable in this system recovers the initial conditions for each acquisition in only 4 s, as shown by the rapid change in the spectra when the optical pumping laser is turned off and then on again. By using such a continuous-flow apparatus, on the order of 1 L/hr of laser-polarized xenon can be obtained. A complete continuous-flow optical pumping apparatus is now commercially available from MITI. Different continuous-flow setups generate ^{129}Xe spin polarizations on the order of 2–20%.

Finally, an alternative optical pumping design has been developed at Michigan that is also capable of generating large quantities of laser-polarized noble gases (*51*). In this hybrid approach, large quantities of laser-polarized xenon are produced via systematic repetition of batch-mode optical pumping of xenon at

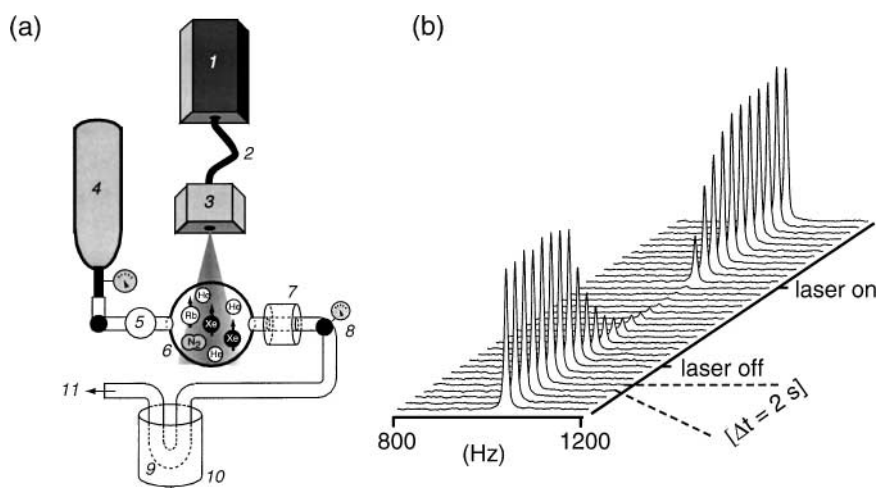

FIG. 5. (a) Continuous-flow apparatus, adapted from the original design in Ref. (*47*). The broad-band output from a high-power laser diode array (1, 130 W) is coupled through optical fibers (2) into a quarter-wave box (3) that expands the beam and renders it circularly polarized. A high-pressure gas cylinder (4) contains a pumping mixture composed of a few hundred torr of xenon, a few hundred torr of nitrogen, and 8–10 atm of helium buffer gas. The gas mixture flows from the cylinder through the rubidium storage region (5). Both this region and the pumping cell (6) are heated to ~160–180°C during pumping. The mixture then flows from the cell through the rubidium condenser (7); the flow rate is determined by a valve/flowmeter (8). Xenon is condensed over time in a U-tube (9) immersed in a dewar of liquid nitrogen (10), while the rest of the gas mixture is blown off into the atmosphere (11). The entire pumping process occurs within the fringe field of a superconducting NMR magnet or Helmholtz coil pair (not shown). Figure from Ref. (*12*). (b) Multiple ^{129}Xe NMR spectra obtained at 2-s intervals from a continuous stream of laser-polarized xenon gas flowing through the sample region within an NMR magnet. By turning the pumping laser off and on, the rapid recovery of the xenon polarization can be observed. In this experiment, the signal recovered with a time constant of ~4 s. Figure courtesy of Roberto Seydoux.

moderate pressure (1700 torr Xe, 150 torr N_2) using a high-power laser diode array. After each pumping cycle, the polarized gas mixture is pumped through a liquid-nitrogen-cooled trap that collects the polarized xenon (and maintains the xenon polarization at high field), permitting the nitrogen buffer gas to be separated and pumped away. This apparatus can routinely produce 157 cc atm of laser-polarized xenon gas ($P \sim 8\%$) every 5 minutes, or nearly 2 L atm/h.

III. PROPERTIES OF LASER-POLARIZED NOBLE GASES

A. General Properties of Xenon and Helium

The various phases of xenon conveniently exist in relatively accessible ranges, as shown in the phase diagram in Fig. 6. While gaseous at room temperature, xenon is rapidly frozen at liquid-nitrogen temperatures, facilitating accumulation and storage of laser-polarized xenon (*38, 39*). Liquid xenon may be obtained at moderate pressures (1–10 atm) via condensation at ~170–200 K, and the supercritical phase can be attained under conditions that appear mild when compared to most other substances (*52*). Xenon is a surprisingly effective solvent (see discussion in Section IV, and references therein). Helium, on the other hand, liquefies at about 4.2 K at 1 atm, and thus nearly all OPNMR applications of helium are performed in the gas phase.

Chemically speaking, helium is unreactive; with a few notable exceptions, xenon is also chemically inert. However, the highly polarizable electron cloud of xenon causes it to be relatively lipophilic, permitting xenon to participate in specific interactions with various substances (see Section V). Xenon readily adsorbs to numerous surfaces under experimentally convenient conditions (see Section VI). Xenon is also more soluble than helium by 10–100 times in different solvents and tissue environments (*57*).

Xenon is well known in the medical community for its anesthetic properties (*55, 56*) (which likely originate from its lipophilicity), suggesting that xenon NMR may be instrumental in elucidating the mechanism of general anesthesia (*57*). Both ^{129}Xe and ^{3}He are nontoxic and can therefore be used in high concentration in breathing mixtures for *in vivo* studies. However, xenon's anesthetic properties require that fractional xenon concentrations below 35% be used in breathing mixtures when it is necessary to avoid residual anesthetic effects (*58*).

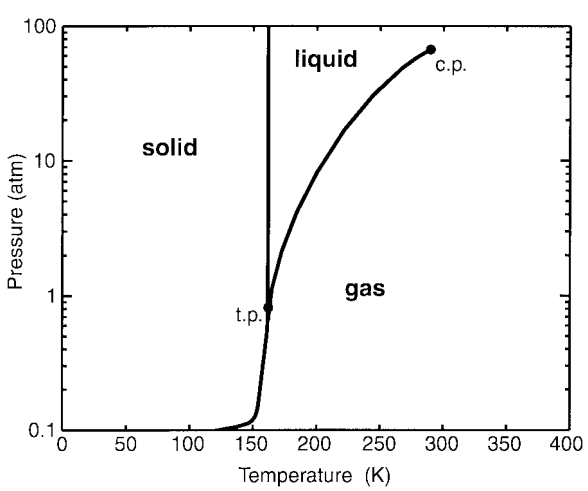

FIG. 6. Phase diagram of xenon. Triple point, 166.1 K, 0.8 atm; critical point, 289.7 K, 58 atm. Adapted from Ref. (*53*).

B. Diffusion of Xenon and Helium

Helium possesses a self-diffusion constant roughly 30 times that of xenon. For example, the self-diffusion constant for laser-polarized helium was recently measured to be about 0.21 cm^2/s at 7 atm and at room temperature by Fukushima and co-workers at LANL (*59*) (which, if scaled linearly, would translate to about 1.5 cm^2/s at 1 atm), compared with a value for xenon of 0.0565 cm^2/s at 1 atm (*60*). In experiments demonstrating the simultaneous measurement of D and T_2^*, Bock measured a slightly larger value of 1.8 cm^2/s for polarized ^{3}He at 1 bar and 20°C (*61*).

Incidentally, many recent measurements of the diffusive behavior of xenon and helium have been made using traditional NMR pulsed-field gradient echo techniques and laser-polarized gases (e.g., Refs. (*59, 61–66*)). Davies *et al.* first measured the diffusion constant of laser-polarized xenon within an optical pumping cell (*65*). Patyal *et al.* (*66*) measured the diffusion constant of laser-polarized xenon within two cells, obtaining 0.057 cm^2/s for a 790-torr sample and 0.044 cm^2/s for a 896-torr sample, in good agreement with the thermally polarized result mentioned above (*60*).

Workers at Harvard–Smithsonian (HSCfA), in different collaborations with scientists at MIT, Sclumberger-Doll, and Brigham and Women's Hospital, have performed a number of recent studies of diffusion using both laser-polarized and thermally polarized gases (*62–64*). Their work has been motivated by the sensitivity of time-dependent diffusive behavior of laser-polarized gases to the nature of motional restrictions (physical barriers to diffusion) within a given sample. The group has employed a novel NMR pulse sequence to permit the acquisition of a complete diffusive attenuation curve of a laser-polarized gas sample in a single measurement (*63*). Recently, the group was able to measure the pore surface-area-to-volume ratio and tortuosity in samples of random glass bead packs, limestone, and sandstone via gas diffusion NMR (GDNMR), thereby demonstrating the potential of using the diffusive behavior of laser-polarized gases to probe the structure and transport properties of various porous media. For discussions of the use of laser-polarized gases for studying convection and boundary-restricted diffusion via MRI, see Section VII.

C. NMR Properties and Experimental Considerations of Laser-Polarized Noble Gases

With the additional property of increased nuclear spin polarization from optical pumping, laser-polarized noble gases have

TABLE 1
Some Physical Parameters of Three Noble-Gas Isotopes

Isotope	Natural abundance (%)	Spin (I)	γ/γ_H
^{129}Xe	26.44	1/2	−0.2781
^{131}Xe	21.24	3/2	0.0824
^{3}He	1.3×10^{-4}	1/2	−0.7618

attracted considerable interest for greatly enhancing sensitivity when probing substances and living tissues via NMR and MRI (for additional reviews, see Refs. (*2, 12, 32, 37, 57, 67–71*). As summarized in Table 1, xenon possesses two NMR-active isotopes (^{129}Xe, $I = 1/2$ and ^{131}Xe, $I = 3/2$), both with sufficient natural abundance. ^{3}He ($I = 1/2$) is also commonly used in OPNMR experiments. While noble gas isotopes with $I > 1/2$ can be optically pumped, their quadrupolar moments give spin–lattice relaxation times in condensed phases that are too short to be practical for most NMR applications. With careful preparation of storage vessels, the high polarization of ^{129}Xe and ^{3}He can be maintained for long periods of time (hours to days). For example, the T_1 of ^{129}Xe was measured to be ∼3 hr at 77 K, and ≥100 h at 4.2 K (*38, 39*) when kept at high field (>500 G); without the external field, the ^{129}Xe will relax by coupling to the quadrupolar ^{131}Xe present in the lattice. When delivered to samples for NMR study, the T_1 of ^{129}Xe is typically over two orders of magnitude longer than that of ^{131}Xe. For these reasons, ^{129}Xe is the xenon isotope predominately used in OPNMR applications.

In principle, the T_1 of gaseous xenon in a homogeneous magnetic field would be limited only by spin-rotation relaxation during collisions, according to the relation (*72*)

$$T_1 \approx \frac{56}{\rho}, \qquad [13]$$

where ρ is the Xe density in amagat and the T_1 is in hours. However, the actual gas-phase ^{129}Xe T_1 is always considerably less, due to collisions between xenon and the walls of the sample.

Happer and co-workers (*73*) showed that T_1's of >20 min could be routinely obtained if the pumping cell is pretreated with the silicone coating agent SurfaSil (Pierce), a preparation which is still widely practiced. However, the exact manner by which this coating extends the lifetime of polarized xenon is still uncertain, despite considerable study. Later work at Princeton (*74*) investigating the field dependence of the gaseous ^{129}Xe T_1 in coated cells suggested that the xenon atoms become trapped in the permeable silicone coating for a surprisingly long time (>10 μs). Moreover, double-resonance experiments suggested that ^{129}Xe–^{1}H cross-relaxation was the dominant source of relaxation for ^{129}Xe in coated cells (*74*). Naturally, this result immediately suggested that the ^{129}Xe T_1 could be extended considerably (roughly by a factor of 15) simply by deuterating the coating, following the earlier example of Bouchiat (*75*). However, recent work using deuterated coatings (*76*) was able to extend the ^{129}Xe T_1 by only 15%; therefore, the authors of this work concluded that further study will be necessary to determine the true nature of the ^{129}Xe surface-induced relaxation in coated cells.

Neither helium nor xenon is naturally present in samples studied via OPNMR (e.g., living organisms), and thus there is no background signal to complicate experimental interpretation. In principle, ^{3}He would be the preferred isotope for MRI experiments because of its higher gyromagnetic ratio; however, its higher diffusion constant could in principle limit the gas-phase image resolution in some circumstances (although this problem has not manifested itself in lung imaging due to the boundary-mediated restrictions on diffusive behavior within the lungs—see the relevant discussions in Sections VII and VIII). These properties also require that the experimentalist take special care to minimize moving the helium through strong field gradients when transporting laser-polarized helium from the pumping chamber to the sample. The longitudinal relaxation rate resulting from diffusion in an inhomogeneous field is given by (*32*):

$$\rho_I^{\nabla B} \approx \frac{2}{3}\tau_c\langle v^2\rangle\left(\frac{\gamma_I G}{\omega_I}\right)^2, \qquad [14]$$

where $\langle v^2\rangle$ is the averaged square of the velocity of the gas atoms, τ_c is the mean time between collisions, and G is the field gradient transverse to the external magnetic field.

^{3}He also has the disadvantage of uncertain long-term availability. While ^{129}Xe is present as a trace gas in the atmosphere with relatively high natural isotopic abundance, ^{3}He is effectively a nonrenewable resource. Once ^{3}He is obtained (from tritium decay) and used, it eventually escapes the atmosphere and is lost.

1. Chemical Shift and Exchange of ^{129}Xe

Because of xenon's highly polarizable electron cloud, the chemical shift of xenon is exquisitely sensitive to its surroundings. Streever and Carr were the first to observe an apparently linear dependence of the xenon chemical shift on the density at moderate pressures (*77*). Subsequent work by Jameson and co-workers yielded an empirical equation for determining the xenon chemical shift (*78*),

$$\delta = [\mathrm{Xe}]\delta_1(\mathrm{Xe}-\mathrm{Xe}) + [\mathrm{Xe}]^2\delta_2(\mathrm{Xe}-\mathrm{Xe}) + \cdots, \qquad [15]$$

where the parameter δ_1(Xe − Xe) is a temperature-dependent quantity. For example, the ^{129}Xe resonance was determined to shift 0.539 ppm/amagat at 298 K (an amagat is the density of an ideal gas at STP, and corresponds to 2.69×10^{19} atoms/cm^3) (*78*). The parameter δ_2(Xe − Xe) was also determined to be temperature-dependent; however, at temperatures greater than about 298 K, δ_2(Xe − Xe) is effectively constant, with a value of ≈0.169×10^{-3} ppm/amagat (*78*).

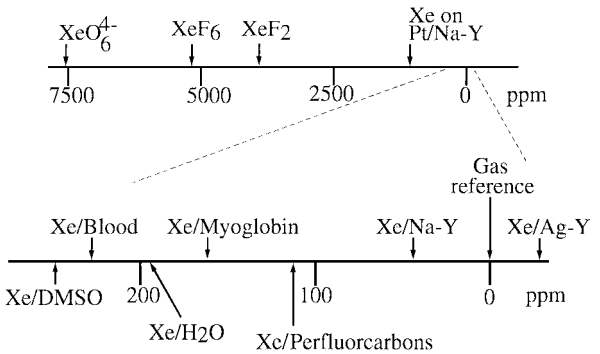

FIG. 7. Chemical shift values for xenon in various environments. Adapted from Ref. (*37*).

The chemical shift range of xenon in different chemical environments is over 7000 ppm wide, as shown in Fig. 7. While the large shift range results largely from strong electron deshielding in the xenon compounds, it is impressive to note that a range of over 200 ppm may be obtained merely by dissolving xenon in different liquids (*79*). Considerable work has therefore exploited such properties by using xenon as a nondestructive magnetic resonance probe of various chemical environments (for review, see Refs. (*68, 79–84*)). Numerous examples where optically pumped ^{129}Xe NMR is used to probe chemical and biological environments can be found throughout this review.

Except in cases involving xenon compounds (e.g., XeF_6 and XeO_4), NMR studies of xenon will usually occur in the presence of exchange phenomena. Thus, multisite exchange models are often used to interpret ^{129}Xe spectra. Naturally, the simplest nontrivial version, the two-site exchange model, can be adopted for discussions regarding xenon exchange between two different environments (e.g., red blood cells and plasma, discussed in detail in Section VIII).

We say that the exchange between two sites is "slow" on the NMR time scale when two lines can be resolved in the NMR spectra originating from the exchanging species. In general, for chemical exchange between two equally populated sites, the limiting condition of slow exchange can be written as

$$[2\pi(\Delta\nu)\tau_{res}]^2 \gg 1, \qquad [16]$$

where $\Delta\nu$ is the difference in frequency between the resonances of the species at each site, and τ_{res} is the average residence time; $\tau_{res} = (k)^{-1}$, where k is the exchange rate. A derivation of the equivalent form of Eq. [16] for the case of asymmetric exchange is beyond the scope of this review; a discussion of this topic, and dynamic NMR spectroscopy in general, can be found in Ref. (*85*). The trends predicted by Eq. [16] can still be helpful, however, even under conditions of asymmetric exchange. In conditions of fast xenon exchange (such as that observed in solutions of xenon and hemoglobin, where $\tau_{res} \sim 3\ \mu$s (*86*)), only one peak is observed, whose chemical shift is a population-weighted average of the two (or more) different environments. Thus, under conditions of slow exchange, it is easier to extract information regarding the different xenon environments. Luckily, the wide chemical shift range of xenon lowers the limit of slow exchange (as suggested by Eq. [16]); naturally, this condition can also be somewhat extended by using stronger external magnetic fields.

2. *Conserving Polarization During RF Pulsing*

The nonrenewable nature of the polarization of laser-polarized gases complicates their use for many NMR/MRI applications. Accordingly, the modification of conventional RF pulse sequences to meet the unique requirements of polarized gases has already been the subject of considerable work (see, for example, Refs. (*66, 87–91*)).

The most obvious requirement is that the RF pulse sequence chosen for a particular OPNMR application must be applied much faster than (or at worst, on the timescale of) the characteristic T_1 of the gas within the sample. Naturally, this point is particularly critical for complicated imaging experiments involving living organisms. For a detailed discussion of considerations for choosing an imaging sequence for different polarized gas applications, see the review of Zhao and Albert (*87*).

Second, for most experiments acquisition pulses applied directly to resonances of laser-polarized gases must be of small tipping angle in order to avoid using up all of the polarization at once. The only way to replenish the signal for averaging (or repetition) is to deliver fresh polarized gas to the sample (e.g., by continuous flow (*48, 49*)); however, in some circumstances the long T_2 values of polarized gases may permit the use of echo-summation techniques to maximize the SNR that can be obtained (*87*).

The application of each RF observation pulse of tipping angle α reduces the remaining z-component of the magnetization by a factor of $\cos(\alpha)$. For example, a common method for measuring the T_1 of a polarized gas within a particular environment employs a series of small pulse/acquisition pairs spaced out over the duration of the relaxation behavior. If the RF pulses are small (a few degrees) and are well-calibrated, the T_1 may be trivially extracted from the observed signal decay. One common imaging method known as FLASH (Fast Low-Angle SHot) imaging (*92*) is a natural choice for polarized gases, as it uses small tipping-angle RF pulses along with stepped pulsed-field gradients to map out k-space. However, the decrease in z magnetization of polarized gases with pulsing can cause artifacts in images and spectra. This effect may be combated by employing a "variable-flip-angle" approach where the tipping angle of N RF pulses is steadily increased, such that the tipping angle of the nth pulse is given by (*88*)

$$\alpha = \tan^{-1}\left(\frac{1}{\sqrt{N-n}}\right). \qquad [17]$$

Increasing the tipping angle in this manner will maintain the signal amplitude as the magnetization is consumed, up until the final (90°) pulse.

If the desired experiment requires the application of 180° pulses (see, for example, the difference SPINOE experiments described in Sections IV and V), then special care must be taken to ensure maximally efficient inversion of the polarized gas magnetization. Inefficient inversion will leave magnetization behind in the $x - y$ plane, accelerating the depletion of the finite z magnetization of the polarized gas. Additionally, radiation damping (*3*) (the back-reaction of the detection coil on the sample magnetization caused by its precession within the coil) can pose an additional complication because of the high magnetization of polarized gases. Indeed, the effects of radiation damping have recently been observed both in high-field, high-resolution ^{129}Xe OPNMR spectroscopic experiments (*90*), and low-field ^{3}He OPMR imaging experiments (*93*). Radiation damping does not reduce the size of the magnetization but changes its direction, tending to align magnetization placed in the $x - y$ plane back along the external field. Adiabatic 180° pulses (followed by strong "spoiler" gradient pulses) (*90, 91, 94, 95*) may be employed to ensure maximal inversion, thereby preventing unwanted magnetization from accumulating in the $x - y$ plane (see Section IV).

However, the nonrenewable nature of the polarization can also be *advantageous* in biomedical applications for two reasons: (1) the polarization can be permanently destroyed at will with high efficiency and locality using standard MRI techniques, and (2) dilution and short *in vivo* relaxation times should cause the contribution to the signal from recirculation to be negligible. These characteristics should greatly simplify interpretation when using polarized gases as tracers to measure local blood flow.

IV. "LIGHTING UP" THE NMR OF MOLECULES. I. NONSPECIFIC INTERACTIONS

A. Introduction

The increased nuclear polarization from optical pumping has attracted considerable interest for using laser-polarized ^{129}Xe to enhance sensitivity when probing substances via ^{129}Xe NMR. However, the information obtained in this manner is still indirect, requiring that underlying structure and dynamics be inferred from the observed chemical shift, chemical-shift anisotropy (CSA), or relaxation parameters of xenon in intimate contact with the substance being studied. Thus, in many circumstances a more direct method of probing such substances would be desired. Moreover, any means by which the overall NMR signal from molecules and materials themselves can be increased would be generally welcomed. For these reasons, considerable work has investigated the possibility of transferring polarization from laser-polarized xenon (and helium) to other nuclei, thereby "lighting up" the NMR of species interacting with laser-polarized noble gases.

B. Polarization Transfer via Low-Field Thermal Mixing

Soon following predictions that polarization could be transferred from laser-polarized xenon to enhance the NMR signals of other substances (*35*), polarization transfer was first experimentally demonstrated when ^{131}Xe NMR signals from xenon ice were enhanced by low-field thermal mixing with laser-polarized ^{129}Xe (*38*).

Low-field mixing involves adiabatically sweeping the external magnetic field through a regime where the difference between the Zeeman energies of the two spin baths (in this case, ^{129}Xe ^{131}Xe spins in xenon ice) is matched by their dipolar coupling. Following thermal mixing, the two spin baths (generally speaking, I and $S = {}^{129}$Xe) share a common inverse temperature, β, given by

$$\beta \approx \frac{\alpha}{1 + \frac{\gamma_S^2 N_S}{\gamma_I^2 N_I}}, \qquad [18]$$

where α is the inverse spin temperature of ^{129}Xe given by optical pumping (the form of Eq. [18] assumes that $I = S = 1/2$).

Low-field thermal mixing was later used to enhance the spin polarization of other substances in contact with laser-polarized xenon (*96, 97*). In one study by Bowers *et al.* at Berkeley the ^{13}C NMR signals from CO_2 molecules embedded in a laser-polarized xenon ice matrix were enhanced by a factor of ~200 (at 4.2 T), as shown in Fig. 8 (*96*). Figure 8a shows the enhanced ^{13}C CSA of CO_2 following zero-field mixing with laser-polarized xenon; Fig. 8b shows a spectrum taken from a sample prepared identically as that observed in (a), except that the xenon was prepared with the opposite polarization. The change in phase of the ^{13}C NMR signal demonstrates that the observed effect originates from polarization transfer from the laser-polarized xenon in the matrix.

Polarization has also been transferred successfully from laser-polarized xenon to material surfaces by RF-driven Hartmann–Hahn cross-polarization (*98–100*) through dipolar couplings at high field (*101, 102*) (discussed later in Section VI). Both low-field mixing and high-field cross-polarization require either (a) that the nuclei to be polarized have been embedded in a laser-polarized xenon ice matrix (*38, 96*) or (b) that laser-polarized xenon has been immobilized onto the material's surface (*97, 101, 102*). Both of these preparations can be difficult to achieve in practice. Moreover, these methods cannot be employed for intermolecular polarization transfer in isotropic liquids, because dipolar couplings are averaged away by the rapid tumbling and translational diffusion of molecules in solution. Therefore, a different physical process must be exploited in order to obtain polarization transfer and subsequent signal enhancement in solution.

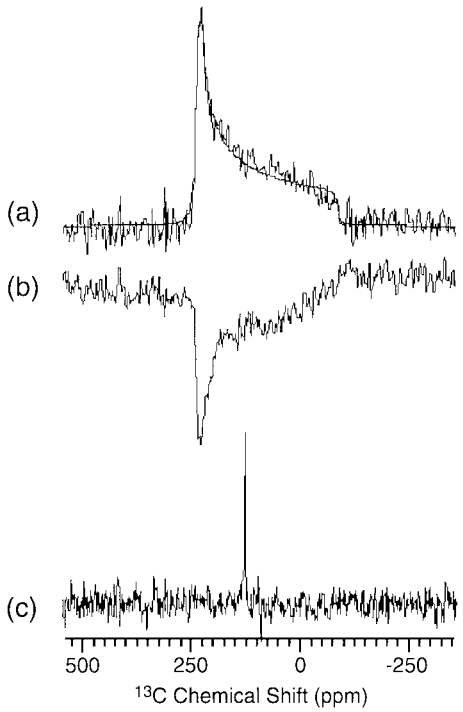

FIG. 8. Enhancement of NMR signals of $^{13}CO_2$ obtained from low-field thermal mixing. (a) ^{13}C NMR signal obtained with one scan following low-field thermal mixing of a matrix comprised of spin-labeled CO_2 embedded in laser-polarized xenon ice. The curve superimposed upon the experimental data represents a theoretical fit to the ^{13}C CSA. (b) As in (a), but with oppositely polarized xenon. (c) Control spectrum obtained by taking 64 scans of $^{13}CO_2$ gas. Figure adapted from Ref. (*96*).

C. The Spin Polarization-Induced Nuclear Overhauser Effect

1. First SPINOE Experiments

It was recently demonstrated that when laser-polarized xenon is dissolved in benzene, an enhancement of the benzene ^1H NMR signal may be observed (*103*), shown in Fig. 9. This transient enhancement of the ^1H signal is a consequence of cross-relaxation and polarization transfer between the dissolved laser-polarized xenon and the surrounding solution spins, a novel manifestation of the nuclear Overhauser effect (NOE) (*104, 105*). The ^1H NMR signal of pure benzene was observed to be enhanced by about 10% (at 4.3 T) following dissolution of laser-polarized xenon, while the ^1H NMR signal of partially deuterated benzene (25% C_6D_5H, 75% C_6D_6) was enhanced by a factor of $\sim$2. As shown in Fig. 9, reversing the polarization of the laser-polarized xenon brought about a concomitant change in the sign of the observed signal enhancement, again indicating that the effect resulted from the enhanced polarization of the laser-polarized xenon. Finally, it was demonstrated that the enhanced proton polarization could be imaged (shown later in Section VII), suggesting the possibility of using cross-relaxation with dissolved laser-polarized xenon to perform novel *in vivo* ^1H MRI experiments.

2. Theoretical Background

The above phenomenon has been dubbed the spin polarization-induced nuclear Overhauser effect (SPINOE) (*103*). In order to better understand the SPINOE, the underlying principles of nuclear dipolar cross-relaxation are reviewed, and slightly recast in light of the unique properties of laser-polarized noble gases.

Consider two ensembles composed of spins I and S (where, for the time being, we will assume that $I = {}^1H$ and $S = {}^{129}Xe$) participating in mutual dipolar cross-relaxation (Figs. 10a, 10b). The time-dependent behavior of the coupled spin baths can be described by the Solomon equations (*106–108*):

$$\frac{d\langle I_z\rangle}{dt} = -\rho_I(\langle I_z\rangle - I_0) - \sigma_{IS}(\langle S_z\rangle - S_0), \qquad [19]$$

$$\frac{d\langle S_z\rangle}{dt} = -\rho_S(\langle S_z\rangle - S_0) - \sigma_{SI}(\langle I_z\rangle - I_0). \qquad [20]$$

ρ_I (ρ_S) is the auto-relaxation rate for spin I (S), σ_{IS} (σ_{SI}) is the I $\leftarrow$ S (S $\leftarrow$ I) cross-relaxation rate, $\langle I_z\rangle$ and $\langle S_z\rangle$ are respectively the ensemble-average values of the z component of the **I** and **S** nuclear spin operators, and I_0 and S_0 are their equilibrium values; for example,

$$I_0 = \frac{I(I+1)\hbar\gamma_I B_0}{3kT}. \qquad [21]$$

For spin-$I = 1/2$ nuclei, $I_0 = P/2$.

A full solution of Eqs. [19], [20] can be found in the literature (*109*), as can a detailed review of the SPINOE (*110*). The SPINOE enhancement for an ensemble of proton spins participating in dipolar cross-relaxation with laser-polarized ^{129}Xe is

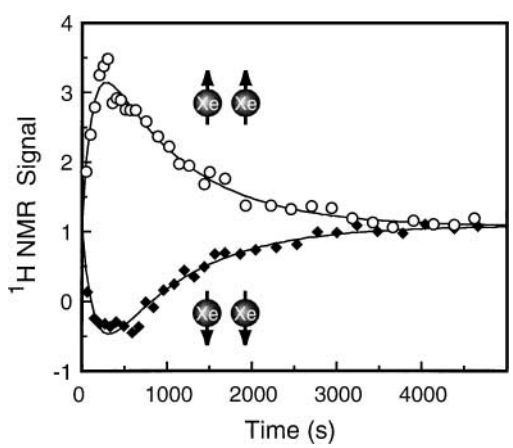

FIG. 9. Time dependence of the integrated ^1H NMR signal from a partially deuterated benzene solution containing dissolved laser-polarized xenon (*103*). The SPINOE produced positive benzene ^1H NMR signal enhancements when "positively" polarized xenon was dissolved (open circles), and negative signal enhancements when "negatively" polarized xenon was dissolved (filled diamonds). Adapted from figure courtesy of Yi-Qiao Song.

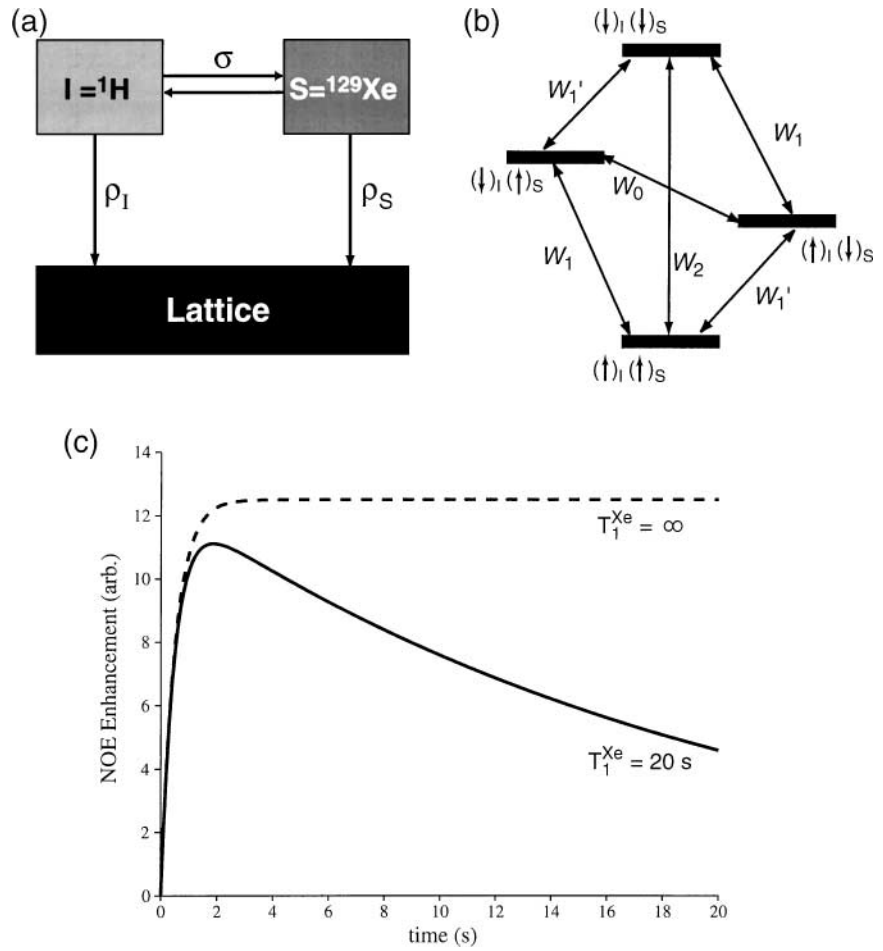

FIG. 10. Macroscopic (a) and microscopic (b) diagrams of the SPINOE. (a) Polarization enhancement of the proton spin bath (I) is achieved via cross-relaxation with laser-polarized xenon (S), governed by the cross-relaxation rate, $\sigma(\sigma_{IS} = \sigma_{SI} \cdot (N_S/N_I))$. The polarization enhancement for the protons is limited by the respective autorelaxation rates of both spin baths, ρ_I and ρ_S. (b) General two-spin model for the NOE, assuming positive gyromagnetic ratio for both spins. The transfer of population among the four levels is governed by W_1 and W_1' (the single-quantum transition probabilities), which contribute to the autorelaxation of the spins, and W_0 and W_2 (respectively the zero-quantum and double-quantum transition probabilities), which contribute to both the cross-relaxation and autorelaxation rates. (c) Calculated time dependence of the SPINOE signal, including (solid line) and not including (dotted line) the exponential decay caused by the eventual ^{129}Xe spin–lattice relaxation. Curves were calculated with $\rho_H = 2\,s^{-1}$, $\sigma_{HXe} = 0.001\,s^{-1}$, and $\rho_{Xe} = 0.05\,s^{-1}$ (for the solid curve). Behavior such as that shown with the dotted line may also be seen under conditions of continuous flow of laser-polarized xenon (see Refs. (*48, 49*) and the discussion in Section VI).

well approximated by

$$f_H(t) = -\frac{\gamma_{Xe}}{\gamma_H} f_{Xe}(0) \frac{\sigma_{HXe}}{\rho_H}(1 - e^{-\rho_H \cdot t}), \qquad [22]$$

where $f_H(t) = [\langle I_z(t)\rangle - I_0]/I_0$ is the fractional polarization enhancement of the protons, and $f_{Xe}(0)$ is the fractional polarization enhancement for the xenon endowed by optical pumping. Figure 10c shows the time dependence of the SPINOE enhancement as calculated by Eq. [22]. Equation [22] assumes that the spin–lattice relaxation time of ^{129}Xe, T_1^{Xe}, is much greater than that measured for the protons, T_1^H (generally true for ^{129}Xe in solution), or that the xenon spin polarization is maintained by continuous flow (*48, 49*).

Equation [22] governs the initial rise in signal shown in the curves in Fig. 10c (as well as that manifested in the experimental data shown in Fig. 9); the latter exponential decay towards equilibrium is governed by T_1^{Xe}. Given the value of T_1^H, the initial ^{1}H NMR enhancement observed over a given time can be used to compute σ_{HXe}. As will be discussed in the next section, σ_{HXe} not only governs the polarization transfer, but can yield important structural and dynamical characteristics of the molecule–xenon interaction.

Recall that in the two-spin model, the nuclear spin cross-relaxation and auto-relaxation rates are generally given by (for example) (*107*)

$$\sigma_{IS} = W_2 - W_0, \qquad [23]$$

$$\rho_I = W_2 + 2W_1 + W_0, \quad [24]$$

where each transition probability between two given states ($|\psi_i\rangle$, $|\psi_j\rangle$), W_{ij} can be derived from the familiar Fermi Golden Rule (after Solomon (*106*)),

$$W_{ij} = \frac{1}{t\hbar^2}\left| \int_0^t dt' \langle\psi_i|H_D(t')|\psi_j\rangle e^{-it'}\left(\frac{E_j - E_i}{\hbar}\right)\right|^2, \quad [25]$$

where each state is a member of the four-level diagram shown in Fig. 10b, and $H_D(t)$ is the (time-dependent) heteronuclear dipolar Hamiltonian, which may be written as

$$H_D^{IS} = \frac{\mu_0\gamma_I\gamma_S\hbar^2}{4\pi r_{IS}^3}(1 - 3\cos^2\theta_{IS})I_{Iz}I_{Sz}; \quad [26]$$

the implicit time dependence originates from the random reorientations and relative diffusive motion of the species involved.

It can be shown (*107*) that the SPINOE cross-relaxation rate between laser-polarized xenon and protons can be explicitly written as

$$\sigma_{\mathrm{HXe}} = \left(\frac{\mu_0}{4\pi}\right)^2 \frac{\hbar^2\gamma_{\mathrm{H}}^2\gamma_{\mathrm{Xe}}^2}{10}\left\langle\frac{1}{r_{\mathrm{HXe}}^6}\right\rangle [6J(\omega_{\mathrm{H}} + \omega_{\mathrm{Xe}}) - J(\omega_{\mathrm{H}} - \omega_{\mathrm{Xe}})], \quad [27]$$

where r_{HXe} is the proton–xenon internuclear distance, $\langle\ \rangle$ denotes the ensemble average, and the spectral density $J(\omega)$ is given by

$$J(\omega) = \frac{\tau_c}{1 + \omega^2\tau_c^2}, \quad [28]$$

where τ_c is the correlation time associated with the fluctuations of the H–Xe dipolar interactions. Thus, both $\langle r_{\mathrm{HXe}}^{-6}\rangle$ and τ_c control the size and selectivity of the observed H–Xe cross-relaxation rates.

From Eqs. [27], [28] it can be shown that σ_{HXe} is always positive (regardless of the correlation time or the external field strength), resulting from the large difference between the gyromagnetic ratios of ^{1}H and ^{129}Xe. Therefore, it is expected that when "positively" polarized xenon is dissolved into solution, positive SPINOEs will be observed (to avoid confusion with the previous literature originating from the negative sign of γ_{Xe}, here we define "positively" polarized xenon to be xenon laser-polarized in the same direction as its equilibrium polarization (with the population of $m_I = -1/2$ greater than the population of $m_I = +1/2$), therefore giving a positive value for $f_{\mathrm{Xe}}(0)$). This behavior is, in fact, observed in Fig. 9; conversely, the admission of "negatively" polarized xenon (produced by inverting the magnetic field in which the xenon was laser-polarized) brought about a corresponding negative SPINOE in the benzene ^{1}H NMR signal.

3. Diffusion-Modulated Dipolar Cross-Relaxation

The dipolar relaxation between xenon and benzene is modulated by the relative diffusive motion between these two species. From the data shown in Fig. 9, it was determined that the cross-relaxation rate was $\sim 1.9 \times 10^{-6}$ s^{-1}, in general agreement with theoretical estimates of diffusion-modulated cross-relaxation between protons and ^{129}Xe in solution (*103*), as discussed below.

Molecular dynamics simulations can be extremely helpful for understanding intermolecular relaxation (for examples regarding xenon spin relaxation in solution, see Refs. (*111, 112*)); however, such simulations tend to be computationally expensive. Instead, simpler models of intermolecular relaxation exist that despite their reliance upon simple assumptions (*107*) can give reasonable qualitative descriptions of intermolecular dipole–dipole relaxation processes. For example, it can be shown that when the cross-relaxation is modulated by relative diffusive motion, σ_{IS} should be linearly dependent upon the concentration of molecules bearing spin S; thus in our case, σ_{HXe} is dependent on [Xe]. In fact, such a dependence arises from the ensemble average of r_{HXe}^{-6}. In a pairwise additivity scheme for xenon-solute interactions, $\langle r_{\mathrm{HXe}}^{-6}\rangle$ is given by the relation

$$\langle r_{\mathrm{HXe}}^{-6}\rangle = \left[4\pi N_A 10^{-27}\int_0^\infty dR \cdot R^2 \frac{\int d\Omega \cdot g(R,\Omega)\cdot r_{\mathrm{HXe}}^{-6}}{\int d\Omega}\right]\cdot[\mathrm{Xe}], \quad [29]$$

where R is the distance between the center of mass of the solute molecule and the xenon atom (with both R and r_{HXe} in Å), N_A is Avogadro's number, Ω represents the angular variables specifying the relative orientation of the solute-xenon pair, and $g(R, \Omega)$ is the solute–xenon pair distribution function. Incidentally, because (to a good approximation) $\langle r_{\mathrm{HXe}}^{-6}\rangle$ is proportional to [Xe], a concentration-normalized H-Xe cross-relaxation rate, σ_{HXe}^n (s^{-1} M^{-1}), may be defined such that

$$\sigma_{\mathrm{HXe}}^d = \sigma_{\mathrm{HXe}}^n[\mathrm{Xe}], \quad [30]$$

where σ_{HXe}^d explicitly refers to cross-relaxation originating from purely diffusive coupling.

Concerning the dynamics of the diffusive coupling, it is clear that an upper bound for the correlation time is provided by the residence time of xenon in the solvation shell of the solute (usually a few picoseconds). Thus, the condition of extreme narrowing ($(\omega\tau_c)^2 \ll 1$)) is thereby fulfilled in normal circumstances. The proton–xenon cross-relaxation rate resulting from diffusive coupling is then given by

$$\sigma_{\mathrm{HXe}}^d = \left(\frac{\mu_0}{4\pi}\right)^2 \frac{\hbar^2\gamma_{\mathrm{H}}^2\gamma_{\mathrm{Xe}}^2}{10}\langle r_{\mathrm{HXe}}^{-6}\rangle 5\tau_c^d, \quad [31]$$

where τ_c^d explicitly refers to the correlation time governing the diffusive coupling between xenon and the other spin.

One should remember that τ_c^d may be unrelated to the correlation time controlling the proton dipole–dipole intramolecular relaxation of the solute molecule participating in cross-relaxation with xenon. For instance, in circumstances where the molecular mass of the solute significantly exceeds the xenon atomic mass, the tumbling motion of the solute molecule is expected to be slow on the timescale of the residence of xenon atoms in the solvation shell of the solute. Consequently, the magnitude of the SPINOE signal resulting from diffusive coupling should generally decrease for increasing solute size (not because σ_{HXe}^d is affected, but because the proton auto-relaxation time is reduced (*36*)).

The order of magnitude of σ_{HXe}^n and σ_{HXe}^d can now be estimated by assuming the system is a monatomic fluid and by using a Heaviside step function as an approximation for the radial pair distribution function ($g(r) = 0$ for $r < r_0$ and 1 otherwise) in Eq. [31], giving

$$\left\langle r_{\mathrm{HXe}}^{-6} \right\rangle \approx \frac{4}{3}\pi N_A 10^{-27} r_0^{-3} [\mathrm{Xe}], \qquad [32]$$

where r_0 is the proton–xenon minimum approach distance. Thus, given $\tau_c^d = 5$ ps and $r_0 \sim 3.0$–3.2 Å, σ_{HXe}^n is estimated to be on the order of 10^{-5} s^{-1} M^{-1} from Eq. [31]. Finally, because the solubility of xenon in organic solvents under standard conditions is on the order of 0.1 M, σ_{HXe}^d is expected to be on the order of 10^{-6} s^{-1}. Indeed, this prediction is in excellent agreement with the value of $\sim 1.9 \times 10^{-6}$ s^{-1} observed between benzene protons and dissolved laser-polarized xenon (*103*).

In the framework of the dipolar-coupled two-spin model, the auto-relaxation of the protons would be solely a consequence of dipole–dipole interactions with laser-polarized ^{129}Xe. However, molecules in solution contain many-spin systems, so intermolecular ^{1}H–^{129}Xe dipole–dipole interactions are not likely to contribute significantly to the ^{1}H auto-relaxation rate. For solutes at low concentration in deuterated solvents, when no paramagnetic species are present, intramolecular ^{1}H–^{1}H dipole–dipole interactions normally dominate the auto-relaxation of protons (especially in molecules large enough to bind xenon), although other mechanisms, such as spin-rotation coupling, may contribute to the relaxation of small molecules such as benzene or parts of molecules, like methyl groups. Therefore, the simplest realistic model for $^{129}\mathrm{Xe} \rightarrow {}^1\mathrm{H}$ polarization transfer requires at least a three-spin system comprised of two interacting protons and one xenon atom participating in dipolar interactions with only one of the proton sites. Such a three-spin model can be found in Ref. (*36*). However, for the purpose of interpreting experimental SPINOE spectra, the two-spin model is usually sufficient, provided that the *experimental* spin–lattice proton relaxation times are considered.

4. Pulse Sequence Considerations

In the Xe/benzene experiments discussed above, the SPINOE enhancements were between 10% and 200%, large enough to observe by acquiring the ^{1}H signal as a function of time, and carefully subtracting the equilibrium ^{1}H signal from each spectrum following acquisition. In many cases, the NMR signal enhancement obtained via the SPINOE will be small compared to the equilibrium NMR signal for a given species, necessitating an NMR pulse sequence designed to directly obtain the SPINOE contribution to a given signal. A heteronuclear NOE sequence adapted from the sequences of Shaka and co-workers (*113, 114*) is shown in Fig. 11a; an NMR signal obtained with this sequence will be referred to as a SPINOE spectrum. The sequence

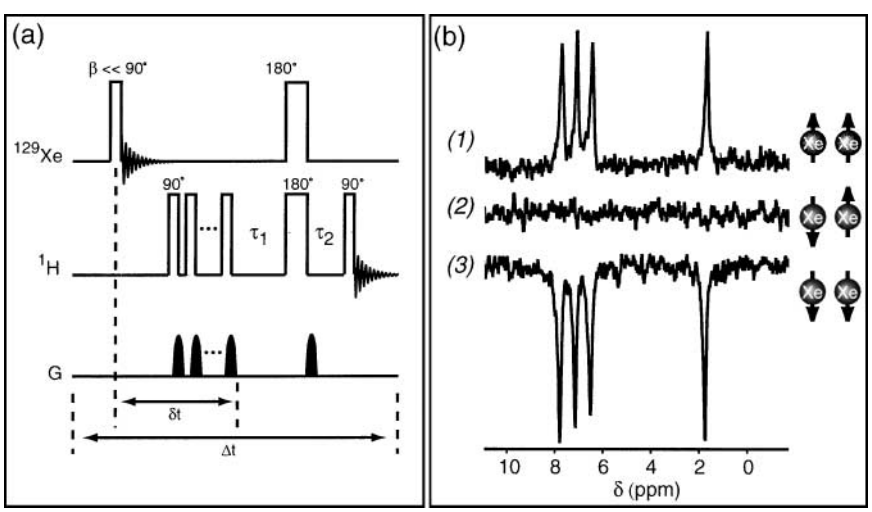

FIG. 11. (a) Heteronuclear difference NOE pulse sequence for obtaining SPINOE spectra (*36, 91*), adapted from sequences developed by Shaka and co-workers (*113, 114*). (b) ^{1}H SPINOE spectra from a solution of 0.1-M *p*-nitrotoluene and d_5/d_6-benzene containing dissolved laser-polarized xenon (*91*). (1) Spectrum acquired following the introduction of "positively" polarized xenon. (2) As in (1), but without the application of the ^{129}Xe 180° pulse, demonstrating complete suppression of the equilibrium proton signal. (3) As in (1), but with "negatively" polarized xenon, yielding a corresponding sign change in the ^{1}H SPINOE spectrum.

in Fig. 11a effectively suppresses the equilibrium NMR signal, conveniently allowing direct detection of NOE signals as weak as $\sim 10^{-4}$ of the equilibrium signal.

The first element of the sequence, a small tipping-angle observation pulse on the ^{129}Xe resonance, is applied prior to the acquisition of ^{1}H SPINOE spectra and is necessary only for calibrating the xenon polarization to calculate absolute values for the Xe–H cross-relaxation rates. Saturation of the equilibrium ^{1}H signal is first achieved by the application of the 90° and gradient pulses; the saturation is then maintained by a 180° pulse followed by a gradient pulse. The ^{129}Xe pulse permits the SPINOE signal to accumulate during τ_1 and τ_2. The values of τ_1 and τ_2 are normally chosen such that: (1) their sum is much less than T_1^{Xe}; (2) their sum is on the order of or less than T_1^{H}; and (3) their ratio minimizes the equilibrium proton signal detected in the absence of SPINOE polarization transfer. The ^{1}H and ^{129}Xe 180° pulses are often adiabatic, modulated pulses (see, for example, Refs. (*90, 94, 95*)) to ensure efficient, wide-band inversion. Generally, each SPINOE spectrum is the difference of two acquisitions.

The difference SPINOE pulse sequence in Fig. 11a was first applied to directly observe the cross-relaxation between dissolved laser-polarized xenon and *p*-nitrotoluene in a perdeuterated benzene solution (*91*); the corresponding SPINOE spectra are shown in Fig. 11b. Specifically, Figs. 11b(1, 3) show the NMR signal originating exclusively from cross-relaxation with laser-polarized xenon, while Fig. 11b(2) contains the NMR signal observed with the same pulse sequence, except without the application of the ^{129}Xe 180° pulse (thereby preventing SPINOE accumulation). The lack of signal in Fig. 11b(2) demonstrates the effectiveness of the pulse sequence in Fig. 11a for suppressing the equilibrium signal.

D. Using Xenon as a Polarizing Solvent

In the absence of strong xenon binding, the observed Xe–H cross-relaxation rate is proportional to the concentration of xenon in the solution; therefore, higher concentrations of laser-polarized xenon should yield larger SPINOE enhancements for other solute species. To maximize this effect, recent work has investigated the use of laser-polarized xenon as the *solvent* in SPINOE experiments. Increasing the nuclear spin polarization of molecules in solution could be useful for a variety of liquid-state NMR and MRI experiments, including circumstances where the observed nucleus is in low natural abundance or the species in question are short-lived. Moreover, because xenon is transparent to electromagnetic radiation from the far-IR to the vacuum-UV, it is an attractive solvent for *in situ* spectroscopy (e.g., for studying the photochemistry of organometallic substances (*52*)).

1. Liquid Laser-Polarized Xenon

Liquid xenon is a surprisingly effective solvent for small organic molecules; it can even be used to dissolve certain inorganic complexes and biomolecules to varying degrees (*115–118*). The solubility characteristics of both liquid and supercritical xenon can be improved by the addition of small amounts of other compounds (*119, 120*).

Liquid laser-polarized xenon has been successfully produced and studied via NMR (*121–123*). For example, by carefully preventing contamination from paramagnetic oxygen, the Princeton group determined that the T_1 of liquid laser-polarized xenon was about 25 min. (*121*), long enough to permit significant polarization transfer to solute species. And unlike the solid phase, it was shown that the high, nonequilibrium polarization of liquid laser-polarized xenon could be maintained for long times at low field; the dipolar coupling between laser-polarized ^{129}Xe and quadrupolar ^{131}Xe that dominate ^{129}Xe T_1 in the solid phase is quenched by the random diffusive motion in solution.

Liquid laser-polarized xenon has since been used to significantly enhance the NMR signals of dissolved molecules (*124*). Under conditions below 200 K, such experiments could be performed at relatively low pressures without prohibitively sacrificing the solubility of the small organic molecules being studied. For example, when toluene was dissolved in liquid laser-polarized xenon, ^{1}H NMR signals from the aromatic and methyl protons were respectively enhanced by factors of 16 and 6 at 1.4 T, as shown in Fig. 12. It is also interesting to note that the observed differential enhancement cannot be entirely attributed to the large difference between the T_1^{H} values measured for these protons (aromatic protons: $T_1^{H} = 21$ s; methyl protons: $T_1^{H} = 6.1$ s), suggesting either a physical difference between the respective xenon-proton interactions (e.g., a difference in average xenon proximity or dynamics for the two types of protons),

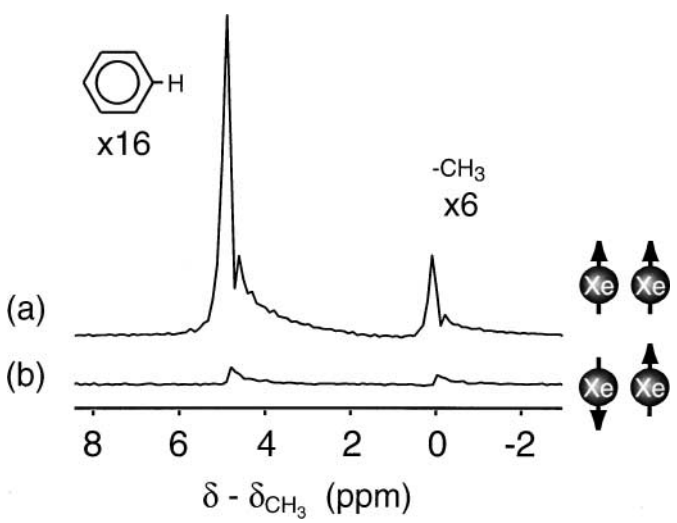

FIG. 12. ^{1}H NMR signal from toluene dissolved in liquid xenon at 200 K and 1.4 T, with (a) and without (b) laser-polarization (*124*). By dissolving toluene in liquid laser-polarized xenon, the NMR signal from the methyl protons was enhanced by a factor of 6, while the signal from the aromatic protons was enhanced by a factor of 16. These enhancements were obtained with natural isotopic abundance of ^{129}Xe, and with ^{129}Xe nuclear polarization of about 7%. Figure adapted from data courtesy of Karen Sauer.

or more simply, significant ^{1}H–^{1}H polarization transfer via "relayed" SPINOE (see Ref. (*36*)). A factor of 45 enhancement was achieved for the ^{1}H NMR signal of dissolved cyclopropane by using 71% ^{129}Xe-enriched laser-polarized liquid xenon (again at 1.4 T and 200 K). Such polarization-transfer experiments are not limited to enhancing the NMR signals of protons, however. By dissolving $^{13}CS_2$ in liquid laser-polarized xenon, it was shown that the ^{13}C NMR signal could be enhanced by a factor of 74 at 1.4 T.

2. *Preliminary High-Pressure Experiments*

The feasibility of using supercritical laser-polarized xenon as a polarizing solvent was also recently investigated (*53*). While requiring the use of high-pressure sample tubes, the super-critical phase offers many potential advantages, including improved solubility characteristics (*52, 125, 126*), higher and broader temperature range (generally more convenient for a variety of chemical and biophysical experiments), low viscosity (leading to narrow solute linewidth (*127–129*)), and highly "tunable" solvent characteristics (resulting from the extreme sensitivity of the properties of supercritical fluids to applied pressure changes (*126, 130*)).

Following early experiments using high-pressure Pyrex capillary tubes (which had to be pressure-checked frequently in order to guard against explosions), frozen laser-polarized xenon was collected in sapphire NMR tubes via cryopumping, then rapidly sublimated in warm water (in the fringe field of a magnet) prior to placement within the NMR magnet. This approach permitted supercritical laser-polarized xenon samples to be created at Berkeley with nuclear spin polarization of a few percent, with densities greater than 140 amagat. The polarization was ultimately limited by the initial polarization achieved in the continuous-flow device (typically 2–8%) and the time required to accumulate enough xenon for the experiment, as well as the numerous phase changes and temperature fluctuations required to transfer the xenon from the flow apparatus to the NMR magnet.

The T_1 of the supercritical laser-polarized xenon was shown to be several hundred seconds, in general agreement with previous work involving unpolarized xenon (*131*). Indeed, T_1 values of about 1000 s have recently been observed in supercritical laser-polarized xenon samples in the Berkeley laboratory.

V. "LIGHTING UP" THE NMR OF MOLECULES. II. SPECIFIC XENON-BINDING INTERACTIONS

A. Introduction

Xenon, while chemically inert, is known to participate in host–guest interactions with a variety of molecules. Xenon has been shown to bind to various proteins in crystals and in solution (*79, 86, 132–139*). The formation of xenon clathrates has also been investigated extensively with both thermally polarized and laser-polarized xenon (see, for example, Refs. (*140, 141*)). Studies using xenon dissolved in lipid vesicles as a model for anesthetic action showed that xenon is preferentially attracted to amphiphilic regions in lipid membranes (*142*). Finally, xenon forms inclusion compounds with various organic molecules possessing accessible cavities, including α-cyclodextrin, hemicarcerands, self-assembling dimers, calixarenes, and cryptophane-A (*140, 143–149*).

Many of the above experiments that probed xenon binding in molecules utilized the highly sensitive chemical shift of xenon in order to reveal properties of the xenon environment via ^{129}Xe NMR spectroscopy. Alternatively, NOE polarization transfer from molecular protons to neighboring ^{129}Xe spins can be achieved via selective irradiation of different ^{1}H resonances and subsequent detection of the ^{129}Xe resonance; this approach was employed to investigate xenon binding in α-cyclodextrin (*146*) and xenon preferential solvation in lipid vesicles (*142*). Such experiments have the advantage of providing direct microscopic information regarding the xenon surroundings (and incidentally, may aid in the interpretation of empirical xenon chemical shifts), but they rely on the weak intermolecular cross-relaxation between ^{129}Xe and the molecules being studied. Furthermore, selective irradiation in complex ^{1}H NMR spectra can be difficult to achieve, and 2D heteronuclear ^{1}H–^{129}Xe NOESY experiments would be enormously time-consuming. In the absence of laser polarization, the ^{1}H $\leftarrow$ ^{129}Xe NOE enhancement is minuscule ($\sim 10^{-5}$), resulting from low xenon concentration, as well as weak ^{129}Xe–^{1}H coupling. With the use of laser-polarized xenon, however, the ^{129}Xe–^{1}H SPINOE enhancement ($\sim 10^{-2}$–10^{-1}) can be directly observed in the resolved ^{1}H NMR sepctrum.

In two recent studies, the transient binding of laser-polarized xenon to organic molecules in solution produced differential enhancements in the ^{1}H NMR spectra resulting from distance-selective xenon-proton cross-relaxation. The degree of cross-relaxation was dictated by the proximity of a given proton to each molecule's xenon binding site, as well as the relative motion between the species involved (*36, 91*). These results suggest that SPINOE polarization transfer could be utilized to study structure and dynamics in molecules that interact with xenon, and to map their hydrophobic surfaces. SPINOE experiments could also be used to identify those regions of macromolecules and biological systems that are accessible to and interact with xenon atoms; thus, in light of xenon's anesthetic properties (*55, 56*), SPINOE spectroscopy may give new insight into the molecular mechanisms of general anesthesia (for a sampling of this controversial field, see, for example, Refs. (*150–153*)).

B. SPINOE Cross-Relaxation Rates and Xenon-Molecule Interactions

The values of xenon-proton cross-relaxation rates depend on the structural and dynamical characteristics of the intermolecular couplings between xenon and a given molecular environment. A molecule (M) may participate in various types of interactions

with a xenon atom, including nonspecific interactions (i.e., diffusive coupling, described in detail in the previous section), preferential solvation, and xenon binding (which results in the formation of a Xe : M complex) (*36*). Exchange phenomena are normally involved among these various situations, but such exchange is generally rapid with respect to both the proton and xenon auto-relaxation rates. Furthermore, proton chemical shifts are generally poorly sensitive to intermolecular interactions with xenon, and therefore in most cases, exchange is likely to be rapid with respect to the proton chemical-shift time scale. This conclusion implies that ^{1}H NMR spectra will not be resolved according to the solute-xenon interactions, and that observed ^{1}H SPINOE enhancements may result from a combination of interactions. Therefore, the experimental H-Xe cross-relaxation rate can be written generally as

$$\sigma_{\mathrm{H\,Xe}} = \sum_i \frac{[\mathrm{M}]_i}{[\mathrm{M}]_\mathrm{T}} \sigma^i_{\mathrm{H\,Xe}}, \qquad [33]$$

where i denotes the interaction mode, $[\mathrm{M}]_\mathrm{T}$ is the total concentration of the solute, $[\mathrm{M}]_i$ is the molar concentration of the solute involved in the ith interaction mode, and $\sigma^i_{\mathrm{H\,Xe}}$ is the H–Xe cross-relaxation rate associated with that mode.

For a dilute solution of xenon-binding molecules, one may consider two modes of interaction: diffusive coupling (governed by $\sigma^d_{\mathrm{H\,Xe}}$), which exists for any kind of solute molecule, and xenon binding (governed by $\sigma^b_{\mathrm{H\,Xe}}$):

$$\sigma_{\mathrm{H\,Xe}} = \sigma^d_{\mathrm{H\,Xe}} + \frac{[\mathrm{Xe : M}]}{[\mathrm{M}]_\mathrm{T}} \sigma^b_{\mathrm{H\,Xe}}. \qquad [34]$$

The form of Eq. [34] assumes that both molecules *without* included xenon and molecules *with* included xenon experience identical diffusive coupling with unbound xenon. [Xe : M] is the equilibrium molar concentration of the xenon : molecule complex. Hereafter, bound xenon is referred to as $\mathrm{Xe_{in}}$, whereas unbound xenon will be referred to as $\mathrm{Xe_{out}}$. Naturally, $[\mathrm{Xe : M}] = [\mathrm{Xe}]_\mathrm{in}$ for 1 : 1 complexes.

1. The Cross-Relaxation Rate Resulting from Xenon Binding

The time scale relevant to $^{129}\mathrm{Xe} \rightarrow {}^1$1H cross relaxation and polarization transfer is the correlation time, τ_r, for tumbling motion of the transient Xe-molecule pair; xenon binding implies that the lifetime of the complex is much greater than the correlation time for its overall tumbling motion. Xenon-molecule configurations that possess lifetimes significantly longer than the average residence time of xenon in the molecule's solvation shell, but are short-lived in the sense that they do not reorient as a whole, could be regarded as specific preferential solvation (*36*).

In cases of xenon binding, τ_r controls the dynamics of $\sigma^b_{\mathrm{H\,Xe}}$. Under these circumstances, the description of the Xe–H cross-relaxation rate reduces to the intramolecular case, and Eq. [27] of the previous section may be used with $\tau^b_c = \tau_r$ to obtain average distances between bound xenon and nuclear spins of the molecule that characterize the structure of the xenon-host complex. Of course, the validity of this treatment of experimental $\sigma^b_{\mathrm{H\,Xe}}$ data depends on the importance of internal dynamics of the molecule being studied. The consequences of internal motions of the host molecule, in addition to the motion of xenon within a binding site, are $\tau^b_c < \tau_r$ and $\langle r^{-6}_{\mathrm{H\,Xe}} \rangle^b$ values which may be difficult to interpret because they correspond to weighted averages over multiple configurations. Molecular dynamics simulations may prove helpful in such cases.

One can now estimate an upper bound for $\sigma^b_{\mathrm{H\,Xe}}$ using Eq. [27] in the previous section with $\omega\tau^b_c = 0.68$ (as suggested by the peak in Fig. 13a, which shows the dependence of $\sigma_{\mathrm{H\,Xe}}$ on the correlation time), and $\langle r^{-6}_{\mathrm{H\,Xe}} \rangle^b = (3.2\ \text{Å})^{-6}$ (an estimate for the xenon-proton minimum approach distance). Given a magnetic field of 9.39 T (in which the proton resonance frequency is about 400 MHz), Eq. [27] yields a $\sigma^b_{\mathrm{H\,Xe}}$ value of $3 \times 10^{-3}\ \mathrm{s}^{-1}$, a figure three orders of magnitude greater than the value expected for the cross-relaxation rate resulting only from diffusive coupling. Indeed, $\sigma^b_{\mathrm{H\,Xe}}$ values of this order have been observed for xenon bound to α-cyclodextrin in solution, as described below.

As shown in Fig. 13a, an increase in the correlation time from a few ps ($\omega_\mathrm{H}\tau_c = 0.01$–$0.02$ at 9.4 T) to a value corresponding to the maximum (with τ_c in the range 0.2–0.5 ns) gives rise to a ~20-fold increase in the cross-relaxation rate. However, such an increase in $\sigma_{\mathrm{H\,Xe}}$ would not necessarily translate into an increase in the observed SPINOE enhancement. For example, in real systems large enough to bind xenon, the increased correlation time characterizing the H–Xe dipolar interactions would generally be accompanied by a corresponding increase in the correlation time characterizing the H–H dipole–dipole interactions, and a concomitant reduction of proton auto-relaxation time.

2. Dependence of the Cross-Relaxation Rate on the Xenon Concentration

Previously, it was shown that to a good approximation, $\sigma^d_{\mathrm{H\,Xe}}$ is proportional to the concentration of unbound xenon. An additional concentration dependence of the experimental cross-relaxation rate may arise from the effect of the xenon concentration on the binding equilibrium. Based on the definition of the binding constant, K, for the equilibrium

$$\mathrm{Xe_{out}} + \mathrm{M} \rightleftharpoons \mathrm{Xe : M}, \qquad [35]$$

we obtain

$$\frac{[\mathrm{Xe : M}]}{[\mathrm{M}]_\mathrm{T}} = \frac{K[\mathrm{Xe}]_\mathrm{out}}{1 + K[\mathrm{Xe}]_\mathrm{out}}, \qquad [36]$$

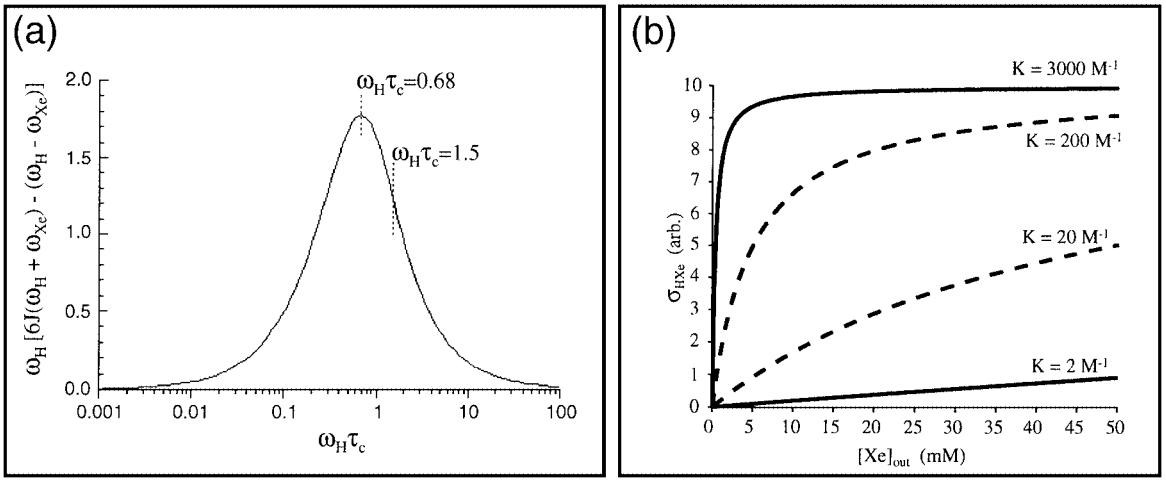

FIG. 13. (a) Illustration of the dependence of the ^{1}H–^{129}Xe cross-relaxation rate, σ_{HXe}, on the correlation time (*36*), where $\omega_H[6J(\omega_H+\omega_{Xe})-J(\omega_H-\omega_{Xe})]=6\omega_H\tau_c/[1+(|\gamma_{Xe}/\gamma_H|)^2\omega_H^2\tau_c^2]-\omega_H\tau_c/[1+(1-|\gamma_{Xe}/\gamma_H|)^2\omega_H^2\tau_c^2]$. Two points on the curve are marked; $\omega_H\tau_c\approx0.68$ corresponds to the curve's maximum, while $\omega_H\tau_c\approx1.5$ corresponds to the experimentally measured value for xenon in cryptophane-A at 9.4 T (described later in detail). (b) Dependence of σ_{HXe} originating from xenon binding on the equilibrium xenon concentration in the solvent for various association constants, K. Curves with solid lines are for systems that have been studied via SPINOE experiments (Xe/cyclodextrin in DMSO, $K=2$ M^{-1}; Xe/cryptophane-A in $(CDCl_2)_2$, $K=3000$ M^{-1}). The dotted curves, added for illustrative purposes, correspond to what would be expected for Xe/cyclodextrin in H_2O, $K\sim20$ M^{-1} (*146, 148*), and xenon/myoglobin or xenon/hemicarcerand, $K\sim200$ M^{-1} (*86, 143*).

which for weak xenon binding reduces to

$$\frac{[\text{Xe}:\text{M}]}{[\text{M}]_\text{T}}\approx K[\text{Xe}]_\text{out}, \qquad [37]$$

and for strong xenon binding and excess xenon reduces to

$$\frac{[\text{Xe}:\text{M}]}{[\text{M}]_\text{T}}\approx 1. \qquad [38]$$

Equations [36], [37], and [38] are written in terms of $[\text{Xe}]_\text{out}$ (and not as a function of the total xenon concentration) because for dilute solutions of host molecules, $[\text{Xe}]_\text{out}$ is well approximated by the equilibrium solubility of xenon in the pure solvent.

Consider the example of xenon binding to α-cyclodextrin. An equilibrium binding constant of ~2 M^{-1} has been reported for this system in dimethyl sulfoxide (DMSO) at 298 K (*146*). For an equilibrium xenon gas overpressure of 1 atm, the solubility of xenon in DMSO gives an equilibrium xenon concentration of 0.024 M at 298 K. Therefore, Eq. [37] applies to this system, and a linear increase in the SPINOE originating from binding is expected with increasing xenon pressures (at least for xenon pressure in the range of a few atm), as shown in Fig. 13b. However, in tetrachloroethane (for which the xenon solubility has been estimated to be $\sim$0.1 M/atm), the equilibrium constant for the binding of xenon to cryptophane-A was estimated to be larger than 3000 M^{-1} at 278 K (*149*), and therefore Eq. [38] is more appropriate (as shown in Fig. 13b). Using Eq. [30] from the previous section and Eq. [36], Eq. [34] can now be rewritten, taking into account the isotopic abundance of ^{129}Xe, A_{129}:

$$\sigma_{\text{H Xe}}=A_{129}\left[\sigma^n_{\text{H Xe}}[\text{Xe}]_\text{out}+\frac{K[\text{Xe}]_\text{out}}{1+K[\text{Xe}]_\text{out}}\sigma^b_{\text{H Xe}}\right]. \qquad [39]$$

C. The SPINOE in the Weak Xenon-Binding Limit: α-Cyclodextrin

One molecule shown to weakly bind xenon is α-cyclodextrin (*140, 146*), a cup-shaped six-membered cyclic oligosaccharide. Specifically, α-cyclodextrin transiently binds xenon within its hydrophobic pocket; cyclodextrins are well known in the chemical industry for their ability to bind a variety of chemical species for numerous applications (e.g., masking tastes and odors, delivering drugs, and catalyzing reactions) (*154–156*). As mentioned above, the association constant for xenon binding of α-cyclodextrin in DMSO was estimated to be ~2 M^{-1} at 298 K (*146*), well within the regime of weak binding as governed by Eq. [35].

When laser-polarized xenon was dissolved in a 0.1 M α-cyclodextrin/DMSO solution, one solution ^{129}Xe resonance was observed, consistent with xenon being in fast exchange between the solvent and the α-cyclodextrin (in agreement with previous results (*146*)). The ^{129}Xe was observed to rapidly decay with a spin–lattice relaxation time of $\sim$20 s, which indicated stronger dipolar interactions compared to benzene and *p*-nitrotoluene, in which the ^{129}Xe T_1 was observed to be greater than 500 s for a solution of 0.1 M *p*-nitrotoluene/d_6-benzene.

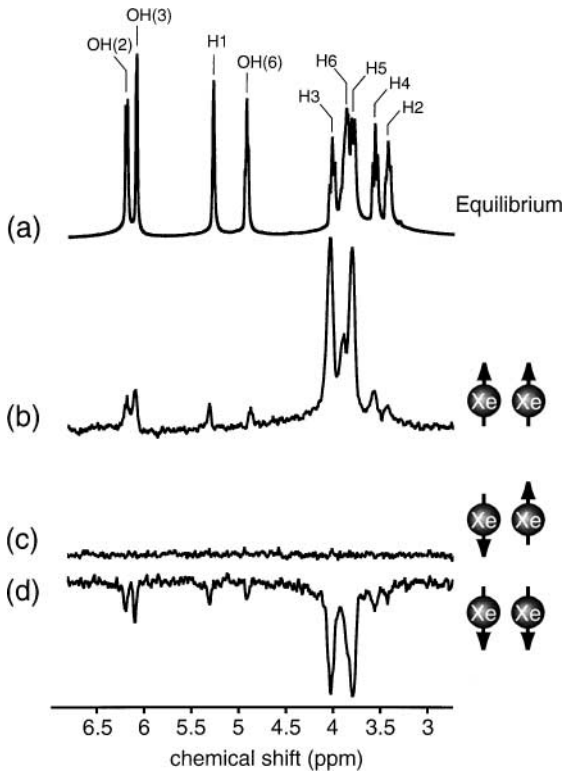

FIG. 14. ^{1}H NMR spectra taken from a 0.05-M dehydrated α-cyclodextrin/d_6-DMSO solution (*91*). (a) Equilibrium ^{1}H NMR spectrum with assignments (see Fig. 15). (b) ^{1}H SPINOE spectrum taken using the pulse sequence shown in Fig. 11a after introduction of "positively" polarized xenon. (c) Baseline spectrum recorded under circumstances similar to those in (b), but without the ^{129}Xe 180° pulse, demonstrating the suppression capability of the pulse sequence. (d) As in (b), but with "negatively" polarized xenon. Values of $\tau_1 = 0.63$ s and $\tau_2 = 0.37$ s were used to obtain the SPINOE spectra shown here.

The NMR pulse sequence shown in Fig. 11a was used to directly observe SPINOE enhancements of ^{1}H NMR signals of α-cyclodextrin. When laser-polarized xenon was dissolved in a 0.05 M solution of α-cyclodextrin in DMSO, selective enhancements in the ^{1}H SPINOE spectra were obtained (*91*); these results are shown in Fig. 14. Figure 14a shows an equilibrium ^{1}H NMR spectrum of α-cyclodextrin with assignments obtained from a 2D COSY spectrum and should be compared with the ^{1}H SPINOE spectra in Figs. 14b,14d. The most striking features of the spectra in Figs. 14b,14d are the relatively large SPINOE signals originating from the H3 and H5 protons of α-cyclodextrin. Interestingly, the H3 and H5 protons are the ones that reside on the inside of the hydrophobic pocket (shown in yellow in Fig. 15) and therefore would be expected to be the closest to bound xenon.

The measured ^{129}Xe–^{1}H cross-relaxation rates for the individual α-cyclodextrin protons, along with their respective T_1^{H} values, are summarized in Table 2; the results from the previous experiments involving the *p*-nitrotoluene/benzene solution are listed for comparison. Values for the cross-relaxation rates were calculated by fitting the data to Eq. [22] in the previous section. Because we are in the weak-binding limit (Eqs. [36] and [37]), the observed cross-relaxation rates are proportional to $[\mathrm{Xe}]_{\mathrm{out}}$; thus, we can obtain a concentration-independent cross-relaxation rate with the following relation,

$$\sigma^n_{\mathrm{H\,Xe}} = \frac{\sigma_{\mathrm{H\,Xe}}}{[\mathrm{Xe}]_{\mathrm{out}}}, \qquad [40]$$

where

$$\sigma_{\mathrm{H\,Xe}} \approx A_{129} \cdot K\,[\mathrm{Xe}]_{\mathrm{out}} \cdot \sigma^b_{\mathrm{H\,Xe}}. \qquad [41]$$

From the table it can be seen that the transient binding of xenon to α-cyclodextrin produced cross-relaxation rates over two orders of magnitude higher than those observed between xenon and *p*-nitrotoluene or benzene, for which the cross-relaxation is modulated only by diffusive motion. More recently, the Virginia group inferred a collective value for the xenon/α-cyclodextrin cross-relaxation rate, $\sigma^c_{\mathrm{H\,Xe}} = 1.2 \times 10^{-5}$ s^{-1} mM^{-1}, by measuring the ^{129}Xe relaxation time of laser-polarized xenon dissolved in deuterated water (*157*); this value is in reasonable agreement with a sum of the values presented in Table 2. This increase in couplings between xenon and α-cyclodextrin arising from xenon binding demonstrates the sensitivity of the cross-relaxation rate to the binding of xenon with molecules

TABLE 2
Xenon–Proton Cross-Relaxation Rates and Proton Spin–Lattice Relaxation Times (*97*)

Molecule	Proton	σ^n_{HXe} (10^{-6} s^{-1} mM^{-1})	T_1 (s)
d_5-Benzene	H	0.028 ± 0.007	110
p-Nitrotoluene	CH_3	0.025 ± 0.007	6.8
	H3, H5	0.032 ± 0.006	35
	H2, H6	0.028 ± 0.005	23
α-Cyclodextrin	H1	0.44 ± 0.14	1.1
	H2	1.3 ± 0.5	1.1
	H3	4.1 ± 0.8	1.2
	H4	1.6 ± 0.3	1.1
	H5	4.9 ± 1.2	0.87
	H6	1.2 ± 0.4	0.78
	OH(2)	0.70 ± 0.22	1.2
	OH(3)	0.86 ± 0.18	1.0
	OH(6)	0.36 ± 0.14	1.1

Note. The cross-relaxation rates are reported here as partial millimolar cross-relaxation rates (σ^n_{HXe}) in order to account for the different xenon concentrations present in the experiments. In the absence of strong binding, the observed cross-relaxation rates will be proportional to the xenon concentration. The data for the first four rows were obtained from the *p*-nitrotoluene/benzene experiments described in the previous section and are listed here for comparison; the values for d_5-benzene were taken from the solvent in those experiments. The error range for the T_1 measurements was ±5%.

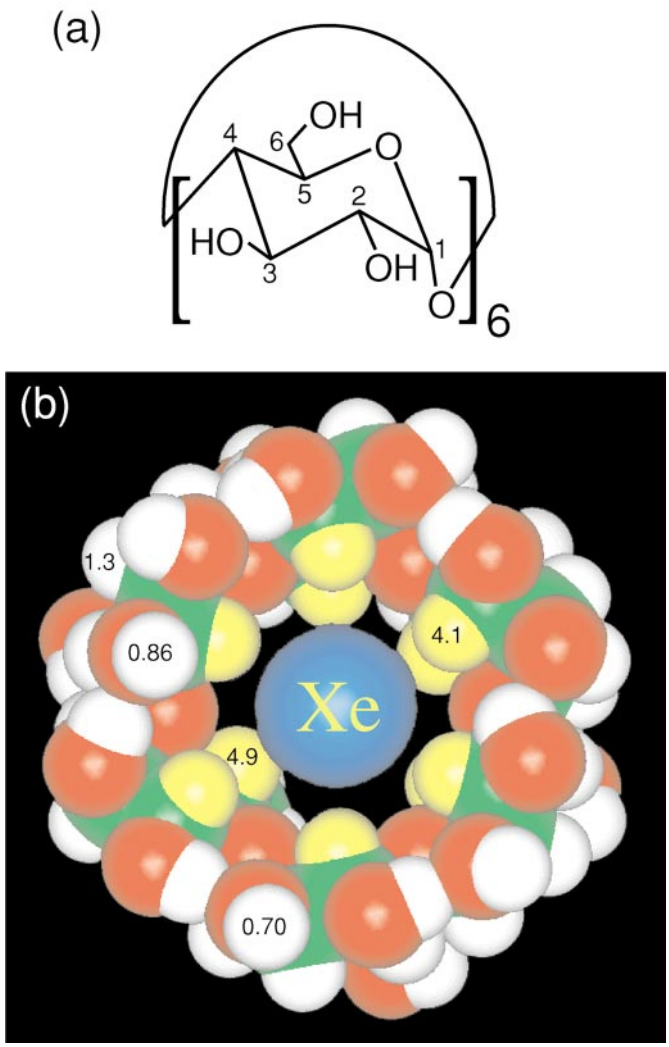

FIG. 15. (Color) (a) Structural formula of α-cyclodextrin. (b) Laser-polarized xenon in the hydrophobic pocket of α-cyclodextrin (shown as a CPK model based upon X-ray crystallographic data (*158*); color scheme: oxygen atoms (red), carbon atoms (green), hydrogen atoms (white), with the spectrally enhanced H3 and H5 atoms shown in yellow). In this "top" view of the complex, the six H3 atoms comprise the closer of the two rings of hydrogen atoms within the hydrophobic pocket. The numbers correspond to measured partial millimolar xenon-proton cross-relaxation rates as given in Table 2.

in solution. Furthermore, as suggested by Eq. [27] the relative values for $\sigma_{\mathrm{H\,Xe}}$ reflect the proximity of the respective protons of α-cyclodextrin to the xenon binding site. For example, assuming $\sigma_{\mathrm{H\,Xe}} \propto r_{\mathrm{H\,Xe}}^{-6}$, a ratio of 1 : 1.5 can be estimated for the range of distances between Xe–H5 and Xe–H1 (neglecting ^{1}H–^{1}H polarization transfer via "relayed" SPINOEs (*36*)). From an X-ray structure of α-cyclodextrin (*158*), this value is consistent with a distribution of xenon locations within the hydrophobic pocket, which predicts a value between 1 : 1.2 and 1 : 2. These ratios correspond to Xe–H5 distances of about 3 to 6 Å and Xe–H1 distances of about 6 to 8 Å.

D. The SPINOE in the Strong Xenon-Binding Limit: Cryptophane-A

More recently, SPINOE experiments were performed on cryptophane-A in solutions of 1,1,2,2-tetrachloroethane (*36*). The binding of laser-polarized xenon to cryptophane-A produced selective enhancements in the ^{1}H SPINOE spectra, permitting experimentally derived ^{1}H–^{129}Xe cross-relaxation rates to be correlated with internuclear distances. Furthermore, comparison of the values measured for the cross-relaxation rates with computational models permitted the determination of the preferred conformations of the cryptophane-A molecule when participating in xenon binding.

Cryptophane-A (Fig. 16) is an approximately spherical, cage-like organic molecule composed of two cyclotriveratrylene bowls connected by three OCH_2CH_2O spacer bridges. Cryptophane-A belongs to the D3 group of symmetry.

In previous work by Reisse, Collet, and co-workers, cryptophane-A was shown to bind xenon very strongly, with an association constant greater than 3000 M^{-1} in 1,1,2,2-tetrachloroethane (*149*). Unlike the complexes of xenon and hemicarcerands (which exhibit association constants on the order of $\sim$200 M^{-1}) (*143*), the Xe/cryptophane-A complex is formed without a high degree of constrictive binding (i.e., trapped xenon is not required to overcome large steric constraints of the portals of cryptophane-A in order to escape confinement), giving xenon residence times on the order of milliseconds instead of hours (*149*). The relative mobility of the spacer bridges permits cryptophane-A to adopt various conformations that affect the size of the cavity and the stability of the host-guest complex; the dynamics of the host are expected to influence the manner in which the guest is bound and released (*159*).

1. Spin–Lattice Relaxation Times of ^{129}Xe and ^{1}H

The ^{129}Xe NMR spectrum in Fig. 16b was obtained with a single scan using an RF pulse of small tipping angle ($\approx$2.5°) following dissolution of laser-polarized xenon in a 0.05 M cryptophane-A/$(CDCl_2)_2$ solution. As shown in the spectrum, the exchange of xenon between cryptophane-A and the solvent is slow with respect to the NMR time scale, in agreement with previous results (*149*). The ^{129}Xe spectrum exhibits two lines separated by $\sim$160 ppm and considerably broadened from chemical exchange. The higher field signal corresponds to the xenon trapped within the cavity of cryptophane-A (Xe_{in}), with a chemical shift $\sim$60 ppm downfield with respect to the xenon gas resonance extrapolated to zero pressure. The second (down-field) peak corresponds to xenon in the solvent (Xe_{out}). Given the molar fraction of Xe_{in}, one can estimate the intrinsic T_1 of bound xenon to be T_1^{obs}. $[Xe_{in}/(Xe_{in} + Xe_{out})] = 16.4$ s, again suggesting significant cross-relaxation between bound xenon and the protons of cryptophane-A.

The ^{1}H T_1 values for cryptophane-A are listed in Table 3. The longest relaxation times, $\sim$0.8 s, are those of the methoxy and aromatic hydrogens. Therefore, relaxation of ^{129}Xe in this

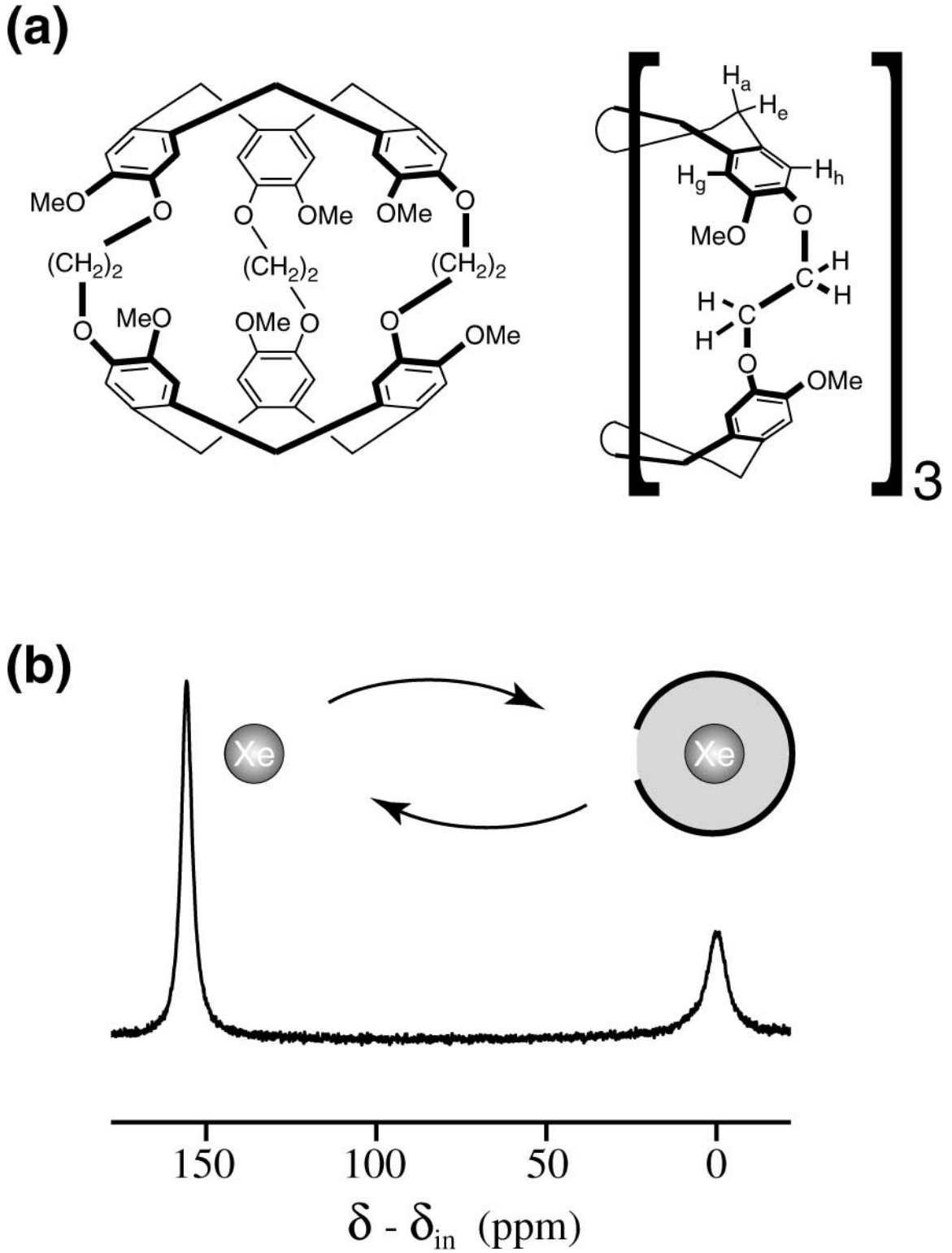

FIG. 16. (a) Structural formula of cryptophane-A, and atom labeling used in the ^{1}H NMR spectrum of Fig. 17. (b) Typical ^{129}Xe NMR spectra for laser-polarized xenon dissolved in cryptophane-A/$(CDCl_2)_2$ solution (*36*). The spectrum was acquired with one scan using a pulse of small tipping angle ($\approx$2.5°). The ^{129}Xe spectrum is referenced to the signal corresponding to xenon bound to cryptophane-A (Xe_{in}). A second signal can be seen roughly 160 ppm downfield from that of Xe_{in}, corresponding to unbound xenon residing in the $(CDCl_2)_2$ solvent (Xe_{out}). ^{129}Xe was in considerable excess for these experiments, as reflected by $[Xe_{in}] < [Xe_{out}]$.

TABLE 3

Spin–Lattice Relaxation Times, SPINOE Enhancements, Relative H–Xe Cross-Relaxation Rates, and Calculated Relative Values in *Gauche* Conformations for the Protons of Cryptophane-A (*36*)

Protone	Label	T_1^H	SPINOE (%)	$\sigma^b_{HXe}/\sigma^b_{H_{g,h}Xe}$	$\langle r^{-6}_{HXe}\rangle/\langle r^{-6}_{H_{g,h}Xe}\rangle$
Aromatic	H_g, H_h	0.80	11.0	(1.00)	(1.00)
Axial	H_a	0.27	3.0	0.47	0.3–0.4
Linker	H_j, $H_{j'}$	0.36	5.2	0.67	0.3
Linker	H_k, $H_{k'}$	0.41	13.0	1.55	1.5–1.8
Methoxy	Me	0.83	2.6	0.23	0.1–0.3
Equatorial	H_e	0.35	2.7	0.35	0.3–0.4

system is slow with respect to ^{1}H relaxation, and thus Eq. [22] of the previous section can be used to describe $^{129}Xe \rightarrow {}^1H$ SPINOE polarization transfer. Finally, selective CW-driven ^{1}H–^{1}H NOE experiments were performed, permitting the rotational correlation time of the complex to be estimated (≈600 ps). Thus as Fig. 13a indicates, σ^b_{HXe} values approximately 70% of the maximum value can be expected for xenon bound to cryptophane-A.

2. *Measurement of the Cross-Relaxation Rates*

The equilibrium ^{1}H NMR spectrum of the cryptophane-A solution is shown with assignments (*149*) in Fig. 17a (the proton NMR signals of the spacer bridges (which comprise an AA′BB′ spin system) are discussed in greater detail below). Figures 17b–17d respectively show SPINOE spectra obtained with positively laser-polarized xenon, with thermally polarized xenon, and with negatively laser-polarized xenon. As observed previously in α-cyclodextrin, the relative intensities in the SPINOE spectra obtained with laser-polarized xenon (Figs. 17b,17d) are strikingly different from those in the equilibrium spectrum. While the equilibrium spectrum is dominated by the signal of the methoxy group, the signal from the aromatic protons is the most intense in the SPINOE spectra of Figs. 17b,17d. The ^{1}H signal enhancements observed in Fig. 17b varied between 3% and 13% (see Table 3). Additionally, the selectivity of the SPINOE was clearly not simply the result of vastly different ^{1}H auto-relaxation times, as the T_1^H values were nearly equal for the methoxy and aromatic protons.

From the experimental data given in Table 3, and estimated values for the xenon polarization enhancement, σ_{HXe}/A_{129} was estimated to be $\sim 1.2 \times 10^{-4}$ s^{-1} for the aromatic protons. From multiple experiments, σ_{HXe}/A_{129} values varying from $(1-4) \times 10^{-4}$ s^{-1} were found for the aromatic protons. This figure is two orders of magnitude greater than the value expected for H–Xe cross-relaxation rates originating from diffusive coupling alone; as with the case of α-cyclodextrin, the observed SPINOE enhancements can therefore be considered as originating entirely from the binding of laser-polarized xenon. Furthermore, the SPINOE spectra were obtained with dissolved xenon in excess with respect to the cryptophane-A concentration. Under these circumstances Eq. [38] is valid, thus giving $\sigma_{HXe}/A_{129} = \sigma^b_{HXe}$ from Eq. [39].

3. *^{129}Xe–^{1}H Cross-Relaxation Rates in Cryptophane-A vs α-Cyclodextrin*

The largest σ^b_{HXe} values resulting from the binding of xenon to cryptophane-A were measured to be 5- to 10-fold smaller than the corresponding values resulting from xenon binding to α-cyclodextrin (*91*). However, it is unlikely that this discrepancy originates from differences in the dynamics of the $^{129}Xe \rightarrow {}^1H$ polarization transfer. As shown previously, for the binding of xenon to cryptophane-A in $(CDCl_2)_2$ at room temperature, each σ^b_{HXe} should reach 70% of its maximum possible value in terms of τ_c. Instead, this difference in the magnitude of the σ^b_{HXe} values suggests differences in the structure of these xenon complexes. Given $\tau_c^b = 0.6$ ns and $\sigma^b_{HXe} = (1-4) \times 10^{-4}$ s^{-1}, Eq. [27] of the previous section gives a value for $\langle r^{-6}_{HXe}\rangle^b$ varying over $(0.5-2) \times 10^{-4}$ Å^{-6}; this range of values gives an average distance between the aromatic protons and the xenon atom of 4.1–5.2 Å. These results are in good agreement with computer

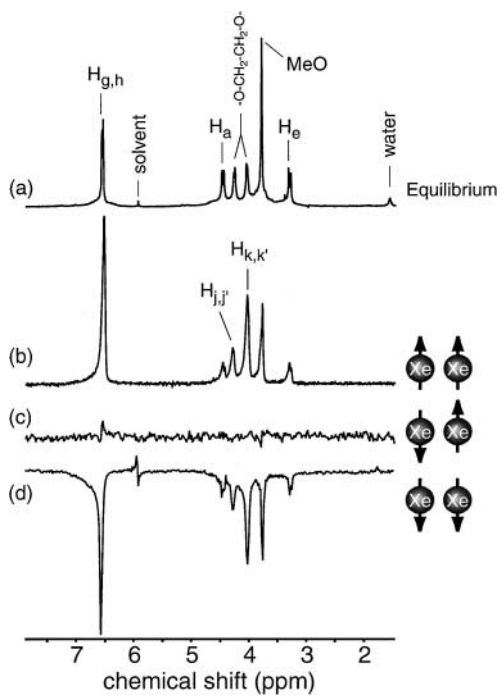

FIG. 17. ^{1}H SPINOE spectra of cryptophane-A. (a) ^{1}H NMR equilibrium spectrum of 0.05-M cryptophane-A in $(CDCl_2)_2$ with chemical shift assignments. (b) ^{1}H SPINOE spectrum acquired with the pulse sequence shown in Fig. 11a following introduction of positively polarized ^{129}Xe to the solution. (c) As in (b), but with ^{129}Xe at thermal equilibrium, demonstrating virtually complete suppression of all contributions to the ^{1}H NMR signal. (d) ^{1}H SPINOE spectrum acquired during a second experiment in which negatively polarized ^{129}Xe (prepared by inverting the direction of the magnetic field in which the ^{129}Xe is laser-polarized) was used, resulting in a corresponding sign change in the ^{1}H SPINOE spectrum. Values of $\tau_1 = 315$ ms and $\tau_2 = 185$ ms were used for the SPINOE experiments shown. Figure adapted from Ref. (*36*).

modeling of minimum-energy structures of the xenon/cryptophane-A complex, which predicted average xenon-proton internuclear distances of 4.5–4.8 Å. In comparison, an X-ray structure of α-cyclodextrin (*158*) can be used to predict r_{HXe} values between a xenon atom positioned at the center of the cavity and the nearest protons to be in the range of 3.2–3.8 Å. These calculated ranges of proton-to-xenon distances would correspond to a 4- to 8-fold factor increase in the cross-relaxation rates for α-cyclodextrin compared to those of cryptophane-A (neglecting dynamical effects), in agreement with the experimental observations.

TABLE 4

Experimental H–Xe Cross-Relaxation Rates (Bold) for the Protons of the Spacer Bridges of Cryptophane-A Relative to the Value for the Aromatic Protons, and Relative $\langle r^{-6}\rangle^b$ Values Calculated Using the Structures in Fig. 18

	Proximal H′s	Remote H′s
Experimental	**1.55**	**0.67**
Anti (a)	5.2	0.5
Anti (b)	4.4	0.5
Gauche (c)	1.8	0.3
Gauche (d)	1.5	0.3

4. Relative σ_{HXe} Values and the Structure of the Complex

As discussed above, the observed SPINOE enhancement for the aromatic protons is clearly consistent with xenon binding within the cavity of cryptophane-A. Nevertheless, detailed information regarding the structure of the xenon/cryptophane-A complex can be obtained in the absence of information about the *absolute* values of σ_{HXe}; furthermore, the use of relative H–Xe cross-relaxation rates avoids the uncertainty attached to the measurement of the absolute xenon polarization enhancement in these experiments.

Table 3 gives the σ^b_{HXe} values of the cryptophane-A protons relative to that measured for the aromatic protons. From this data it is clear that the binding of xenon to cryptophane-A gives rise to differential ^{1}H–^{129}Xe dipolar interactions. Provided that internal dynamics do not contribute significantly to the fluctuations of the intermolecular dipole–dipole interactions, the relative σ^b_{HXe} values listed in Table 3 reveal structural information regarding the xenon/cryptophane-A complex. Of particular interest are the results obtained for the protons belonging to the OCH_2CH_2O spacer bridges (also referred to as linkers). Indeed, one pair of these protons (labeled H_k and $H_{k'}$ in the spectrum of Fig. 17b) experiences, in the presence of xenon, a cross-relaxation rate more than twice as great as that between xenon and the other pair of protons (H_j and $H_{j'}$). Because the dynamics of both pairs of protons are most likely to be similar, these results indicate that H_k and $H_{k'}$ are, on average, closer to the xenon atom than H_j and $H_{j'}$.

While cryptophane-A is a somewhat rigid molecule, the internal degrees of freedom associated with the OCH_2CH_2O spacer bridges permit the molecule to adopt various conformations. Specifically, these conformations differ in the dihedral angle O–CH_2–CH_2–O and, in reference to the oxygen atoms, are either *gauche*-like or *anti*-like in nature.

Minimum-energy structures of the xenon/cryptophane-A complex were created via computer modeling. Four such structures are shown in Fig. 18 for different conformations of the displayed spacer bridge. In Figs. 18a,18b, the linkers are in an *anti* conformation. These conformations possess C_2 symmetry axes which bisect the C–C bond of the linkers and intercept at the center of the cavity where the xenon atom is found. Therefore, in Fig. 18a the protons labeled H and H′ have the same chemical shift which, *a priori*, is different from the chemical shift of the other pair of protons. The structures shown in Figs. 18b–18d were created based on the structure in Fig. 18a, with the labels unchanged; i.e., the H and H′ which were "remote" with respect to the xenon atom in Fig. 18a are the "proximal" protons in Fig. 18b. In both of these *anti* conformations, the proton–xenon distances are nearly equal, and consequently yield similar relative values for $\langle r^{-6}_{\mathrm{HXe}}\rangle^b$. From Table 4 it can be clearly observed that the calculated values for the "proximal" H′s in the *anti* conformations are significantly different from the corresponding experimental result; even if it were considered that both *anti* structures were present simultaneously (therefore giving weighted-average values for σ^b_{HXe}), the experimental results could not be properly explained.

In Figs. 18c,18d, the linkers are in a *gauche* conformation. These structures do not possess C_2 symmetry axes, but for each of them an equivalent structure exists in which the position of the protons H and H′ are interchanged. Therefore, for each pair of protons, $\langle r^{-6}_{\mathrm{HXe}}\rangle^b$ must be calculated as the average between the two protons. It is worth noting that in both of these *gauche* structures, the partner of the proton which is the nearest to xenon is actually the farthest proton; nevertheless, in Table 4 this pair is still referred to as the "proximal" protons, because it leads to the greater value $\langle r^{-6}_{\mathrm{HXe}}\rangle^b$. Thus, the H and H′ which are "remote" with respect to the xenon atom in Fig. 18c become the "proximal" protons in Fig. 18d. From Table 4, it can be seen that both *gauche* structures lead to relative $\langle r^{-6}_{\mathrm{HXe}}\rangle^b$ values in good agreement with the experimental results. Both of these *gauche* structures might be present simultaneously, but if this is the case, one conformation must be in considerable excess in order to explain the observed difference in cross-relaxation rates between the proton pairs.

The relative values for $\langle r^{-6}_{\mathrm{HXe}}\rangle^b$ of the various protons of cryptophane-A calculated using the *gauche* structures are shown in the last column of Table 3. It was necessary to calculate the value for the methoxy group for numerous positions of these protons; the calculation leads to values in agreement with the experimental relative cross-relaxation rates, despite the fact that the dynnamics of the polarization transfer might be somewhat different in this case.

The calculations shown here neglect the effects of relayed SPINOEs, which in the present system might be on the order

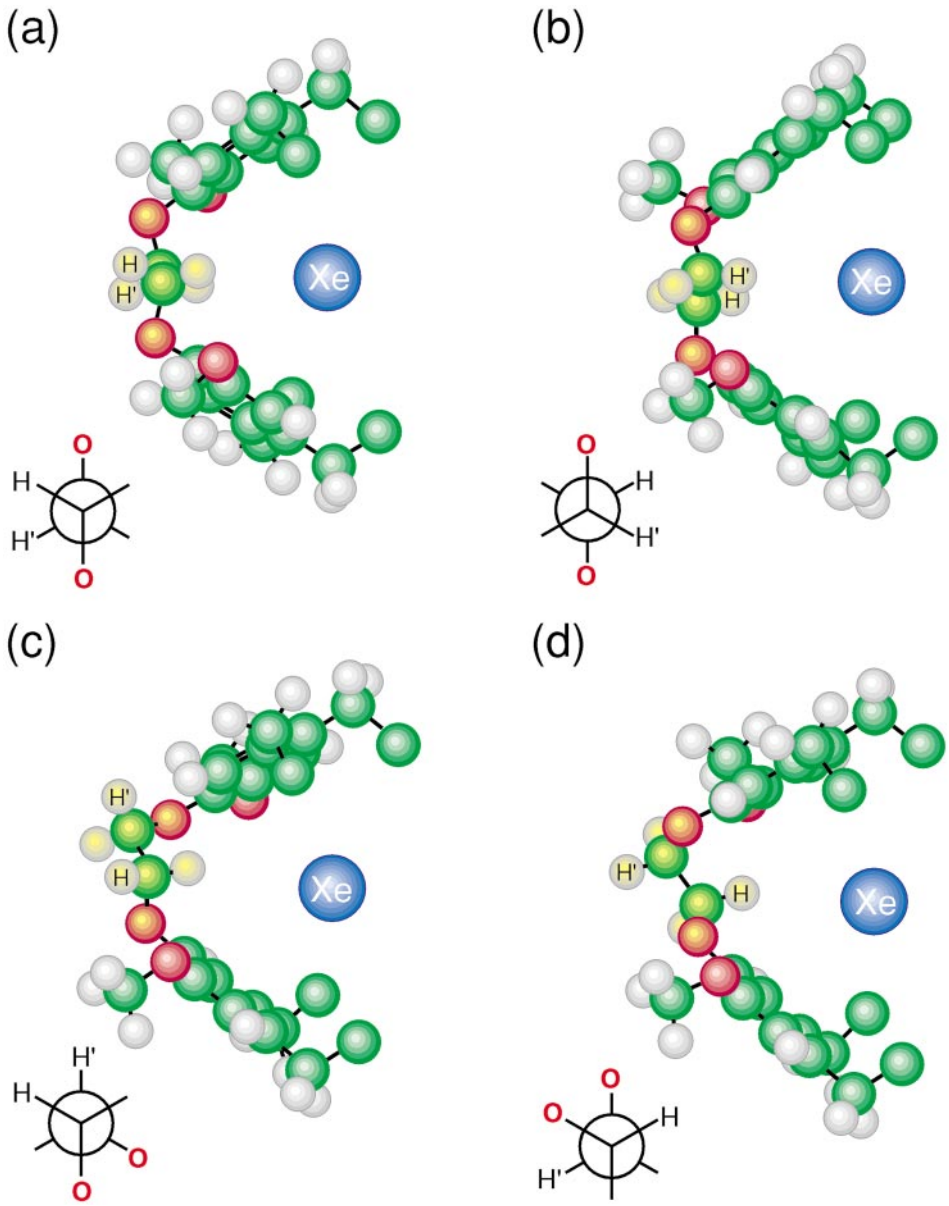

FIG. 18. (Color) Minimum energy structures of cryptophane-A with bound xenon for the various conformations of the displayed spacer bridge (highlighted with yellow tint) (*36*). The atoms of the cyclotriveratrylene subunits are at similar positions in each view; the molecule is slightly rotated from (a) to (d) to make the spacer bridge more clearly visible. In (a) and (b), the linkers are in an *anti* conformation. In (c) and (d), the linkers are in a *gauche* conformation.

of 10–15% between geminal protons (for a detailed explanation of relayed SPINOEs, see Ref. (*36*). Nevertheless, on the basis of the experimental SPINOE cross-relaxation rates, one can conclude that the most probable conformation of the spacer bridges of cryptophane-A when the molecule complexes xenon (in $(CDCl_2)_2$ at room temperature) is a *gauche* conformation. This conclusion is in agreement with the simulation of resolution-enhanced ^{1}H NMR signals performed previously (*149*). Additionally, one can conclude from these results that the chemical shifts of $H_{k,k'}$ and $H_{j,j'}$ characterize the protons of the spacer bridges of cryptophane-A which are, respectively, *gauche* and *anti* with respect to the vicinal oxygen atom; thus, the SPINOE results have permitted a more complete assignment of the ^{1}H NMR spectrum.

E. Xenon and Proteins

Both the α-cyclodextrin and cryptophane-A experiments suggest that SPINOE polarization transfer can be useful for directly probing the structure and dynamics of molecules that interact with xenon; the prospect of using SPINOE experiments to study proteins is particularly tantalizing. For example, because many

of the xenon binding sites in proteins (e.g., myoglobin (*134*) are not solvent-accessible, it is believed that xenon binding may require cooperative motion on the part of the protein in such cases. Thus, SPINOE experiments may shed light on dynamic binding processes between ligands and proteins.

Considerable work has been dedicated to studying xenon binding to various proteins in crystalline, solution, and lyophilized solid forms (*79, 86, 132–139, 157, 160, 161*). Much of the recent work studying xenon-binding in proteins has been motivated by the desire to map hydrophobic sites, and also to use xenon/protein complexes as highly isomorphous heavy-atom derivatives for solving the phase problem in X-ray structure determination (*136–138*).

Hemoglobin and myoglobin were the first two proteins shown to bind xenon (*79, 86, 132–134*). Hemoglobin is currently more difficult to study via NMR because of its large size (~80 kDa); the large number of protons and the broad spectral features resulting from slow molecular tumbling have (to date) precluded a complete structural assignment of hemoglobin's NMR spectra. Moreover, large proteins would be poor choices of model systems for SPINOE studies in general because proton–proton spin diffusion grows more efficient with increased molecular weight. Such spin diffusion would tend to "wash out" any selectivity of the SPINOE by bleeding polarization from the "lit up" protons neightboring bound laser-polarized xenon to the rest of the protons in the protein. Myoglobin, on the other hand, has a mass of "only" about 18 kDa, and it has been well-characterized via NMR methods (see, for example, Ref. (*162*)), facilitating the interpretation of proposed SPINOE experiments. Moreover, myoglobin is known to bind xenon relatively strongly in solution (~2–6 specific sites as indicated by both NMR and X-ray crystallography, depending on the experimental conditions), with $K \sim 200\ \mathrm{M}^{-1}$ for its strongest binding site (*86*); the corresponding value for hemoglobin is only about $10\ \mathrm{M}^{-1}$ (*86*).

Unfortunately for studies involving laser-polarized xenon, myoglobin possesses a paramagnetic center (specifically, the heme iron) that is believed to cause rapid xenon relaxation in solution. For example, a value for the ^{129}Xe T_1 of ~0.1 s has been observed in concentrated aqueous solutions of metmyoglobin (Fe^{3+}, $S = 5/2$) (*163*). More recently, the Virginia group measured a ^{129}Xe T_1 of 1.3 s in a low concentration (100 μM) solution of myoglobin.

The Florida group recently used laser-polarized ^{129}Xe NMR to probe the interaction between adsorbed xenon and the surfaces of lyophilized protein solids (e.g., metmyoglobin, methemoglobin, hen egg white lysozyme, and soybean lipoxygenase) (*160, 164*). One future goal of this work is to achieve polarization transfer (e.g., via SPINOE) from laser-polarized xenon to such proteins in the solid state by taking advantage of previously developed continuous-flow/SPINOE OPMAS techniques already used to probe materials surfaces (described in detail in Section VI).

Recent studies (*157, 161*) have investigated the possibility of using apomyoglobin (formed by removing the heme from the protein, for example, via reverse-phase HPLC) as a protein model for SPINOE polarization transfer in solution. The Virginia group was unable to detect any ^{129}Xe signal from a moderately high-concentration (5 mM) apomyoglobin solution 10 s after mixing laser-polarized xenon with the solution, suggesting a short ^{129}Xe T_1 under these conditions. The Berkeley group was recently able to measure a ^{129}Xe T_1 for a 1 mM apomyoglobin solution of 15.0 s at 7 T (*161*). This decay time should be long enough to permit the observation of small enhancements of the protein's NMR spectrum (provided the protein concentration is not too small to obtain a detectable SPINOE signal). This work also provided evidence of *nonspecific* interactions between xenon and the surface of myoglobin from the dependence of the ^{129}Xe shift on the xenon and protein concentrations (as well as the ^{129}Xe T_1's measured under folded and denaturing conditions), demonstrating the potential for xenon to probe protein/solvent interfaces.

Regardless which proteins are eventually studied via SPINOE methods (see 'Note added in proof') it is likely that selective or stochastic deuterium labeling may be needed to suppress spin diffusion and aid in interpretation of any observed SPINOE enhancements in the protein's ^{1}H NMR spectra. If such experiments prove successful, future work will also investigate the feasibility of actively transferring SPINOE magnetization from directly affected protons to other spins via more traditional NMR methods in order to improve the interpretability and information content of SPINOE experiments.

VI. ENHANCED NMR SPECTROSCOPY OF MATERIALS SURFACES

A. Introduction

NMR can be a powerful means of probing the morphology, molecular structure, dynamics, and chemical properties of surfaces of heterogenous materials under a wide range of experimental conditions. However, the NMR signals from the surfaces of low surface-area materials can often be difficult to observe, not only because the number of spins contributing to the surface signal may be extremely small (especially in light of the inherently low sensitivity of NMR in general), but also because the surface signal may in many circumstances be virtually indistinguishable from that of the bulk. Therefore, methods capable of increasing both the sensitivity and selectivity of the NMR of surfaces are highly desirable.

Adsorbed (thermally polarized) ^{129}Xe has long been used as a sensitive magnetic resonance probe of pore sizes and chemical properties of high-surface area materials like zeolites (for review, see Refs. (*67, 68, 80, 81, 83*)). For example, the measured value of xenon's highly sensitive chemical shift can be empirically correlated with the number of xenon atoms located within a given cavity of a zeolite, providing information about available void space within the zeolite, as well as the localization and type of guest species within the zeolite's pores. By their nature, such

studies would normally be limited to materials with very high surface area (and short xenon spin–lattice relaxation times) to compensate for the otherwise weak signal from the relatively low number of surface-adsorbed xenon spins.

An additional complication when using ^{129}Xe NMR to probe a material's surface arises from the fact that the adsorbed ^{129}Xe chemical shift can be very sensitive to xenon–xenon interactions, giving a xenon concentration dependence to the observed shift; often, one must perform multiple studies with varying xenon coverages to extrapolate the ^{129}Xe chemical shift to zero xenon concentration. Therefore, in some circumstances it would be advantageous to perform ^{129}Xe NMR studies with the minimal xenon coverage required to obtain sufficient signal-to-noise.

In this section, numerous examples of OPNMR of materials surfaces are described, including enhanced ^{129}Xe NMR signals from adsorbed laser-polarized xenon, and the direct enhancement of NMR signals of surface spins via polarization transfer (especially within the context of more conventional NMR techniques commonly used in solid-state experiments, such as variable-temperature studies, cross-polarization, and magic-angle spinning). Additional reviews of the application of laser-polarized xenon for enhancing the NMR of materials surfaces can be found in Refs. (*26, 37, 67, 68*).

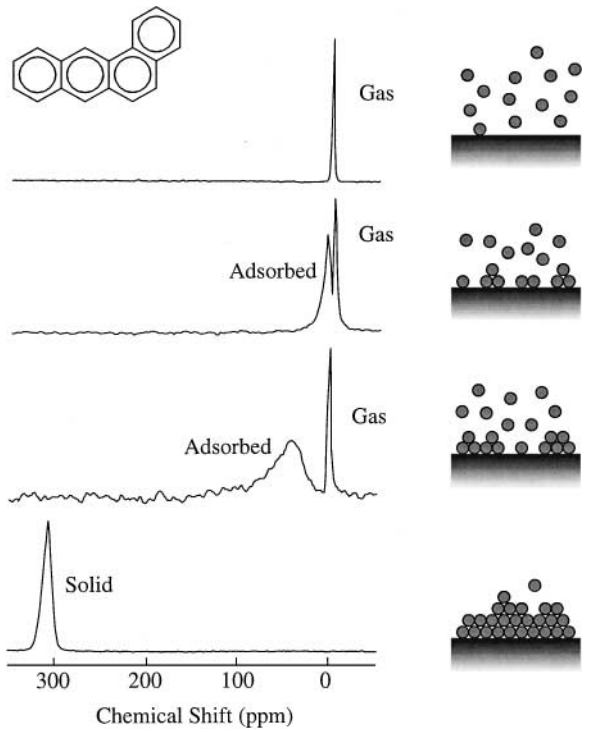

FIG. 19. ^{129}Xe NMR spectra of laser-polarized xenon adsorbed onto powdered benzanthracene (*35*). (a) Spectrum showing only gaseous xenon (298 K, 20 torr). (b,c) Spectra showing both gaseous and adsorbed xenon (158 K, 21 torr for (b), 153 K, 22 torr for (c)). (d) Spectrum showing only solid xenon (123 K). Figure courtesy of Thomas Meersmann.

B. Probing Surfaces with ^{129}Xe OPNMR

Soon following the work at Princeton investigating the production and relaxation behavior of frozen laser-polarized xenon (*39*), experiments at Berkeley (*35*) showed that adsorbed laser-polarized xenon could be a sensitive NMR probe of low surface-area materials. In this work, a batch optical pumping apparatus (similar to that shown in Fig. 4) was employed to produce small quantities of laser-polarized xenon and deliver it to samples of low surface-area materials within an NMR magnet. This early OP apparatus utilized a 30-mW diode laser, which could produce laser-polarized xenon with a polarization enhancement factor of about 750 (limited primarily by the laser power).

At room temperature and low xenon overpressure (about 20 torr), it was shown that NMR signals from adsorbed xenon could be observed from particles of graphitized carbon and Na–Y zeolite. The graphitized carbon particles, which possessed a moderately small surface area (10 m^2/g), shifted the resonance of the adsorbed xenon about 10 ppm downfield from the gas resonance. The signal for xenon adsorbed in the zeolite was shifted 59 ppm downfield from the gas resonance produced by 16 torr of xenon; at the time, this was the lowest xenon pressure reported for such xenon adsorption NMR experiments.

Similar experiments were also performed on particles of powdered benzanthracene, which possessed a low surface area of only $\sim$0.5 m^2/g (the particle size was determined from electron micrographs) (*35*). These results are shown in Fig. 19. At room temperature (Fig. 19a), only the signal from gaseous xenon could be observed in the ^{129}Xe NMR spectra. However, lowering the sample temperature to 158 K produced a second resonance 10 ppm downfield from the gas resonance (Fig. 19b), attributed to laser-polarized xenon adsorbed on the benzanthracene particles. Lowering the temperature five degrees further increased the shift to 32 ppm, and significantly changed the lineshape of the adsorbed xenon resonance (Fig. 19c), possibly resulting from the distortion of the electron clouds of the adsorbed xenon atoms. Overall, the chemical shift and linewidth were observed to increase with decreasing temperature, which is characteristic of increased residence time and decreased mobility for the adsorbed xenon. Finally, once the temperature was lowered to 123 K, only the signal from solid laser-polarized xenon could be observed (Fig. 19d).

Many typical amorphous solid materials have relatively large particle sizes ($\sim$10 μm) giving them low surface areas ($\sim$1 m^2/g); thus, these results suggested that a wide variety of materials of interest in catalysis and surface science could be studied with laser-polarized xenon NMR. Moreover, the authors stated that it should be possible to employ cross-polarization methods to transfer polarization from laser-polarized xenon to spins on the surfaces of materials, thereby selectively enhancing the NMR of surfaces (a prediction that was soon realized, as discussed later in this section).

This work was soon followed by numerous studies using ^{129}Xe OPNMR to probe the properties of various materials surfaces. In

one early study, the adsorbed xenon itself was the material being investigated. In this work, thin films of frozen xenon (~1-μm thickness, ≈2000 atomic layers) were prepared on the interior surfaces of glass containers of varying shape (*165*). The highly uniform xenon films gave rise to a variety of observed lineshapes that depended on the geometry and temperature of the glass cells; the origin of the lineshape dependence was the bulk diamagnetic susceptibility of solid xenon, giving signals that corresponded to model CSA lineshapes.

In another study, the interaction between adsorbed laser-polarized xenon and a polymer surface was investigated (*166*). In these experiments, laser-polarized xenon was adsorbed onto particles of powdered amorphous poly(acrylic acid) of moderate surface area (~15 m^2/g) at different temperatures. The xenon was observed to strongly interact with the polymer surfaces, which the authors suggest possibly resulted from the polar carboxylic acid functional groups present at the particle surfaces. The temperature dependence of the surface interaction, as measured by the ^{129}Xe chemical shift of the xenon resonance, fit well to a simple model of chemical exchange between gaseous and adsorbed xenon. Moreover, the pressure dependence of the xenon chemical shift permitted the diffusion constant of the surface-adsorbed xenon to be estimated (~3.3×10^{-5} cm^2/s).

^{129}Xe OPNMR was then utilized to probe the surfaces of CdS nanocrystals (*96*). Specifically, laser-polarized xenon was used to probe the morphology of the thiophenol capping groups on the nanocrystals. One interesting result from this work was the observation of two partially superimposed lines for xenon adsorbed onto CdS nanocrystals with low thiophenol coverage, which was interpreted as evidence for two distinct surface domains of the thiophenol groups on such nanocrystals. It was concluded that such domains were likely formed by the aggregation of thiophenol molecules on the surfaces under conditions of incomplete coverage, a hypothesis consistent with previous results of studies using X-ray photoelectron spectroscopy and liquid-state ^{1}H NMR.

C. Polarization Transfer to Surfaces

1. Cross-Polarization and Zero-Field Mixing

As described in Section IV, polarization transfer from laser-polarized xenon to other nuclei was first achieved in the solid phase with low-field thermal mixing (*38, 96, 97*). This technique involves adiabatically sweeping the external magnetic field through a regime where the difference between the Zeeman energies of the two spin baths is matched by their dipolar coupling. Following experiments where ^{129}Xe polarization was transferred to neighboring ^{131}Xe spins in xenon ice (*38*) and ^{13}C spins in a frozen CO_2/xenon matrix (*96*), zero-field mixing was used to transfer polarization to protons of a silicone surface coating (SurfaSil) on glass (*97*). A lower limit for the achieved value of the ^{1}H polarization P was estimated at 0.01, corresponding to an enhancement factor of ~300 for protons at 400 MHz.

Polarization has also been successfully transferred to material surfaces by Rf-driven Hartmann–Hahn cross-polarization (*98–100*) in the rotating frame through dipolar couplings at high field (*101, 102*). In one experiment, the immobilization of laser-polarized xenon at 90 K onto a high surface-area (835 m^2/g) sample of poly(triaryl-carbinol) permitted the ^{1}H NMR signal of the polymer surface to be enhanced by a factor of about 800 at 4.2 T (*104*).

In order to employ either zero-field mixing or Hartmann–Hahn CP to enhance the NMR signals of surface spins, it is required that either (a) the nuclei to be polarized have been embedded in a laser-polarized xenon ice matrix (*38, 96*) or (b) the laser-polarized xenon has been immobilized onto the material's surface (*97, 101, 102*). However, both of these preparations can be difficult to achieve in practice and are usually limited to temperatures below ~100 K.

2. SPINOE Enhancement of Surfaces

Following the successful solution-phase results obtained from laser-polarized xenon dissolved in liquid benzene (*103*), it was demonstrated that the nuclear spin polarization of both laser-polarized xenon and helium could be selectively transferred to nuclear spins on solid surfaces in high field (4.2 T) via the SPINOE (*167*). In contrast to the previous cross-polarization experiments, the magnetization transfer was established by dipole–dipole cross-relaxation between surface spins and mobile polarized gas atoms adsorbed on the surface, in a manner similar to that in the liquid-state NMR experiments described previously. It should be remembered that cross-relaxation is a far more inefficient means of transferring polarization than direct cross-polarization. However, while the overall signal enhancements observed with the SPINOE are smaller than those obtained via cross-polarization and zero-field mixing, surface selectivity can still be achieved with easier sample preparation over a wide range of experimental conditions, without the need for strong RF fields or field cycling procedures.

Figure 20 shows the evolution of the ^{1}H magnetization of surface –OH groups on particles of Aerosil130 after exposure to laser-polarized ^{129}Xe. Each point in the plot corresponds to the integral of the Fourier-transformed free induction decay, proportional to the instantaneous total nuclear magnetization. The inset shows the corresponding ^{1}H spectrum at the Boltzmann equilibrium (top spectrum) and after negatively polarized xenon has caused an enhancement of the surface magnetization (bottom spectrum); the enhanced spectrum is shown for the time t_0 when the negative enhancement has reached a maximum. A maximum enhancement factor of −20 was observed for the ^{1}H magnetization. In this type of experiment, the magnitude of the SPINOE depends on the cross-relaxation rate (σ_{HXe}) and on the number of noble gas spins on the surface, which can depend on the sample temperature. SPINOE enhancements using adsorbed ^{129}Xe were measured between about 100 and 200 K, with the greatest enhancement obtained at 130 K.

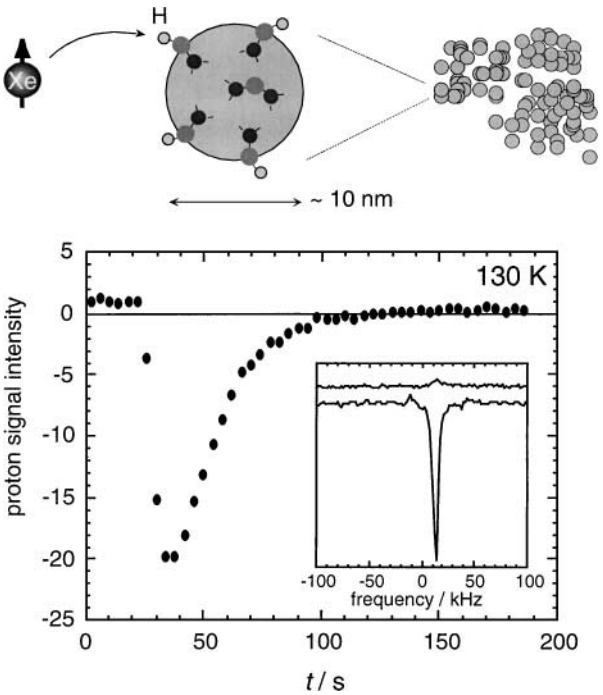

FIG. 20. Time evolution for the SPINOE enhancement of the integrated ^{1}H NMR signal from surface –OH groups on Aerosil 130 particles following adsorption of negatively laser-polarized ^{129}Xe (*167*). Signals taken prior to xenon absorption are shown for comparison. The largest enhancement factor observed was −20. The inset shows a thermal equilibrium ^{1}H NMR spectrum (top) and the corresponding spectrum obtained when the negative enhancement had reached its maximum (bottom). Figure courtesy of Roberto Seydoux.

Experiments were also performed that demonstrated SPINOE polarization transfer from both laser-polarized xenon and helium to a polymer coating (polyethylene oxide (PEO), with an average molecular mass of ≈400,000) on Aerosil130 particles. The adsorption of laser-polarized xenon at 130 K permitted a fractional SPINOE enhancement of the PEO ^{1}H NMR signal of about 10, with an estimated value for $\sigma_{\mathrm{H\,Xe}}$ of 7×10^{-4} s^{-1}. However, this value is about an order of magnitude lower than that expected based on the estimated number of adsorbed xenon spins (and other relevant experimental parameters). Possible origins of this disparity may have included the presence of other relaxation pathways (i.e., other than xenon-proton dipole–dipole interactions) such as paramagnetic centers and ^{129}Xe CSA, as well as the likelihood that not all of the protons were accessible to the adsorbed noble gas spins (this latter effect would make the cross-relaxation rate seem smaller than it actually is). By using laser-polarized ^{3}He, signal enhancements between 100% and 200% could be observed for protons of PEO coating the Aerosil surfaces at sample temperatures between 4 and 10 K. The helium–proton cross-relaxation rate, $\sigma_{\mathrm{H\,He}}$, was estimated to be $\sim 1 \times 10^{-3}$ s^{-1}. Finally, the ability to enhance ^{13}C NMR signals via the SPINOE was demonstrated following the adsorption of laser-polarized xenon onto ^{13}C-labeled CO_2 coating Aerosil300 particles. An enhancement factor of −4 was observed for the ^{13}C spins, with an estimated xenon–carbon cross-relaxation rate $\sigma_{\mathrm{C\,Xe}} \approx 4 \times 10^{-4}$ s^{-1}.

More recently, it was shown that silicon nuclei could be polarized indirectly via the SPINOE by a technique called SPINOE-CP (*168*), despite the low accessibility of these spins to the adsorbed xenon. By adsorbing laser-polarized xenon onto the surfaces of Aerosil300 particles, the polarization of surface protons could be enhanced via the SPINOE; this enhanced polarization could then be rapidly transferred by conventional Hartmann–Hahn cross-polarization methods to neighboring ^{29}Si spins in the material's lattice. Fractional enhancements of 4 to 5 for the ^{29}Si NMR signal could be obtained with this technique.

D. Enhancing NMR with Continuous Xenon Flow

By adapting the design of an optical pumping apparatus capable of producing a continuous stream of laser-polarized xenon gas (*47*), a constant supply of laser-polarized xenon can be delivered to a sample within an NMR magnet (*48, 49, 160, 170*). With this apparatus, ^{129}Xe NMR experiments are not limited in time by longitudinal ^{129}Xe relaxation. Moreover, pulse sequences requiring a steadily renewed nuclear spin polarization can be applied without any restriction, permitting phase cycling, signal averaging, and a variety of multidimensional NMR experiments (and MRI experiments, as discussed in the next section).

For example, the continuous delivery of fresh laser-polarized xenon gas permitted the direct observation of xenon exchange between two different zeolites within a powdered sample via two-dimensional exchange spectroscopy (EXSY) (*32*). A 2D ^{129}Xe EXSY spectrum of laser-polarized xenon exchanging between particles of zeolites Y and ZSM-11 taken at 220 K is shown in Fig. 21. This experiment was performed with a xenon

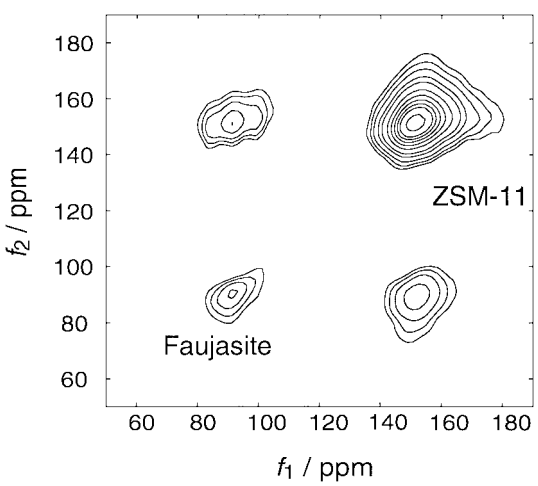

FIG. 21. Contour plot of a 2D ^{129}Xe EXSY spectrum of laser-polarized xenon adsorbed on a mixture of highly siliceous zeolites Y (Faujasite) and ZSM-11, taken at 220 K with a xenon partial pressure of 1.3 KPa. The existence of cross peaks shows that significant xenon exchange occurs between the two zeolites during the mixing time of 25 ms. Figure courtesy of Eike Brunner.

partial pressure of only 1.3 kPa. The 2D spectrum shown was obtained with an exchange mixing time of 25 ms. The diagonal peaks at 91 and 150 ppm correspond to xenon residing in zeolite Y and zeolite ZSM-11, respectively. The existence of cross peaks in the EXSY spectrum is indicative of significant xenon exchange between the two sites within the given exchange period. By analyzing the dependence of the cross-peak signal intensities upon the mixing time, a mean exchange time of 15 ± 5 ms could be determined.

Recently, ^{129}Xe OPNMR was used to study the behavior of xenon in a polycrystalline sample with 5-Å channels under conditions of continuous xenon flow (*171*). This subnanoporous material is comprosed of tris(*o*-phenylenedioxi)-cyclo-phosphazene (TPP) in such a way that the 5-Å channels are formed with nearly perfect cylindrical symmetry, leading to an effectively one-dimensional gas phase for xenon within the material. The use of continuous flow of laser-polarized xenon afforded enormous ^{129}Xe NMR sensitivity, allowing numerous experiments to be rapidly and systematically performed under varying conditions of temperature and xenon partial pressure within the flowing gas mixture.

When a gas mixture comprised entirely of laser-polarized xenon was flowed through the TPP material, it was observed that the CSA of the ^{129}Xe signal varied with temperature in such a way that *full inversion* of the anisotropy could be achieved over the available temperature range, as shown in Fig. 22a. For example, at 373 K, the observed ^{129}Xe lineshape is indicative of a nearly axially symmetric CSA with positive anisotropy. However, decreasing the temperature results in an isotropic line at 333 K, and the sign of the anisotropy becomes inverted by 263 K. The authors note that while such CSA inversions have been observed previously (*172, 173*), the behavior in the present case is unique because the nearly perfectly axial CSA and the collapse to the isotropic line at 333 K suggest that only two opposing mechanisms exist that govern the distortion of the xenon electron cloud from spherical symmetry. Namely, the authors suggest the two mechanisms to be: (1) interactions between xenon atoms and the near-cylindrically symmetric walls of the channels; and (2) collisions between xenon atoms and other gas-phase species (e.g., other xenon atoms). Indeed, varying the xenon concentration within the flowing gas mixture from 1 to 100% at constant (ambient) temperature produced a similar inversion of the axially symmetric CSA, as shown in Fig. 22b. The authors suggest that because such results can be described by simply considering the competing influences of gas–gas and gas–wall interactions, the xenon/TPP system constitutes an ideal system with which to study physisorption and diffusion of gases within nanoporous materials.

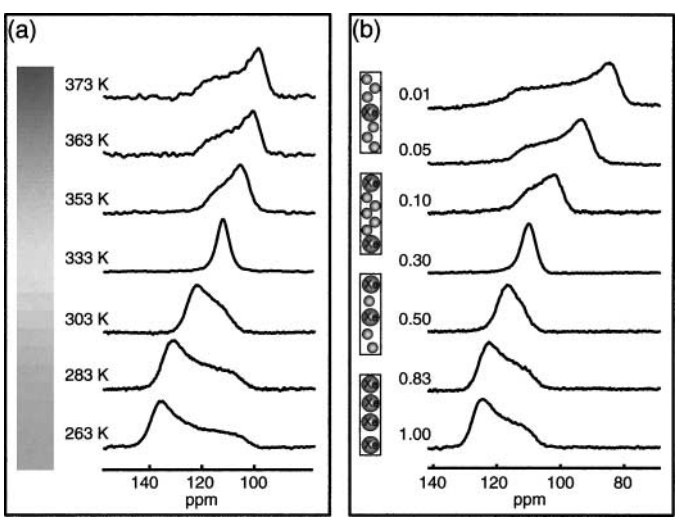

FIG. 22. Inversion of ^{129}Xe CSA of laser-polarized xenon gas flowing through subnanometer channels of TPP. (a) Temperature dependence of ^{129}Xe CSA with gas mixture comprised entirely of laser-polarized xenon. (b) Xenon partial pressure dependence of ^{129}Xe CSA at ambient temperature. Figures courtesy of Roberto Simonutti and John Logan.

Other experiments have recently been performed that take advantage of continuous xenon flow to perform novel polarization transfer experiments. SPINOE polarization transfer to surfaces does not require immobilization of the laser-polarized noble gas. Thus, not only can surface-selective SPINOE experiments be performed over a broader range of temperatures, but they can be carried out indefinitely under conditions of continuous flow. In one demonstration, laser-polarized xenon was streamed continuously over an Aerosil surface to selectively enhance the surface proton spins via the SPINOE (*48*). Following delivery of laser-polarized xenon to the sample, the gas was recirculated with a mechanical pump back into the optical pumping cell for re-polarization, permitting the experiment to be performed without interruption for several hours. With this technique, a steady-state enhancement of 200% was achieved (~800% when isotopically enriched ^{129}Xe was used), with a steady-state ^{129}Xe polarization of only ~0.25% at the sample.

E. SPINOE under Magic-Angle Spinning

Considerable work at Purdue and Berkeley has been directed toward the development and application of an experimental apparatus capable of delivering a continuous stream of laser-polarized xenon to the sample, while performing magic-angle spinning (MAS) of the sample in order to obtain enhanced, high-resolution surface NMR spectra (*169, 174–176*). This technique has been denoted by Raftery and co-workers as OPMAS.

One such OPMAS apparatus used at Berkeley is shown schematically in Fig. 23a. The first portion of the apparatus is identical to that used to perform the previous continuous-flow experiments under static sample conditions (*48*), adapted from the original design of Driehuys *et al.* (*47*). As described previously for the continuous-flow apparatus shown in Fig. 5, a high-pressure (~800 kPa) gas mixture of xenon, nitrogen, and helium streams from a gas cylinder through a heated pumping cell (~400 K) containing a small amount of rubidium metal, where the Rb atoms are optically pumped at the wavelength of the Rb

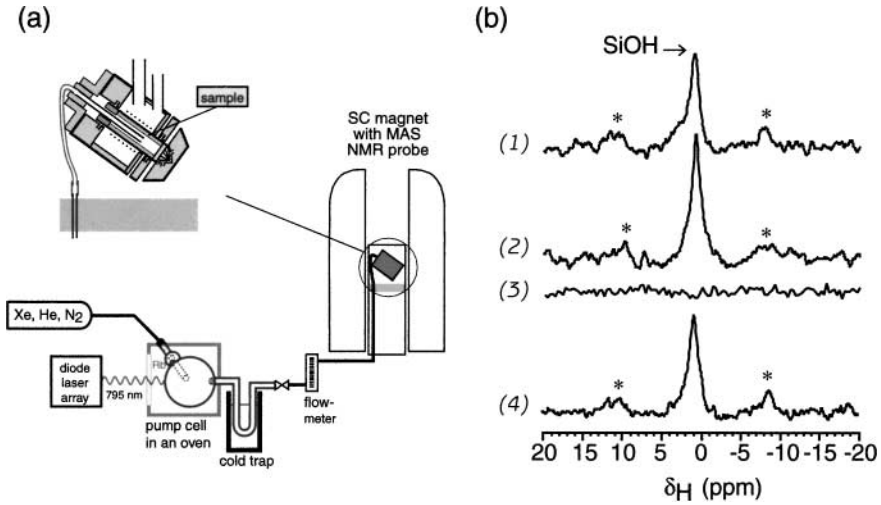

FIG. 23. (a) Schematic of an apparatus used for OPMAS experiments (*174*); see text for description. (b) SPINOE-MAS ^{1}H difference NMR spectra taken from surface –OH groups on Aerosil300 particles at 173 K (1), 168 K (2, 3), and 163 K (4) (*174*). Spectrum (3) was obtained under the same conditions as (2), but with thermally polarized xenon (obtained by turning the optical pumping laser off), demonstrating that the signals shown originate entirely from cross-relaxation with laser-polarized xenon. The asterisks (∗) denote spinning sidebands. Each spectrum was taken as the sum of four scans, with a repetition time of 10 s. Figures courtesy of Eike Brunner.

D_1 transition with circularly polarized light produced by a high-power ($\geq$100 W) diode laser array. After passing through the pumping cell, the gas is expanded to normal pressure and finally directed into a homebuilt double-resonance probe equipped with a commercial variable-temperature MAS unit (Fig. 23a inset).

OPMAS was first demonstrated at Purdue in experiments designed to obtain SPINOE enhancement of surface protons with high resolution under conditions of continuous polarized xenon flow (*169*). In these experiments, the ^{1}H NMR signal from water adsorbed onto fumed silica particles (surface area, 420 m^2/g) was enhanced via the SPINOE at 150 K while spinning the sample at ~3000 Hz. The SPINOE provided a two-fold increase in ^{1}H NMR signal compared with the thermal equilibrium signal; the cross-relaxation rate σ_{HXe} was measured to be $\sim 2 \times 10^{-3}$ s^{-1}.

These experiments were soon followed by work performed at Berkeley in which the OPMAS apparatus shown in Fig. 23a was used to obtain high-resolution SPINOE spectra of surface protons of Aerosil300 SiO_2 particles under conditions of continuous xenon flow (*174*). Figure 23b shows variable-temperature ^{1}H "SPINOE-MAS" spectra from the Aerosil sample acquired at a resonance frequency of 301.2 MHz and with a sample spinning rate of about 3 kHz; these spectra were obtained by subtracting the signal obtained when the sample was at thermal equilibrium (laser off) from the signal obtained when the xenon was laser-polarized (laser on). The highest SPINOE signal intensity—about 140% of the equilibrium signal—was observed at ≈168 K. The efficiency of the spin-polarization transfer strongly decreased with increasing temperature (most likely due to increasingly inefficient xenon adsorption), in agreement with previous observations (*167*). One striking feature of the spectra in Fig. 23b is the spinning sidebands, denoted by asterisks (∗); as expected, these sidebands are each offset from the main ^{1}H Aerosil resonance by the spinning frequency of the MAS rotor.

The above examples demonstrate the ability to observe SPINOE enhancement of proton NMR signals under MAS conditions. However, the surface area of the fumed silica and Aerosil particles used in such studies is high (e.g., 300 m^2/g for Aerosil300). Moreover, enhancing the NMR signals of nuclei other than protons would be advantageous for a number of reasons, including (1) wider chemical shift ranges, giving more sensitivity to local structure in a material; and (2) improved spectral resolution, resulting from reduced line broadening from weaker homonuclear dipolar coupling. In more recent studies, the ability to perform high-resolution SPINOE polarization transfer experiments to other types of nuclei, and on materials with much smaller surface areas, was demonstrated.

In one report, ^{129}Xe–^{13}C SPINOE-MAS experiments were performed on microcrystallites of fullerenes (C_{60} and C_{70}) (*175*). Fullerenes are attractive systems to study with such methods because their spin relaxation behavior is well-characterized (*177–180*), and the ^{13}C longitudinal relaxation times can be relatively long at low temperatures (e.g., ^{13}C $T_1 \sim 80$ s for C_{60} (*178*)). However, because the average diameter of the crystallites was large (~4 μm for the C_{60} sample and ~2 μm C_{70}), the respective surface areas of these samples were estimated to be only ~1 and ~2 m^2/g.

Figure 24a shows ^{13}C MAS NMR spectra of C_{60} obtained under different conditions. The equilibrium ^{13}C MAS NMR spectrum of C_{60}, denoted Fig. 24a(1), shows the characteristic single line of C_{60} at 144 ppm (*179*). The SPINOE spectrum shown in Fig. 24a(2) was obtained as the difference between the spectrum measured when laser-polarized ^{129}Xe was flowing through the rotor, and the spectrum measured when the xenon was

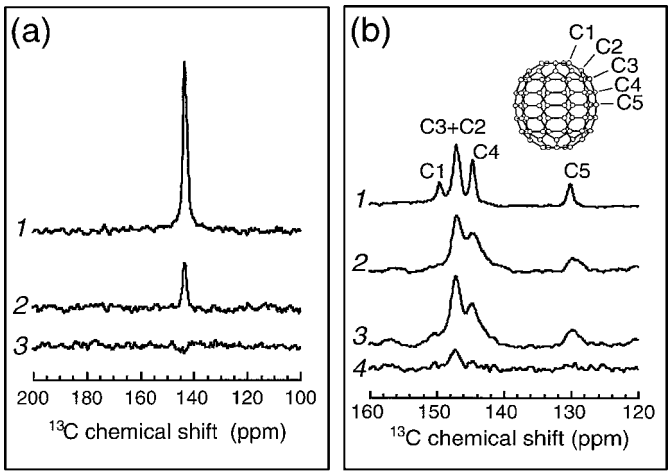

FIG. 24. ^{13}C MAS spectra obtained from (a) C_{60} and (b) C_{70} crystallites (*175*). (a) (1) ^{13}C MAS NMR spectrum obtained when the gas stream contained only thermally polarized xenon (laser off). (2) Difference SPINOE-MAS ^{13}C NMR spectrum obtained by subtracting Spectrum (1) from a spectrum obtained using laser-polarized xenon. (3) Difference spectrum obtained in the absence of laser-polarization. The observed overall enhancement factor in (2) was about 15%. (b) ^{13}C MAS spectra obtained from C_{70} crystallites at room temperature (1) and 150 K (2–4) (*175*). (1, 2) Spectra obtained in the absence of laser-polarization. (3) Spectrum obtained with flow of laser-polarized xenon. (4) The signal obtained from subtracting (2) from (3), showing the differential enhancement of the C2 + C3 resonance. Figures courtesy of Eike Brunner.

thermally polarized. The intensity of the SPINOE signal corresponds to ∼15% of the intensity of the spectrum shown in Fig. 24a(1). However, because only a very small fraction of the C_{60} molecules is located on the surface of the crystallites (∼0.0015, estimated from the mean crystallite diameter and the diameter of a C_{60} molecule (∼1 nm)), the actual enhancement of the ^{13}C spins directly (or indirectly) coupled to the laser-polarized xenon was significantly larger. Assuming that the SPINOE polarization transfer occurs only to C_{60} molecules located at crystallite surfaces, one can conclude that the observed signal enhancement of ∼15% would correspond to a polarization enhancement factor of about 100. However, this estimate neglects ^{13}C spin diffusion, which can transport spin polarization into the bulk of the crystallites, resulting in a lower effective magnetization enhancement for the spins. Ideally, such spin diffusion is quenched under fast-MAS conditions (when the sample-spinning rate is greater than the homonuclear linewidth), although the degree of residual spin diffusion was difficult to determine. Nevertheless, by assuming full spin diffusion (i.e., the spin diffusion observed in a static sample), an upper limit for the penetration depth of 30–40 nm could be estimated, resulting in a lower limit for the SPINOE enhancement factor of ∼3.

Figures 24b(1) and 24b(2) show the ^{13}C MAS NMR spectra of C_{70} crystallites measured at room temperature and 150 K, respectively, with assignments as given in Ref. (*179*). Because the residual linewidths of the ^{13}C MAS spectra increase with decreasing temperature (*179*), the signal resulting from C1 carbons is poorly resolved at 150 K. While the spectrum in Fig. 24b(2) was measured in the presence of a gas stream carrying thermally polarized xenon (i.e., with the laser turned off), the spectrum in Fig. 24b(3) was obtained while the laser was on, producing differential enhancements in the ^{13}C spectra. Specifically, Fig. 24b(3) shows an increase in intensity of the signal resulting from carbons in the C2 and C3 positions (147 ppm) of about 25%, more clearly shown in the difference spectrum (Fig. 24b(4)). However, in agreement with the results of previous calculations and measurements (*179*), identical ^{13}C T_1 values of ≈5 s were measured for the C2, C3, C4, and C5 carbons at 150 K. Therefore, it is likely that the greater SPINOE for the C2/C3 resonance results from a higher cross-relaxation rate. The origin of this selectivity is unknown, but may be due to greater xenon accessibility to C2 and/or C3 carbons in the C_{70} crystallites, or a higher heat of adsorption of xenon for these sites.

In a second study, both the SPINOE and SPINOE-CP were used to enhance the NMR signals of ^{13}C and ^{29}Si spins on the surfaces of fumed silica particles under OPMAS conditions (*176*). In a manner similar to that of Ref. (*168*), signal enhancement of ^{29}Si spins of the fumed silica particles (surface area, 389 m^2/g) was achieved by first permitting SPINOE polarization transfer from adsorbed laser-polarized xenon to surface protons, and then coherently driving polarization from these surface protons to neighboring ^{29}Si spins via Hartmann–Hahn CP. The observed ^{29}Si NMR signal was enhanced by about 16%. For ^{13}C spins of ^{13}C-labeled methanol chemisorbed onto the fumed silica surfaces, however, it was observed that the SPINOE was more efficient than SPINOE-CP (30% vs 7.6% enhancement). The authors point out, however, that the observed enhancement of the carbon signal may have been affected by cross-relaxation with protons, instead of a purely direct SPINOE between the xenon and carbon spins.

More recent work by the Purdue group has examined this effectively three-spin system in greater detail, obtaining measurements of the relevant ^{1}H–^{13}C, ^{13}C–^{129}Xe, and ^{1}H–^{129}Xe cross-relaxation rates (0.088, 3.8×10^{-4}, and 8.6×10^{-4} s^{-1}, respectively) (*181*). These experiments indicated that the observed ^{13}C polarization was indeed dependent upon cross-relaxation with both xenon and protons; for example, saturation of the ^{1}H spins during ^{13}C SPINOE build-up gave an enhancement factor of 3.3 for the carbon signal, resulting from the summed effects of the ^{1}H–^{13}C NOE and ^{129}Xe–^{13}C SPINOE, while an enhancement factor of 1.6 was measured when the xenon was unpolarized. Deuteration of the adsorbed methanol—effectively quenching the cross-relaxation between the carbon and hydrogen spins—permitted a 12-fold enhancement of the carbon signal (at ≈4.7 T, −126°C).

VII. ENHANCED IMAGING OF MATERIALS

A. Introduction

The nondestructive characterization and imaging of porous materials continues to be an experimental challenge. For example, the properties of many porous materials can depend not

only on the overall porosity, but also on the size distribution and connectivity of the pores within a given material. Such parameters can be difficult to study—particularly in opaque systems—without destroying the material in question. While in principle such materials can be studied by infusing them with water, mercury, or other liquids (often at high pressure), there are various samples whose chemical or physical sensitivity precludes such approaches, including many polymers, catalysts, ceramics, aerogels, food products, and antiquated or fossilized remains (the study of living samples is the subject of the next section).

As inert gases, xenon and helium can provide contrast for studies of material inhomogeneity and sample morphology in a nondestructive fashion. Some work has been performed using gaseous (thermally polarized) ^{129}Xe to image various materials samples (see, for example, Ref. (*182*)). However, a serious limitation of the MRI of gases is the low density in the gas phase compared to that of condensed-phase media (e.g., liquid water), as well as the normally low equilibrium nuclear spin polarization. Luckily, the enormous signal enhancement afforded by optical pumping can overcome the low spin density of gas-phase media, thereby permitting, for example, the imaging of macroscopic void spaces in porous materials, the visualization of convective behavior and phase exchange, studies of the effects of boundary-restricted diffusion on MRI, and the visualization of gas flow and diffusion in porous materials under conditions of continuously recirculating xenon flow.

B. Gas Imaging under Static Conditions

Following the use of laser-polarized xenon gas to image the void spaces in excised rat and guinea pig lungs (*183, 184*) (discussed in greater detail in the next section), laser-polarized xenon gas was used to demonstrate void space imaging in materials, without the need for signal averaging (*185*). Figure 25 shows enhanced ^{129}Xe MR images obtained following the admission of laser-polarized xenon gas into structured phantom samples. Specifically, the left side of Fig. 25 shows a FLASH ^{129}Xe MR image of xenon gas in a phantom in which void spaces have been cut to give the chemical symbol for xenon ("Xe"), while the right side of Fig. 25 shows a FLASH ^{129}Xe MR image of xenon gas in a phantom comprised of three nested glass tubes; the gaps between the tubes varied from 0 to 2 mm. It was possible to obtain ^{129}Xe MR images with a resolution of $\sim$100 μm, on the order of the diffusion-limited resolution for gaseous xenon when using typical micro-imaging gradients. The ability to directly image xenon penetration within an aerogel sample as a function of time was also demonstrated in this work.

C. Enhanced Imaging in Condensed Phases: Visualization of Convection and Phase Exchange

The enormous sensitivity enhancement provided by optical pumping, along with the long spin–lattice relaxation time of ^{129}Xe in benzene, permitted the dissolution and macroscopic

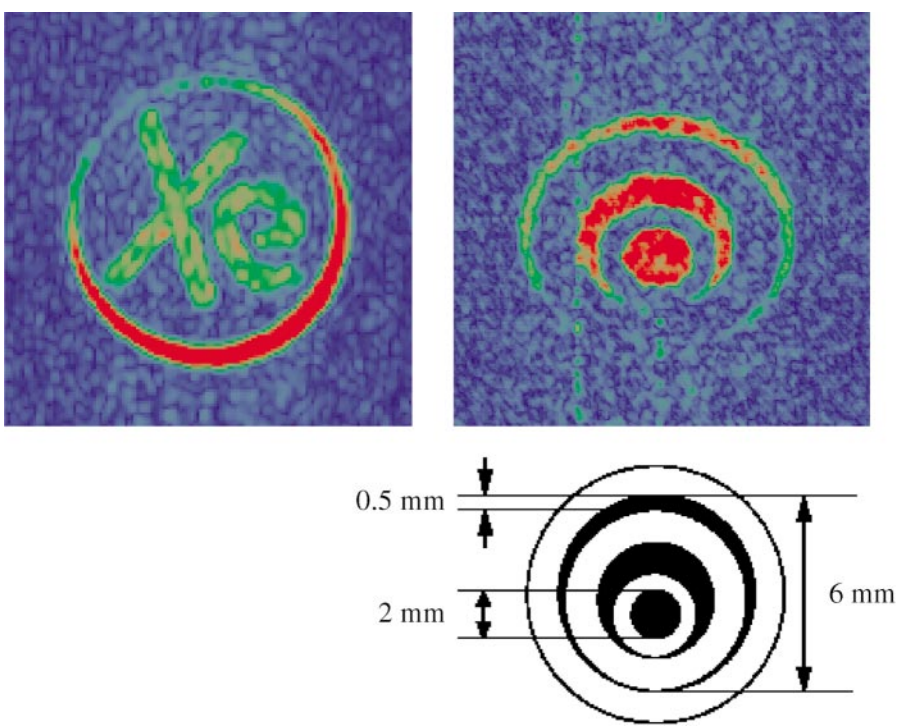

FIG. 25. (Color) Two-dimensional images of laser-polarized xenon in phantom samples. (Left) Image obtained following the admission of laser-polarized xenon in a phantom sample (cross-sectional diameter, $\sim$7 mm) in which void spaces have been cut to give the chemical symbol for xenon ("Xe"). (Right) Image obtained following the admission of laser-polarized xenon in a phantom comprised of three nested glass tubes, with geometry as shown in the diagram (*185*). Figures courtesy of Yi-Qiao Song.

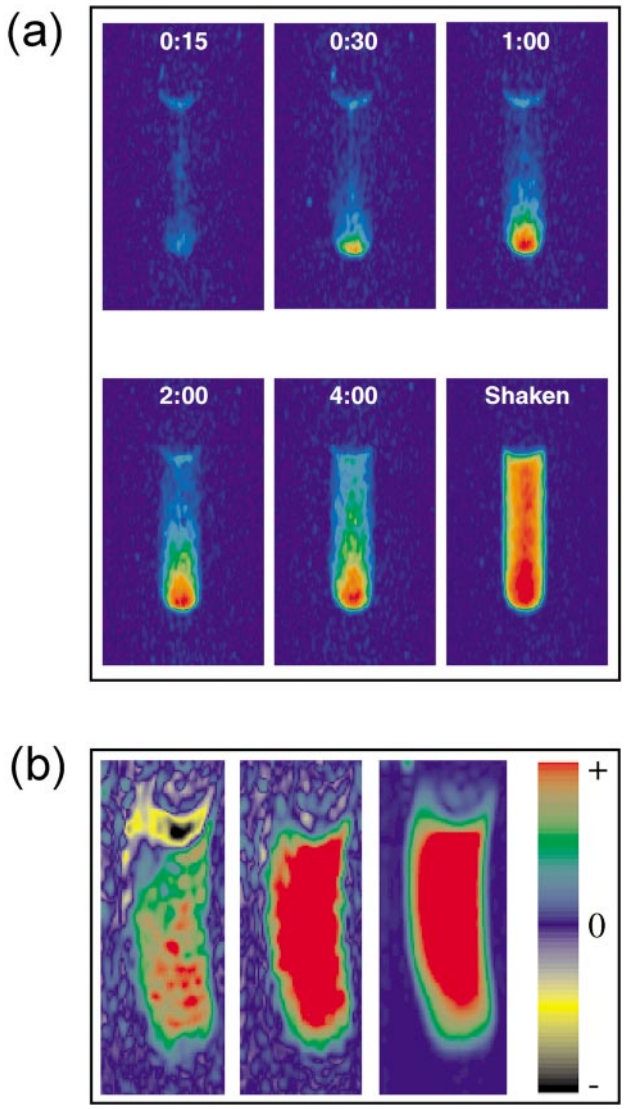

FIG. 26. (Color) Time-dependent OPMRI of laser-polarized xenon dissolving in benzene (*103*). The vertical axis of the images is parallel to the external magnetic field and the long axis of the NMR sample tube. (a) Time-resolved false-color 2D FLASH ^{129}Xe MR images of the dissolved xenon in a sample tube containing partially deuterated benzene taken immediately following exposure to gaseous laser-polarized xenon. (b) The 2D false-color ^{1}H SPINOE MRI of fully protonated benzene taken 2 min (left image) and 6 min (middle image). Following the introduction of laser-polarized xenon; an equilibrium ^{1}H MR image is also shown (right image). The negative region in the left image (yellow/black region) originates from the expansion of the liquid phase of benzene following the dissolution of xenon. The images were obtained by the EPI method. The distortion of the images reportedly originated from inhomogeneity in the static magnetic field. Figures courtesy of Yi-Qiao Song.

transport of xenon in benzene to be observed in detail via OPMRI (*103*). Figure 26a shows a series of 2D FLASH ^{129}Xe OPMR images taken as a function of time immediately following the exposure of partially deuterated benzene to gaseous laser-polarized xenon. A macroscopic xenon concentration gradient is observed to rapidly form in the tube at short times; this concentration gradient is then observed to become more equilibrated over time by the 4:00 mark. The final image shows an equilibrium distribution of xenon obtained by vigorously shaking the sample. Interestingly, the concentration at early times is observed to be greatest at the *bottom* of the tube. This xenon accumulation at the bottom of the sample likely originates from density differences between the xenon/benzene solution and neat benzene; the heavier, xenon-rich regions that form at the top of the solution following xenon diffusion into the solvent gravitate to the lower regions of the tube via convection.

The dissolution of laser-polarized xenon also permitted the SPINOE enhancement of the benzene proton polarization to be directly imaged. Figure 26b shows two 2D ^{1}H "SPINOE MR images" taken at 2 and 6 min following exposure of a fully protonated benzene sample to laser-polarized xenon gas, alongside a third proton MR image obtained with the benzene protons at thermal equilibrium. The SPINOE images were obtained by subtracting the equilibrium image from the data obtained following xenon dissolution; the maximum enhancement in the first image was 5%, while the maximum enhancement in the second image was 12% (the contrast for the SPINOE images was multiplied by a factor of 8). Note that the concentration gradient seen previously in Fig. 26a is also observed in the 2-min SPINOE image (left). This effect is expected, as the SPINOE enhancement of the proton magnetization will normally scale with the local xenon concentration in the absence of strong xenon binding. The uniform appearance of the SPINOE image taken at 6 min, however, suggests that the xenon concentration had equilibrated throughout the benzene sample by the time that the image was acquired.

Following work demonstrating the potential for enhanced sensitivity and MRI resolution from the imaging of frozen laser-polarized xenon at 77 K (*186*), MRI studies of liquid laser-polarized xenon were performed by the Harvard–Smithsonian/MIT collaboration (*123*). By condensing the xenon, the spin density is increased by orders of magnitude, thereby improving the potential maximum resolution. However, in this more recent work, the presence of both liquid and gas phases of xenon within the tube, in addition to the bright NMR signal and long xenon spin–lattice relaxation times, permitted the direct observation xenon exchanging between the phases at 166 K.

Figure 27 contains a series of 2D FLASH ^{129}Xe MR images taken of laser-polarized xenon condensed in a Pyrex tube at various stages of exchange. Specifically, Fig. 27a shows an image of the liquid xenon that has collected at the bottom of the tube, while Fig. 27b shows the corresponding gas image; Figs. 27c–27f) show xenon evaporation as a function of time, while Figs. 27g–27j show the corresponding images of xenon condensation into the liquid phase. The propagation of laser-polarized xenon in the vapor phase (shown in Figs. 27c–27f) is consistent with the xenon gas diffusion coefficient under the given experimental conditions (about 0.02 cm^2/s). In principle, the authors state, liquid laser-polarized xenon MRI could achieve a resolution on the order of 10 μm^3 at 166 K (with gradient strengths on the

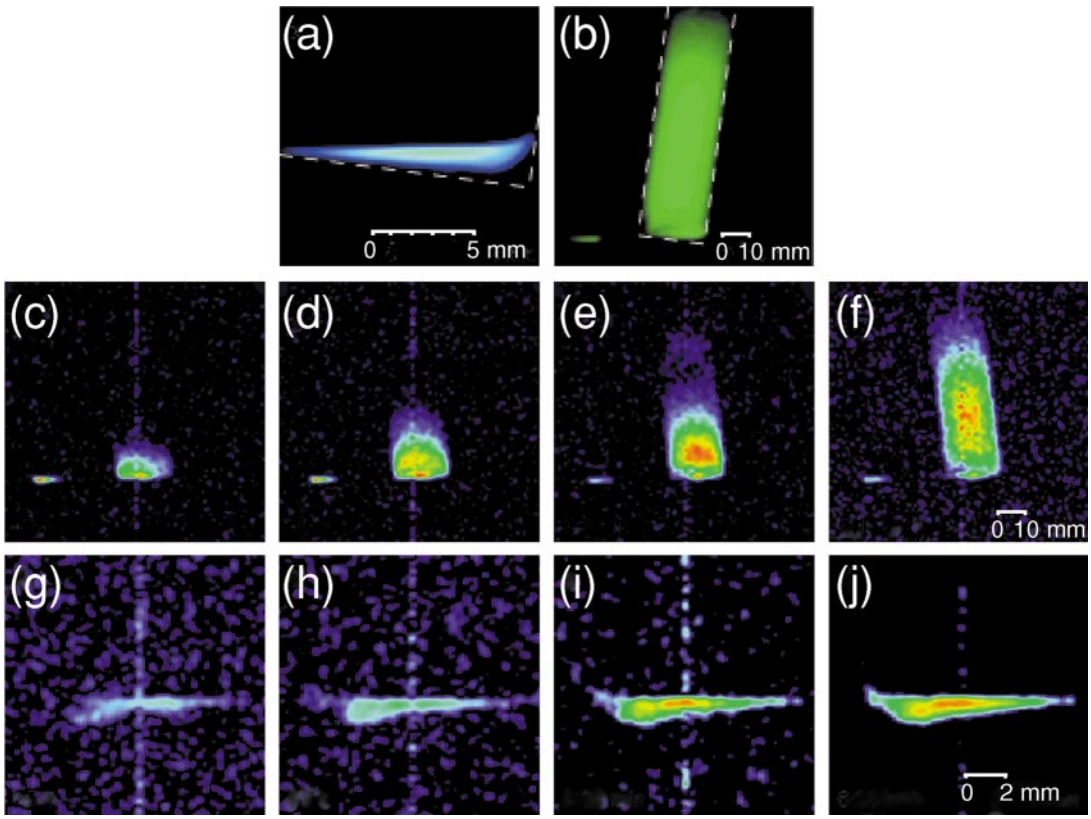

FIG. 27. ^{129}Xe FLASH MRI of laser-polarized xenon condensed in a tilted glass tube at 166 K (*123*). (Color) (a) MR image of liquid laser polarized xenon that has condensed at the bottom of the tube. The image resolution was $195 \times 195\ \mu m^2$, limited by the strength of the applied magnetic field gradients. A displaced liquid xenon signal can also be seen in the xenon gas image in (b) resulting from RF-excited xenon atoms in the gas phase condensing into the liquid phase prior to acquisition. (c–f) Time-resolved MR images tracking the evaporation of liquid laser-polarized xenon, taken 12 s (c), 46 s (d), 3:30 min (e), and 5:15 min (f) after the xenon gas signal was destroyed by the application of multiple selective RF pulses and gradient pulses. (g–j) Time-resolved MR images tracking the condensation of gaseous laser-polarized xenon, taken 25 s (g), 63 s (h), 2:30 min (i), and 6:30 min (j) after the xenon liquid signal was destroyed by the application of multiple selective RF pulses and gradient pulses. Figures courtesy of Glenn Wong and Ronald Walsworth.

order of 400 G/cm). The authors suggest many possible applications of liquid laser-polarized xenon MRI, including studies of density equilibration and convective flow near xenon's critical point and the imaging of microstructure in porous media.

The Harvard–Smithsonian/MIT collaboration recently extended this work by performing two-dimensional NMR velocity imaging of laser-polarized xenon gas above a droplet of condensed liquid xenon (*187*). The authors exploited the high signal endowed by laser-polarization in order to perform more rapid imaging than one can normally achieve with thermally polarized gas/liquid samples, thereby permitting the direct observation and study of the convection of gas-phase xenon atoms evaporating from liquid laser-polarized xenon in this closed two-phase system.

D. Effects of Diffusion on Imaging

In condensed phases, the one-dimensional resolution of MRI can reach a few microns under the most ideal of circumstances and is normally limited by the low signal obtained from the relatively low number of spins in such minute portions. However, one limitation on the resolution of laser-polarized gas imaging originates from the rapid diffusion of gases, typically several orders of magnitude higher than in liquids. For example, the 100-μm resolution of the image in Fig. 25b was primarily limited by the rapid diffusion of the polarized xenon gas, and not by the available signal.

In addition to limiting the MRI resolution, diffusion may distort the lineshape of MR images for samples containing boundaries or diffusion barriers within the space being imaged. This effect was first suggested by numerical simulations (*188, 189*) and was later explored experimentally (*190, 191*) using ^{1}H NMR of liquid samples. In one dimension, the diffusion problem has been solved analytically (*192–194*). However, the detailed characterization of such effects has been difficult using ^{1}H NMR. For example, given a value for the diffusion constant of water molecules $D_w \approx 2 \times 10^{-5}$ cm^2/s, the corresponding effects from diffusion would occur over a distance $d = \sqrt{2D_w t}$, or less than 10 μm during a time t of a typical one-dimensional (1-D) imaging experiment ($\sim$10 ms). An imaging resolution below 10 μm

is difficult to achieve because the signal from such a small region is often too weak.

The use of laser-polarized xenon gas for studying the effects of boundary restricted diffusion provides two advantages: a strong NMR signal and a large diffusion length. Given a xenon diffusion constant at 1 atm of 0.0565 cm^2/s (*60*), one obtains a value of $d = 0.034$ cm for $t = 10$ ms, which can be readily measured. The Princeton group (*195*) first used samples of polarized ^{3}He gas to study the the effects of diffusion on imaging, while demonstrating the ability to image such polarized gases at low field (a prospect discussed later in Section IX); those investigations were performed in the weak-diffusion regime, where the diffusion length is much smaller than the sample size.

In a more recent study, the effects of diffusion on MRI were examined in greater detail using 1D samples of laser-polarized xenon gas (*196*). In these experiments, the strength of the applied gradient and the geometric dimension of the 1D sample could be varied, permitting the systematic study of the evolution of diffusion-mediated image distortions between the regimes of strong and weak diffusion. By directly measuring the displacement distribution of the polarized xenon atoms, it was shown that in the weak-diffusion regime the image distortions originate from the restricted diffusive motion near the sample boundaries, in agreement with previous theoretical work. In these experiments, a thin, pyrex tube with a rectangular cross-section (0.66×0.07 cm) was loaded with $\sim$2 atm of laser-polarized xenon. Three pulse sequences were used in these experiments, all of which employed a soft, 500-μs Gaussian excitation pulse (tipping angle, $\leq 5^\circ$) applied during a slice-selection gradient along **z**. To obtain 1D images, a gradient pulse was applied perpendicularly to **z** along either the short or long cross-sectional dimension of the tube following the excitation pulse. The acquired free induction decay was then Fourier transformed to obtain the image. Xenon displacement distribution measurements were performed using the pulsed-field-gradient spin-echo method (see, for example, Ref. (*197*)). Finally, edge-enhanced imaging was demonstrated simply by varying the duration, τ_1, of the gradient applied perpendicularly to **z**. The signal was then acquired in echo mode during the application of a refocusing gradient pulse of opposite sign.

1. Imaging in the Limits of Strong and Weak Diffusion

To study how diffusion distorts MR images, two series of 1D images were taken as a function of the gradient G along both axes of the sample. Five images selected from these series are shown in Fig. 28a. These images display the evolution of the lineshape from a sharp resonance at zero gradient, to a slightly broadened but still single resonance in the limit of strong diffusion, to the development of two broad lines at an intermediate regime, to the limit of weak diffusion in the fifth image; the two broad features seen in the fourth image have grown into sharp, well-defined spikes in the fifth image—their locations correspond to positions near the sample boundaries (the so-called "edge-enhancement effect"). Edge spikes such as those manifested in the fifth image have been observed previously in polarized gas samples (*195, 198*); Saam *et al.* (*195*) used this effect to demonstrate edge enhancement in the images of polarized ^{3}He gas samples.

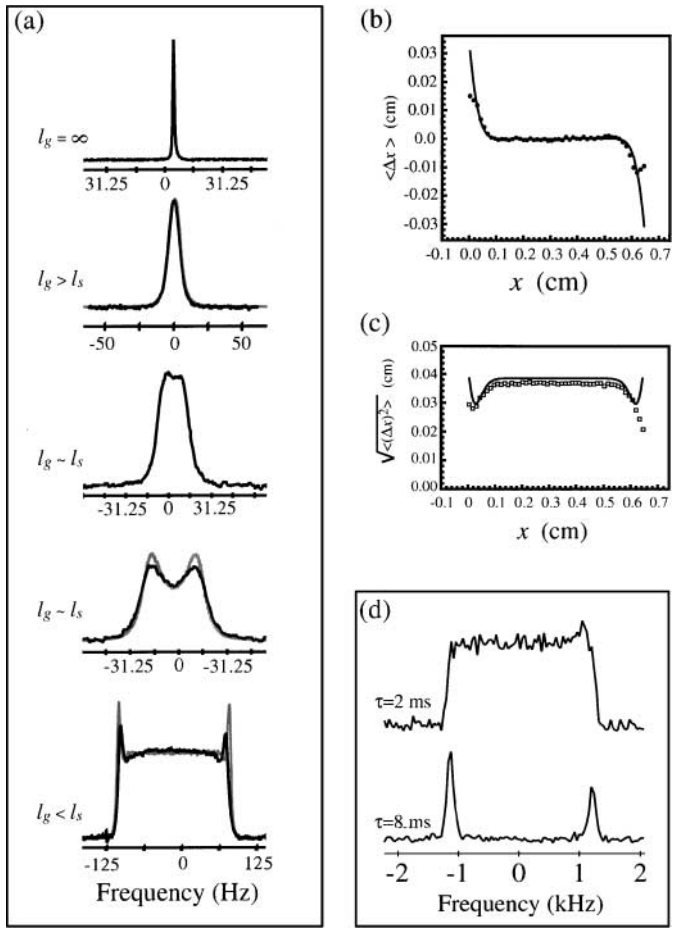

FIG. 28. (a) The 1D ^{129}Xe MR images taken as a function of applied gradient and sample geometry (*196*). The experimental parameters were as follows: for the first four images, the gradient was along y ($l_s = 0.07$ cm), for the 5th image, the gradient was along x ($l_s = 0.66$ cm); the applied gradient strengths were, in G/cm (reading top to bottom), 0.0, 0.24, 0.41, 0.70, 0.25. Simulated images were calculated using the experimental parameters for the 2nd, 4th, and 5th images and are shown in gray. (b) Plot of the mean displacement (first moment) of xenon atoms in the sample as a function of x. Filled circles are data calculated from the measured displacement distribution across the sample, and the curve represents theoretical values from Eq. [44]. (c) Plot of the range of displacement (second moment) of the xenon atoms in the sample as a function of x. Open squares are data calculated from the position-dependent displacement distribution within the sample, and the curve represents theoretical values from Eq. [45]. (d) Demonstration of "active" edge-enhanced imaging. Images were obtained using the pulse sequence described in the text, with τ_1 values of 2 ms (top) and 8 ms (bottom) and a gradient of 3.3 G/cm along x. The bottom image was acquired with 90° excitation pulses and 32 averages; the recycle delay was long enough to allow the diffusion in the sample to replenish the polarized xenon in the space being imaged.

A conceptual understanding of the diffusion-mediated image distortions shown in Fig. 28a is relatively straightforward, at least at the extremes of weak and strong diffusion. De Swiet and Sen (*193*) have introduced a parameter called the diffusion length, l_g, that characterizes these two regimes,

$$l_g = \sqrt[3]{\frac{D}{\gamma G}}, \qquad [42]$$

where D is the diffusion coefficient of the substance and γ is the gyromagnetic ratio of the nuclear spin. Simply stated, l_g is the distance that a molecule will diffuse during the time that its nuclear spins acquire a unit of phase under the influence of a gradient of strength G. Thus, it can be shown (*196*) from a plot of l_g vs G that the maximum imaging resolution that may be obtained from xenon gas imaging is limited to about 100 μm for a typical gradient value in a micro-imaging apparatus (at room temperature and one atmosphere of xenon pressure).

When l_g is much greater than the geometric dimension l_s of the sample along the direction of the gradient vector (i.e., experiments within the strong-diffusion regime), a spin will diffuse throughout the available space before the dephasing from the gradient can occur. In this case an averaged frequency of the nuclear spin is measured. In other words, all of the spins have essentially lost their memory of their initial positions; thus, all have the same average frequency giving rise to a single resonance line, as shown in the second "image" of Fig. 28a. In this regime the effect of the gradient is primarily manifested by an apparent line broadening. Previous theoretical work (*193*) has shown that in this regime the lineshape can be effectively approximated by a Lorentzian.

In circumstances where $l_g \ll l_s$ (i.e., experiments within the weak-diffusion regime), the effects of diffusion are most clearly observed near the edges (where diffusive motion is restricted). This effect can be understood qualitatively in the following manner. Because xenon atoms near the edges of the sample are reflected back upon collision with the edges, the average displacement of these xenon atoms is smaller than the displacement of the xenon atoms in the middle of the sample during the application of the gradient. In other words, the spins near the edges lose their memory slower than those in the middle of the sample, and thus the decay of the signal from spins near the edges is slower than that for spins in the middle. This slower decay in the time-domain signal causes the pronounced, narrow spikes to appear near the edges in the fifth image of Fig. 28a once the signal is Fourier transformed. In addition, the reflection at the edges also leads to each peak being positioned at some distance ($\sim l_g$) from the actual edge. More precisely, theoretical work (*194*) has shown that this distance is equal to $-a_1' l_g$, where a_1' is the first zero of the derivative of the first Airy function, and $a_1' \approx -1.0188$; this value is consistent with the results presented here (*196*) and with those of Saam *et al*. (*195*). It is important to remember, however, that such amplitude variations are only relative, and the integral of the image is actually conserved regardless of the diffusion in the sample in this type of experiment.

Calculations were performed to simulate the diffusion of xenon in the 1D sample in the presence of magnetic field gradients according to the experimental conditions for the 2nd, 4th, and 5th images in Fig. 28a. These simulations (*188, 189*) modeled the effects of xenon diffusion by following the phase accumulated by dimensionless particles making random walks between the sample boundaries. As shown in the figure, the simulations reproduce the experimental results reasonably well in all three cases.

2. *Measurements of the Displacement Distribution*

The difference between the diffusion behavior near the boundaries and that at the center of the sample originates from the impermeability of the glass walls. Xenon atoms adjacent to the sample walls can only diffuse inward, thus altering the displacement distribution of those atoms compared to that of xenon atoms near the center of the sample. This change in the xenon displacement distribution gives rise to two effects: (1) a net displacement of the gas atoms occurs near the edges towards the center; and (2) the range of the displacement for atoms near the edges is significantly reduced. In fact, these two effects correspond, respectively, to the first and second moments of the displacement distribution (which would normally be Gaussian for diffusion in free space). At the sample edges, however, the displacement distribution is neither Gaussian nor symmetric, and thus higher order moments are also significant.

The boundary-restricted diffusive motion was characterized by directly measuring the displacement distribution as a function of position across the sample. Values of both the mean displacement and the second moment of the displacement distribution were calculated for all slices from the displacement distribution and are shown in Figs. 28b and 28c, respectively. The net displacement toward the center of xenon near the edges, as well as a restriction of diffusive motion near the edges, is clearly shown.

By measuring the displacement distribution, one could obtain, for example, a spatially dependent diffusion constant whose values are expected to be larger in the middle of the sample and smaller near the edges. However, it is interesting to note that the second moment of the displacement distribution actually becomes wider *at* the sample's edges (see Fig. 28c); thus, any calculated position-dependent diffusion constant would become greater at the boundaries than values calculated for regions *near* those boundaries. This effect can be rationalized by considering the one-dimensional diffusion of three identical particles over a short time t, with one particle distant from any boundaries, one particle positioned $d/2$ from a boundary, and the last particle positioned at a boundary. The first particle will travel a distance d over t. Over the same amount of time, the particle near the boundary may end up very near its original position due to reflection from a collision with the boundary. The particle at the boundary, however, will tend to travel inward away

from the boundary, free from reflection and traveling a longer distance (on average) than that traveled by the second particle. However, because of the limited spatial resolution in the experimental results shown here, it proved difficult to directly observe this phenomenon.

One may analytically solve the diffusion equation near a one-dimensional wall using a Green's-function approach and obtain the probability of finding an atom at a position x after diffusing from the original position x_0 over a time t:

$$P(x, x_0, t) = \frac{1}{\sqrt{4\pi Dt}}\{\exp[-(x - x_0)^2/4Dt] + \exp[-(x + x_0)^2/4Dt]\}. \quad [43]$$

The position of the boundary is defined to be at $x = 0$. For regions distant from the boundary, $x \gg \sqrt{2Dt}$, this function reduces to the familiar Gaussian form for diffusion in free space. Because the sample dimension is much greater than $\sqrt{2Dt}$, the effect of the other boundary can be neglected, and it is therefore sufficient to consider the effect of only one boundary. The average displacement and the width of the displacement distribution can be calculated using Eq. [43],

$$\frac{\langle \Delta x \rangle}{d} = \sqrt{\frac{2}{\pi}}\left\{ \exp\left(-\frac{x_0^2}{2d^2}\right) + \frac{x_0}{d\sqrt{2}}\left[\operatorname{erf}\left(\frac{x_0}{d\sqrt{2}}\right) - 1\right]\right\}, \quad [44]$$

$$\frac{\langle (\Delta x)^2 \rangle}{d^2} = 1 - \sqrt{\frac{8}{\pi}} \cdot \frac{x_0}{d} \exp\left(-\frac{x_0^2}{2d^2}\right) + \frac{2x_0^2}{d^2}\left[1 - \operatorname{erf}\left(\frac{x_0}{d\sqrt{2}}\right)\right], \quad [45]$$

where $D = \sqrt{2Dt}$ and $\Delta x = x - x_0$. Plots of the calculated $\langle \Delta x \rangle$ and $\sqrt{\langle (\Delta x^2) \rangle}$ values are shown for comparison with the experimentally measured data in Figs. 28b and 28c.

3. Edge-Enhanced Imaging for Boundary Detection

Diffusion-weighted imaging has been utilized in many areas of magnetic resonance imaging (see, for example, Refs. (*10, 199, 200*)), and it has been suggested that the effects of diffusion on MRI can be used to detect impermeable and semipermeable membranes (*188*). It has been shown that diffusion-mediated edge spikes like those seen in Fig. 28a can be used to differentiate between the boundaries and bulk of a sample of laser-polarized gas, and thus represent a "passive" form of edge ehnancement (*195*). However, such contrast between the edge and bulk signals can be significantly increased by the application of a simple pulse sequence that exploits the different diffusive behavior in these regions. In the case of the 1D sample used in the present experiments, one may understand such an "active" edge-enhancement method in terms of a position-dependent diffusion constant, $D(x)$. According to the displacement distribution, $D(x)$ would be effectively smaller near the boundaries; thus the decay of the NMR signals during the application of a magnetic field gradient should be slower for spins near the boundaries and faster spins distant from the boundaries. Therefore, the contrast between the boundaries and the interior of the sample should become more pronounced if sufficient time is allowed for diffusion to occur during the application of the pulse sequence.

The duration of the applied gradient, τ_1, was varied to change the level of contrast between xenon at the boundaries and the bulk. Two of a series of 1D edge-enhanced images are shown in Fig. 28d, taken with $\tau_1 = 2$ and 8 ms. For $\tau_1 = 2$ ms, the diffusion is not significant enough to change the ratio of the signals from the edges and the center of the sample, and thus in such cases an essentially static image is obtained. When $\tau_1 \geq 8$ ms, however, the signals originating from the center of the sample are almost negligible, and only the xenon near the edges of the sample contributes to the images; restricted diffusion at the edges of the sample reduces the decay rate of the signal from these regions. This same effect has been observed in the experiments of Callaghan *et al.* (*191*) using ^{1}H MRI. The asymmetry in peak heights from the sample edges is most likely due to inhomogeneity in the static magnetic field and contributions from imperfections in the sample's geometry.

The simple imaging sequence used can generate enormous contrast between the boundaries and the interior of a sample; however, this feat is accomplished at the expense of the signal intensity. For example, the signal-to-noise ratio for the $\tau_1 = 8$ ms image is approximately two orders of magnitude less than that for the $\tau_1 = 2$ ms image. Even with the use of laser-polarized xenon, some signal averaging was necessary in order to obtain the $\tau_1 = 8$ image.

While it is intuitively appealing to describe the behavior observed in the images of Fig. 28d in terms of a position-dependent diffusion constant, such a model does not correctly describe the functional form of the signal decay for the edges at long times. De Swiet (*194*) has shown that the decay of the signal S at the peaks near the edges changes from a τ_1^3 dependence ($\log(S) \propto -\tau_1^3$), to one that is linearly dependent on time ($\log(S) \propto -\tau_1$). Naturally, this change in the time dependence results in greatly extended signals at long times, and hence produces sharp peaks in the images near the sample's edges following Fourier transformation. In any case, the Princeton and Berkeley work suggest that boundary detection schemes that take advantage of diffusion, in addition to studies of boundary-constrained diffusional motion, may have application to medical and materials imaging using laser-polarized noble gases.

E. Imaging with Continuous Xenon Flow

Recent work has been directed toward the combination of laser-polarized ^{129}Xe gas MRI with continuous xenon flow (*201*). The continuous-flow system described in Section II was modified so that xenon could be continuously recirculated

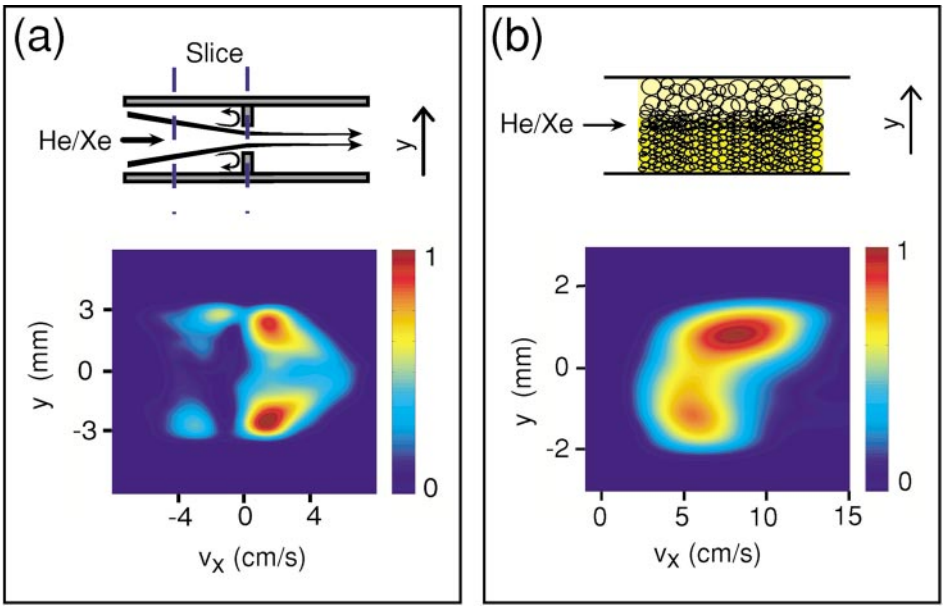

FIG. 29. (Color) Dynamic displacement profiles of laser-polarized xenon flowing through porous materials (*201*). (a) Dynamic displacement profile of laser-polarized xenon flowing through a 3 : 1 constriction. (b) Dynamic displacement profile of laser-polarized xenon flowing through slices of two different polyurethane foams with mean pore sizes of ∼200 μm (top region) and ∼100 μm (bottom region). Note the greater average velocity, as well as the greater spread in velocities, in the top portion of the image. The probability displacement profile is consistent with the pore sizes of the different materials. Figures courtesy of Lana Kaiser.

through a sample within a micro-imaging gradient set. The steady-state nuclear spin polarization of laser-polarized ^{129}Xe can thus be applied without time limitations for MRI of small void spaces in porous materials or the visualization of flow through such systems. Moreover, signals from laser-polarized xenon can be observed using signal averaging and conventional multidimensional imaging pulse sequences that require a steadily renewed source of nuclear spin polarization.

In one application, MR images were obtained of laser-polarized xenon flowing through a collection of glass capillaries, demonstrating the feasibility of imaging under continuous flow of polarized gas. These results suggested that the approach could prove especially useful for imaging studies of porous materials with short longitudinal relaxation times for ^{129}Xe.

The continuous flow of laser-polarized xenon can be further exploited by employing pulse sequences that have velocity-encoding capabilities, permitting various novel experiments designed to study flow in porous materials. For example, PGSE methods may be implemented for simultaneous measurement of a displacement distribution in one dimension and spin density in another orthogonal dimension. In such experiments, a modified PGSE pulse sequence can employ a slice selection gradient chosen in the same direction as the pulsed gradients that encode the flow (*202*). The displacement of the selected gas spins in the flow direction during the fixed time Δ gives rise to a characteristic echo damping (*8*). A second gradient (G_y) is applied to generate the spatial resolution perpendicular to the flow direction. A 2D data set $S(k, q)$ is acquired as a function of $k = (2\pi)^{-1}\gamma G_y t$ and $q = (2\pi)^{-1}\gamma G_x \delta$. This type of combined k-space and q-space imaging is also known as dynamic NMR microscopy (*8*). Fourier transformation with respect to q results in a profile of the displacement probability, containing information about velocity and diffusion. At each point perpendicular to the direction of flow, the mean velocity is given by the position of the signal maximum. The width of the typically Gaussian-shaped line is a function of the apparent diffusion coefficient.

Figure 29a shows the dynamic displacement profile of laser-polarized ^{129}Xe flowing through a glass tube (inner diameter = 6.3 mm) with a 3 : 1 constriction (*201*). The maximum velocity is observed in the center region of the tube ($y = 0$). The relatively low signal intensity in the center region originates from the higher gas velocity in that region (∼7 cm/s), and is not related to differences in longitudinal relaxation. It is interesting to note the two negative velocity components close to the walls of the tube that apparently arise from xenon backflow from the constriction. This behavior originates from secondary flow vortices typical for laminar flow.

A combination of four factors, the Reynolds number (*Re*), determines whether the flow of a fluid through a tube is laminar or turbulent (*203*),

$$Re = \frac{d \cdot v_{ave} \cdot \varrho}{\eta}, \qquad [46]$$

where v_{ave} is the average forward flow velocity, d is the diameter of the tube, ϱ is the density, and η is the viscosity; turbulent flow occurs when $Re \geq 2000$. For the laser-polarized xenon gas

mixture in the glass tube, the Reynolds number did not exceed 30, and thus remained well within the regime of laminar flow. The value used for the viscosity in this calculation was determined according to the equation given in Ref. (*204*) for multicomponent gas mixtures. The difference in the speed of the two components with negative velocity reveals that the constriction hole is not located in the center of the tube, most likely a consequence of the glass-blowing process. The location of the back-flow was upstream of the constriction, verified by velocity profiles taken perpendicular to the flow direction.

Figure 29b shows a dynamic displacement profile of ^{129}Xe flowing through slices of two different polyurethane (PU) foams contained in a 3.5 mm (i.d.) glass tube (*201*). The upper PU foam possessed a lower density and had a larger average pore size (the mean pore radius was determined by optical microscopy to be $\sim$200 μm). In comparison, the medium-density PU foam at the bottom had a smaller pore size, with a mean pore radius of $\sim$100 μm. The mean gas velocity of 5.5 cm/s in the medium density foam is lower than the 8.1 cm/s value observed for the low-density foam; the resistance to flow is naturally greater in the higher-density material (*203*).

A variety of new applications of gas flow MRI are immediately suggested from the above examples. For example, this new technique may have applications in fluid mechanics, as it may aid in the study of flow under various conditions (e.g., under laminar vs turbulent flow regimes). Other possible applications of this nondestructive technique may include the study of restricted diffusion and flow of gases in porous materials and the measurement of pore size distributions in such systems.

Finally, very recent work at Berkeley (*205*) has employed chemical-shift imaging techniques in combination with the continuous flow of laser-polarized xenon to directly visualize gas flow and diffusion within porous media. Specifically, this study was directed at two different samples—fragments of silica aerogel (pore diameter, $<$500 Å), and a collection of zeolite (13X) molecular sieve particles (pore diameter, $<$10 Å)—demonstrating the potential of the approach with both mesoporous and nanoporous materials. Chemical-shift imaging was enabled by the large chemical-shift difference between xenon in the gas phase and xenon occluded in the given materials ($\sim$25 and $\sim$130 ppm, respectively, for xenon in the aerogel and zeolite samples). By using this approach, the authors were able to directly observe the penetration of laser-polarized xenon from the gas phase into the sample particles as a function of time and xenon diffusion constant (determined by the gas pressure and sample temperature). Moreover, it was possible to obtain 3D chemical-shift images with high-resolution, $250 \times 250 \times 100$ μm in the silica aerogel fragments and $100 \times 100 \times 100$ μm in the zeolite particles. Such work may help scientists and engineers obtain a more detailed understanding of flow and diffusion in porous materials used, for example, in catalysis, water purification, soil mechanics, and petroleum engineering.

VIII. BIOMEDICAL APPLICATIONS OF LASER-POLARIZED NOBLE GASES

A. Introduction

Laser-polarized noble gases hold enormous potential for enhancing sensitivity and contrast for a variety of *in vivo* NMR and MRI experiments. In addition to void-space imaging in the body, laser-polarized noble gases could be powerful MR probes of tissues and blood flow. Not surprisingly, research involving the development of biomedical applications of laser-polarized noble gases has been particularly vigorous. Readers of this review can find previous discussions of this field in Refs. (*12, 57, 71, 206–209*); Ref. (*57*) also provides a historical perspective of the field's development.

B. Void-Space Imaging

Void spaces in the body are normally difficult to image with conventional diagnostic methods (e.g., X-ray tomography and ^{1}H MRI) because of the low concentration of signal sources in the gas phase. However, the characteristics that make laser-polarized noble gases advantageous for imaging porous materials (e.g., strong signal and negligible chemical reactivity) also make them extremely promising for imaging void spaces *in vivo*, especially lung space (*57, 71*). Such applications are particularly important in light of the morbidity and mortality associated with many pulmonary diseases and conditions, including asthma, emphysema, pulmonary embolism, cystic fibrosis, lung cancer, and chronic obstructive pulmonary disease (COPD). COPD, a smoking-related illness, is currently the fourth leading cause of death in the United States.

1. Preliminary Experiments

The potential held by polarized gases for novel biomedical studies was first demonstrated in 1994, when laser-polarized xenon was used by the Princeton/SUNY Stony Brook collaboration to image the void spaces in excised mouse lungs (*183*). Three such ^{129}Xe lung space images are shown in Figs. 30a–30c, along with a corresponding ^{1}H image (Fig. 30d). The polarization enhancement afforded by optical pumping permitted multiple images to be acquired with signal-to-noise and spatial resolution (on the order of 0.14–0.28 mm^3) unrivaled by previous methods. Moreover, the region producing large signals near the center of the ^{1}H image (Fig. 30d)—originating from the mouse's heart—corresponds to regions void of signal in Figs. 30b, 30c, demonstrating the potential for obtaining excellent contrast between gas space and tissue in such MRI studies. The ^{129}Xe T_1 was measured to be $\sim$30 s for the gas mixture in the mouse lungs; it was projected that the presence of oxygen necessary for a normally breathing animal would reduce the ^{129}Xe T_1 to $\sim$15 s, still long enough to obtain several bright images. In fact, more recent T_1 measurements by the Duke group polarized gases in the lungs of living guinea pigs yielded values of $T_1 = 28.8$ s for ^{3}He and $T_1 = 31.3$ s for ^{129}Xe (*210*); as expected, the relaxation

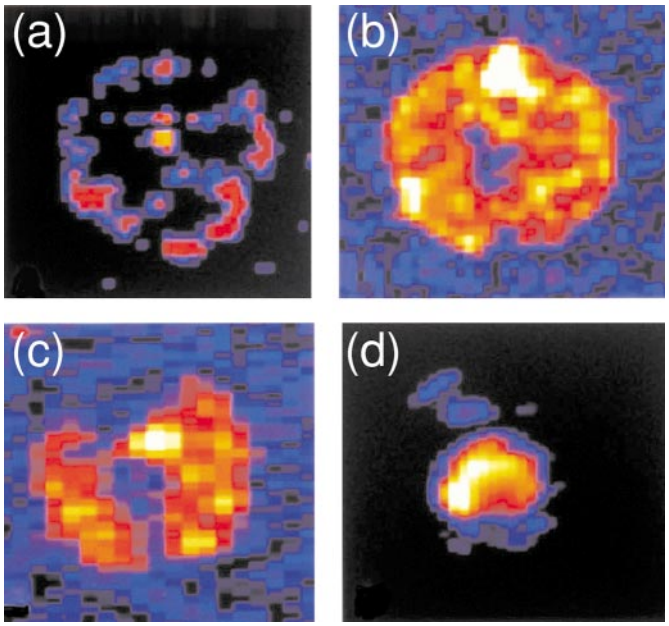

FIG. 30. (Color) MR images taken from the excised lungs and heart of a mouse following delivery of laser-polarized xenon gas (*183*). (a–c) ^{129}Xe images respectively taken ~1 s (a), ~2 s (b), and ~7 s (c) following gas delivery via the trachea. (d) The corresponding ^{1}H image. Note that the bright region (the heart) corresponds to the central signal void in (c). Figures courtesy of Mitchell Albert. Reprinted by permission from *Nature* (**370**:199–201), © 1994 Macmillian Magazines Ltd.

was dominated by paramagnetic molecular oxygen in the lung space. A lower limit for the lung wall-induced relaxation time of 261 s has also been recently measured at Mainz (*211*).

Experiments involving excised animal lungs (*183, 184*) were soon followed by considerable work involving the imaging of polarized xenon and helium in the lung spaces of living animals (see, for example, Refs. (*210–222*)). Indeed, progress in this field has been rapid, as well over a dozen studies involving human subjects have now been performed by several groups in North America and Europe (*211, 220, 223–235*). Delivery of the laser-polarized gas can be achieved easily and in a relatively noninvasive manner via respiration. Such studies could be performed by imaging under continuous-breathing conditions, by gating respiration to the MRI spectrometer to synchronize the breathing cycle with acquisition, or by simply having the patient hold his or her breath during acquisition immediately following inhalation of the laser-polarized gas. Inhalation of laser-polarized xenon and helium has also permitted imaging of the oral cavity, nasal cavity, and paranasal sinuses (*236–238*).

The first demonstration of ^{129}Xe OPMRI in human lungs was performed by the Princeton/Virginia collaboration (*228*). Figure 31 contains a ^{129}Xe MR image taken from the lungs of a healthy human volunteer following respiration of laser-polarized xenon. As with the case of the excised mouse lung images shown in Fig. 30, the correlation between the signal voids in the gray-scale ^{1}H MR image (Fig. 31a) and the bright regions in the corresponding false-color ^{129}Xe MR image (Fig. 31c) is excellent (shown in the image overlay in Fig. 31b).

2. *Maximizing Image Resolution*

Recent experiments at Duke involving both guinea pigs and humans have been performed with the goal of imaging lung space with the highest possible spatial resolution (*217, 218, 220, 221, 229*). Previously, most polarized-gas lung images were performed with conventional pulse sequences (e.g., FLASH and GRASS) under held-breath conditions. The authors point out that such experiments permitted observation of the larger airways in the lungs, as well as gas-exchange areas and outlines of the vasculature of the lungs and nearby tissue. However, such methods do not normally permit the smaller lung airways to be resolved; these airways are obstructed from view at full inspiration by the bright signal from the lung periphery.

By gating the respiration of the subject, the authors could carefully control the timing of the application of the imaging pulse sequence with respect to the breathing cycle, permitting images to be obtained at different points in the respiration process. This ability, combined with the use of a radial acquisition pulse sequence (*239*), permitted fourth-order branchings to be observed in the human lung images, and fifth-order branchings to be observed in the guinea pig lung images.

Three of a series of high-resolution ^{3}He MR images taken from the lungs of a guinea pig are shown in Figs. 31d–31f; such images possess an in-plane resolution approaching $100 \times 100\ \mu m^2$. This resolution is particularly impressive in light of the rapid diffusion of gaseous helium. The radial acquisition technique was chosen partially because it minimizes diffusion effects in images; however, the high resolution obtained may also partially result from boundary-restricted diffusion in the small passageways present in the lungs (refer to Section VII for a discussion of MRI under conditions of boundary-restricted diffusion). Indeed, more recent work from the Duke group (*221*) has measured significantly decreased effective local diffusion constants for both polarized helium and xenon in lung spaces: D for ^{3}He in the trachea of a guinea pig was measured to be $\approx 2.4\ cm^2/s$, but D was measured to be only $\approx 0.16\ cm^2/s$ for helium residing in the minute lung spaces distant from the trachea (a similar trend was observed for ^{129}Xe, with $D \approx 0.068\ cm^2/s$ and $D \approx 0.021\ cm^2/s$ for xenon residing in the trachea and smaller pulmonary spaces, respectively). The measured values for the diffusion constants were also likely affected by the presence of air in the lung spaces, in addition to the effects of boundary restriction.

The Duke Group has recently obtained high-resolution 3D images from the lungs of guinea pigs breathing mixtures of laser-polarized helium and xenon, with voxel sizes of only 0.17 and 0.40 μL, respectively, for the two gases (*217*). The authors noted a one order-of-magnitude SNR advantage for helium over xenon, resulting from xenon's smaller gyromagnetic ratio, faster relaxation in the gas reservoir, and lower achieved polarization

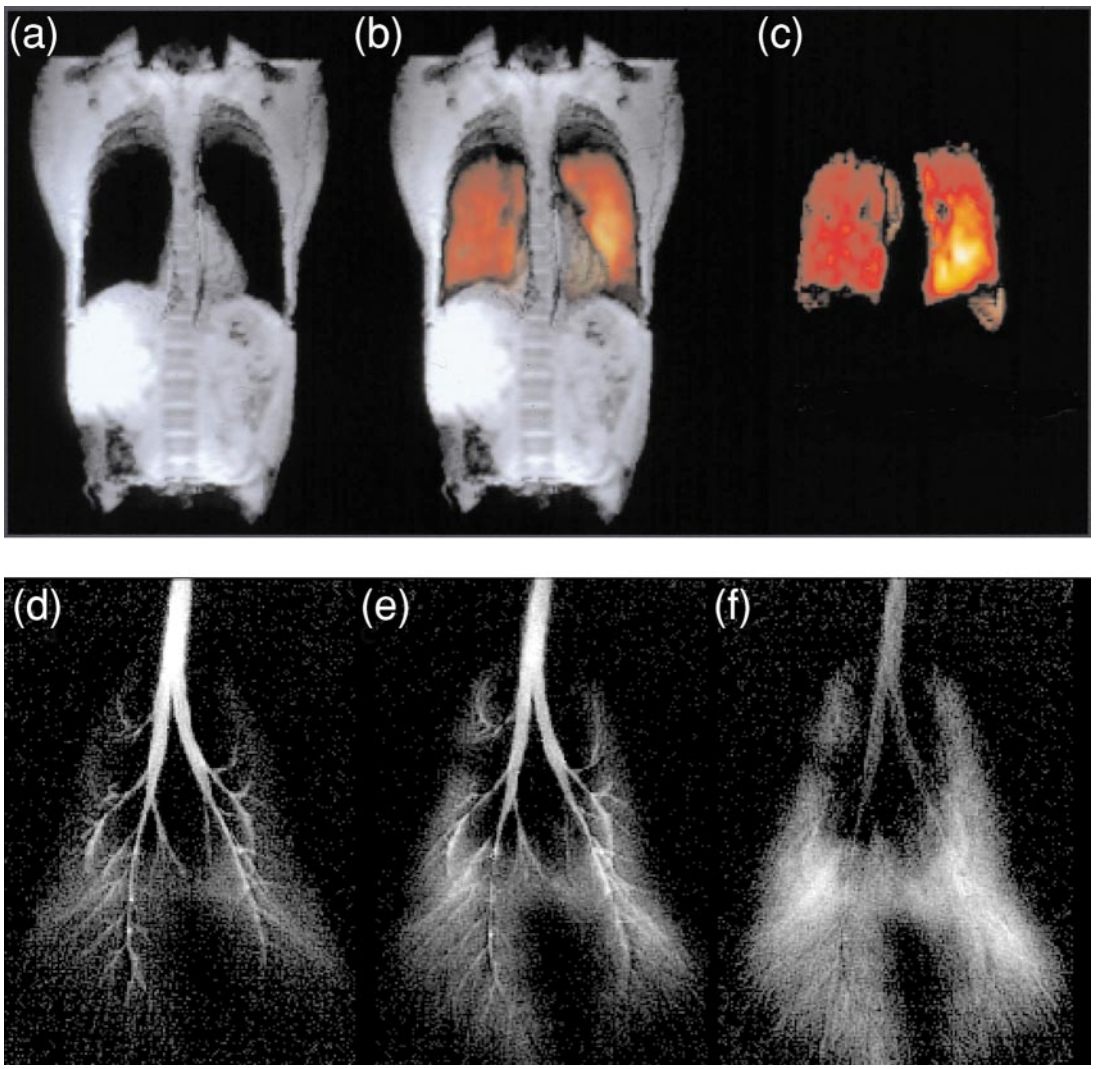

FIG. 31. (Color) Laser-polarized noble gases in the lungs of living organisms. (a–c) *In vivo* MRI of human lung space following respiration of a gas mixture containing laser-polarized xenon (*228*). (a) Gray-scale ^{1}H abdominal image. (b) Composite ^{1}H/^{129}Xe abdominal image comprised of the ^{1}H image in (a) and the false-color ^{129}Xe gas-space image shown in (c). Figures courtesy of John Mugler (d–f) Three of a series of high-resolution, non-slice-selective ^{3}He MR images taken from the lung space of a live guinea pig acquired during respiration of laser-polarized helium (*229*). The timing of the each image acquisition was varied with respect to the gated respiration of the polarized ^{3}He; the images shown were taken following delays of (d) $\approx$0 ms, (e) 200 ms, and (f) 400 ms. Images were obtained with projection-reconstruction methods, involving the mapping of radial trajectories of k-space. Figures courtesy of Mark Chawla and G. Allan Johnson.

and isotopic abundance. The high resolution and SNR in the polarized helium images permitted 5th- and 6th-order branchings to be resolved. These results—along with considerations of reasonable estimates of future ^{3}He polarization and the restricted diffusion of helium in the lungs—suggest that future ^{3}He OPMRI resolution may be fine enough to resolve the lung's smallest gas exchange structures, alveoli and alveolar ducts.

Finally, recent work by numerous groups has been directed toward improving the *temporal* resolution of lung ^{3}He OPMRI. For example, the Washington University (St. Louis) group utilized EPI (echo-planar imaging) methods to achieve 120 ms temporal resolution in ^{3}He OPMRI of human lungs. While the spatial resolution was somewhat diminished when compared to previous human lung OPMR images, the high temporal resolution permitted the compilation of a respiration "movie" with satisfactory resolution and SNR (the movie can be viewed via the Web (*231*)). The Duke group has achieved 50 ms temporal resolution while maintaining high ($<$100 μm) spatial resolution in 2D OPMRI of guinea pig respiration, demonstrating the potential of ^{3}He OPMRI for performing functional studies of the lung with near-microscopic resolution (*218*).

3. *Potential Clinical Applications*

The results of a number of recent experiments suggest that the goal of *clinically* using polarized noble gas imaging for the

routine study of human lungs may soon be realized. The Mainz group demonstrated that lung images obtained from healthy human volunteers breathing mixtures containing laser-polarized ^{3}He can differ dramatically from those of patients suffering from COPD, emphysema, and lung cancer (*227*). Such images can exhibit inhomogeneities corresponding to insufficient ventilation at different positions within the diseased lungs.

Lung imaging with laser-polarized noble gases has since advanced to the point of human clinical trials to test the technique's potential for aiding in the diagnosis and treatment of various pulmonary diseases. For example, the identification of diseased portions of lung tissue may be crucial to treatment for patients suffering from COPD. The experiments shown in Refs. (*227, 233, 235*) suggest that imaging laser-polarized gases in the lungs of COPD patients could be instrumental in helping doctors differentiate healthy and pathological tissue, thereby aiding in the selection of lung regions as candidates for surgical removal. Other work has demonstrated that ^{3}He OPMRI may help detect the early signs of lung transplant failure (known as bronchiolitis obliterans syndrome) (*234*). The potential for using polarized gas MRI for measuring the progression of cystic fibrosis has also been investigated (*232*). Finally, recent technique developments in ^{3}He OPMRI (in addition to the improved spatial and temporal resolution described earlier), including the local measurement of partial O_2 pressure in different portions of the lungs during respiration (*211, 222*), and the combination of ^{1}H perfusion/^{3}He ventilation studies (*219*) should provide detailed descriptions of lung function, thereby greatly improving the means by which doctors can diagnose pulmonary diseases and assess the efficacy of chosen treatments.

As of the time that this review was written, laser-polarized noble gases had not yet attained FDA approval for general clinical use as MRI contrast agents in human patients within the United States. Laser-polarized helium should ultimately have little trouble attaining FDA approval; proponents joke that first they must demonstrate *not* that helium is safe for human use, but that highly spin-polarized helium is safe. However, an arguably less trivial worry of using laser-polarized gases involves the potential exposure of the patient to minute but significant quantities of alkali metal (this, of course, is not a concern for metastability exchange pumping of ^{3}He). Nevertheless, alkali metal vapors and noble gas atoms are easily separated provided simple precautions are taken (see Section II). Xenon, on the other hand, faces a more uncertain timetable for FDA approval because of its (often unwanted) anesthetic properties.

C. Demonstration of Xenon's Potential to Probe Living Tissues: *In Vitro* Studies of Xenon in Blood

While the imaging of lung spaces with polarized gases is extremely promising, it is hoped that *in vivo* applications can be expanded to permit novel studies elsewhere in the body. Unlike the case with lung space imaging, however, there is a manifestly high concentration of excellent signal sources in tissues for conventional NMR/MRI experiments ($[^1H] \sim 80$ M), making the need for using dissolved polarized gases less obvious. However, the signal from polarized gases in tissues need not be greater than the proton signal for a variety of proposed applications to be feasible and useful. The unique characteristics of laser-polarized xenon suggest numerous experiments involving localized ^{129}Xe NMR spectroscopy, chemical-shift imaging, functional MRI, exchange spectroscopy, and blood flow/perfusion studies. Fresh blood is an ideal sample for use in *in vitro* studies to test various potential modalities for future *in vivo* applications using laser-polarized xenon.

1. Preliminary Studies

The prospects for using ^{129}Xe NMR/MRI to probe living tissues were first explored by Albert *et al*. at LBNL with a ^{129}Xe NMR study of thermally polarized xenon dissolved in human blood (*240*). Two peaks were resolved in the ^{129}Xe spectra, assigned to xenon in red blood cells (RBCs) and xenon in plasma. These results demonstrated the ability to simultaneously observe xenon residing in different tissue compartments on the cellular level, and suggested a new means of contrast that could be exploited via chemical-shift imaging (CSI) experiments and *in vivo* localized spectroscopy.

In later work it was shown that laser-polarized xenon could be efficiently delivered to blood samples *in vitro* by predissolving laser-polarized xenon in saline, and subsequently injecting the xenon-saturated solution into open-air test tubes containing fresh human blood (*241*); this injection method is described in detail later in this section. The blood samples used for xenon injection were prepared by allowing the RBCs to settle to the bottom of the tube, and then removing a portion of the plasma. Figure 32 contains two ^{129}Xe NMR blood spectra, one taken by signal averaging acquisitions of thermally polarized xenon over 1.5 h (top), while the second spectrum (bottom) was taken with a single scan following the injection of laser-polarized xenon. In agreement with the previous studies employing thermally polarized xenon, two peaks were observed, corresponding to xenon in slow exchange between RBCs (at $\approx$216 ppm) and their plasma/saline surroundings (at $\approx$192 ppm). However, this exchange in much faster than the relaxation rate of ^{129}Xe, characterized by a common ^{129}Xe T_1 for both signals. The enormous signal enhancement shown in Fig. 32b permitted the ^{129}Xe T_1 to be easily determined from the exponential signal decay observed from multiple acquisitions with small tipping-angle pulses; the ^{129}Xe T_1 was measured to be $\approx$5 s (in the previous study, sedimentation of the RBCs during the extensive signal averaging required to measure the ^{129}Xe NMR signals gave rise to different ^{129}Xe T_1 for the RBCs and plasma: about 5 and 10 s, respectively (*240*).

2. Observation of Xenon Exchange between Blood Compartments

The signal enhancement afforded by optical pumping, in addition to the slow xenon exchange and efficient xenon delivery,

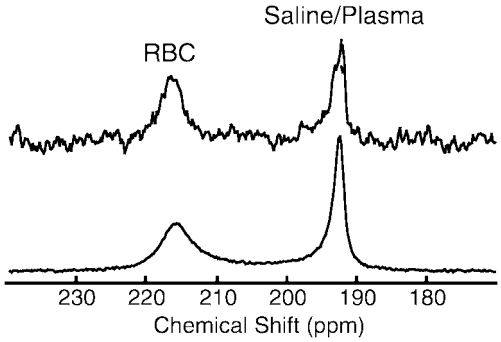

FIG. 32. ^{129}Xe NMR spectra in fresh human blood, with (bottom) and without (top) laser-polarization. The top spectrum was obtained using thermally polarized xenon and accumulating 520 scans over 1.5 h (the xenon over-pressure was about 1 atm). The bottom spectrum was acquired after injection of 1 cc of laser-polarized xenon/saline solution into 1 cc of a concentrated RBC sample (*241*). The ^{129}Xe NMR signal at 216 ppm originates from xenon in the RBC, while the signal at 192 ppm originates from xenon in the saline/plasma mixture (*240, 241*). The signal enhancement between the two spectra is over 2000.

permitted the direct observation of xenon penetrating red blood cells (shown in Fig. 33). By using a frequency-selective 180° RF pulse, the xenon saline/plasma resonance was inverted, and the subsequent recovery of the ^{129}Xe OPNMR signals was followed with low-tipping-angle RF observation pulses. The reduction of the RBC signal, S_{RBC}, and the concomitant rise of the saline/plasma signal, S_{pl}, originate from the intrinsic xenon exchange between the RBCs and the plasma/saline environment. By using a two-site xenon-exchange model, the observed behavior can be described with the following relations,

$$\frac{dS_{RBC}}{dt} = -\frac{S_{RBC}}{\tau_{RBC}} + \frac{S_{pl}}{\tau_{pl}}, \quad [47]$$

$$\frac{dS_{pl}}{dt} = +\frac{S_{RBC}}{\tau_{RBC}} - \frac{S_{pl}}{\tau_{pl}}, \quad [48]$$

where τ_{RBC} and τ_{pl} respectively govern the residence of xenon in the RBCs and plasma. Equations [47], [48] may be solved, yielding

$$S_{RBC} = \left(S^0_{RBC} + S^0_{pl}\right)\frac{\tau_{RBC}}{\tau_{RBC}+\tau_{pl}} + S_0 \exp\left(-\frac{t}{\tau}\right), \quad [49]$$

$$S_{pl} = \left(S^0_{RBC} + S^0_{pl}\right)\frac{\tau_{pl}}{\tau_{RBC}+\tau_{pl}} - S_0 \exp\left(-\frac{t}{\tau}\right), \quad [50]$$

with

$$S_0 = S^0_{RBC}\frac{\tau_{pl}}{\tau_{RBC}+\tau_{pl}} - S^0_{pl}\frac{\tau_{RBC}}{\tau_{RBC}+\tau_{pl}}, \quad [51]$$

where S^0_{RBC} and S^0_{pl} describe the signal intensities for the RBC and the plasma resonances immediately following inversion, and

$$\frac{1}{\tau} = \frac{1}{\tau_{RBC}} + \frac{1}{\tau_{pl}}. \quad [52]$$

Assuming $S_{RBC} + S_{pl}$ is constant over the time of the experiment (a valid assumption in light of the slow rate of ^{129}Xe spin–lattice relaxation relative to the exchange), the observed exponential decay in $S_{RBC} - S_{pl}$ gives $\tau = 12.0$ ms (taking into account the magnetization lost from the application of small tipping-angle pulses to observe the signal). Knowing that the preinversion value of S_{pl}/S_{RBC} constrains the value of τ_{pl}/τ_{RBC}, it can be shown that $\tau_{RBC} = 20.4$ ms, which reflects the mean residence time of xenon in the RBCs.

Given a diffusion constant D for xenon of $\sim 2 \times 10^{-5}$ cm^2 (the approximate value measured in water at room temperature (*89, 242*), one can calculate an average distance $d = \sqrt{6Dt} = 15\ \mu$m that would be traveled via diffusive motion. This value is significantly larger than the dimensions of a red blood cell (a disk $\approx 8\ \mu$m across and roughly $1\ \mu$m thick). Thus, the motion of the xenon during exchange is likely restricted or regulated by some physical or biophysical process, possibly the preferential interaction of xenon with the amphiphilic regions of lipid membranes (*142*).

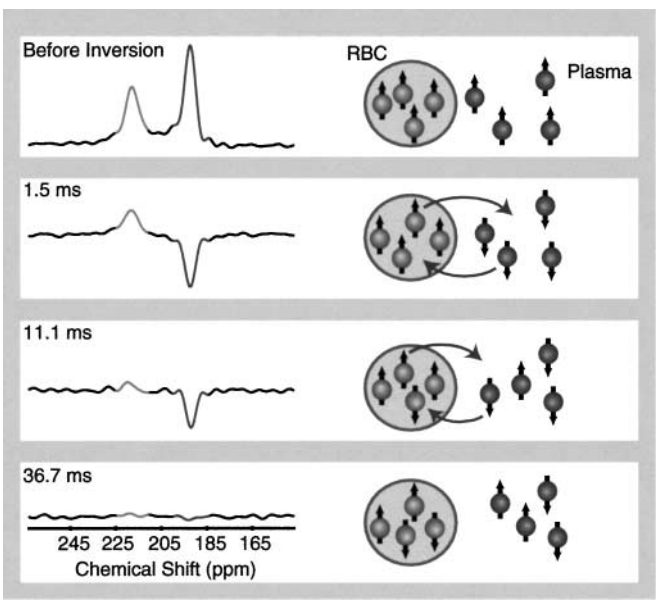

FIG. 33. Direct observation of xenon penetrating red blood cells. Following selective inversion of the Xe/plasma resonance, the time dependence of the ^{129}Xe spectra was monitored via the application of multiple low tipping-angle RF pulses, as shown in the selected spectra. The recovery of the two xenon resonances to a new equilibrium reflects the intrinsic exchange of xenon between the red blood cells and the plasma (*241*). The inversion pulse was an amplitude-modulated (Gaussian) pulse of 1-ms duration centered at the saline/plasma signal; this pulse also reduced the absolute intensity of both signals by about 50%. A 1-ms gradient pulse was applied immediately following the inversion in order to dephase any remaining transverse magnetization.

3. Dependence of Xenon Spin–Lattice Relaxation on Blood Oxygenation

More recent work has investigated the role of blood oxygenation in the observed ^{129}Xe T_1. It is well known that blood oxygenation levels vary considerably among different tissue environments and physiological conditions; for example, the partial pressures of oxygen (p_{O_2}) in the well-oxygenated blood found in alveoli and arteries are about 100 and 95 torr, respectively, while $p_{O_2} \approx 20$ torr for capillary blood draining from active muscle tissue (*243*). In both previous studies mentioned above, the xenon was dissolved in blood with relatively low (ambient) oxygen concentrations. However, work at Harvard/Brigham and Women's Hospital has shown that higher blood oxygen concentrations correlate with *longer* ^{129}Xe T_1 values (*57*), a result that at first seems to counter intuition. This sensitivity of the ^{129}Xe T_1 to the oxygenation level of hemoglobin is believed to originate from the binding of xenon to hydrophobic pockets in hemoglobin (*133*); the subsequent binding of oxygen to hemoglobin apparently changes the relaxation efficiency between xenon and hemoglobin (some potential underlying mechanisms of this effect are discussed in greater detail below). It should be noted, however, that in studies of polarized xenon in blood foam (*244*), the opposite trend in T_1 was observed (i.e., the ^{129}Xe T_1 was *longer* in deoxygenated blood foam). While the origin of this disparity is uncertain, the authors of the blood foam work point out that extrapolation of their observations to normal physiological conditions gives a ^{129}Xe T_1 of $\sim$5 s.

Nevertheless, the observed increase in xenon T_1 with increasing blood oxygenation was recently confirmed by work at ICR/London and at Harvard. The ICR/London group carefully controlled the experimental conditions (e.g., temperature, magnetic field, RBC concentration, and oxygenation level) of *in vitro* samples of laser-polarized xenon in human blood. At body temperature (37°C) and 1.5 T, ^{129}Xe T_1 values were measured to be 6.4 ± 0.5 s and 4.0 ± 0.4 s for xenon in blood samples whose oxygenation levels matched those of arterial and venous blood, respectively (*139*). This work also studied xenon relaxation in blood plasma; a competitive ligand (flucloxacillin) "titration" in albumin solutions suggested that xenon binding to albumin contributes significantly to the observed ^{129}Xe T_1 in plasma (measured to be about 13.2 s in plasma equilibrated with air) (*139*).

The Harvard group recently studied the oxygenation dependence of ^{129}Xe T_1 in blood and lysed RBC samples using thermally polarized xenon at 3–4 atm overpressure (measurements performed with lower xenon overpressures did not show significant differences from those obtained at higher pressures) (*245*). To prevent sample degradation during the experiment, blood samples were kept at 8°C; additionally, blood samples were gently but continuously agitated to prevent RBC sedimentation during signal averaging. The results consistently showed increased ^{129}Xe T_1 with increased sample oxygenation. In samples of lysed RBCs, ^{129}Xe T_1 values of 2.86 and 10.2 s were measured for deoxygenated and oxygenated samples, respectively. Measurements of xenon in whole blood samples obtained values of 2.7 s for RBCs and 3.7 s for plasma in deoxygenated blood (the difference was believed to originate from the relatively low SNR in the data and was not considered significant by the authors), compared to 7.9–8.0 s measured for the xenon in the compartments of oxygenated blood. Poisoning the blood with carbon monoxide increased the observed ^{129}Xe T_1 to over 11 s. The authors suggest two possible explanations for the observed increase of ^{129}Xe T_1 with increasing blood oxygenation: in addition to the reduction of hemoglobin's paramagnetism upon oxygen binding (the authors remind us that the ratio of bound O_2 to paramagnetic "free" O_2 dissolved in blood is about 100 : 1 under normal physiological conditions), it is suggested that conformational changes in the structure of hemoglobin upon O_2 binding (*246*) may in some way hinder xenon binding and subsequent relaxation through xenon–hemoglobin interactions.

4. Dependence of Xenon Chemical Shift on Blood Oxygenation

Both of the above studies also observed an apparent change in the *chemical shift* of the RBC ^{129}Xe resonance between oxygenated and deoxygenated blood, an effect which has subsequently been studied in more detail at ICR/London (*247*). Increased blood oxygenation is observed to drive the RBC

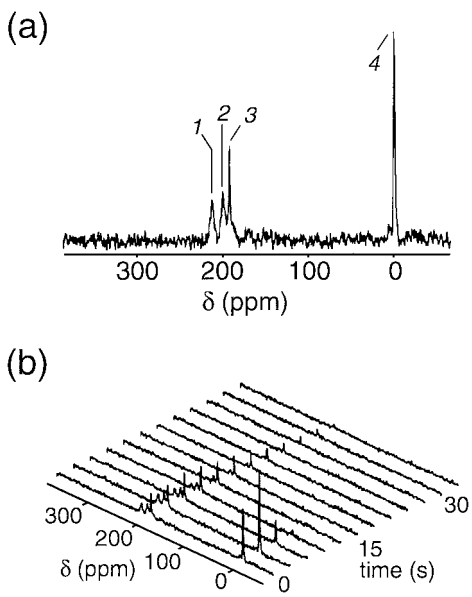

FIG. 34. *In vivo* ^{129}Xe OPNMR spectroscopy (*213*). (a) ^{129}Xe NMR spectrum from the thorax of an anesthetized rat following respiration of laser-polarized xenon. The spectrum was tentatively assigned as follows: 1, red blood cells; 2, lung tissue; 3, blood plasma/adipose tissue; 4, Xe gas. (b) ^{129}Xe NMR spectra showing the dynamics of the xenon resonances in different tissue compartments. Figures courtesy of Arvind Venkatesh and Mitchell Albert.

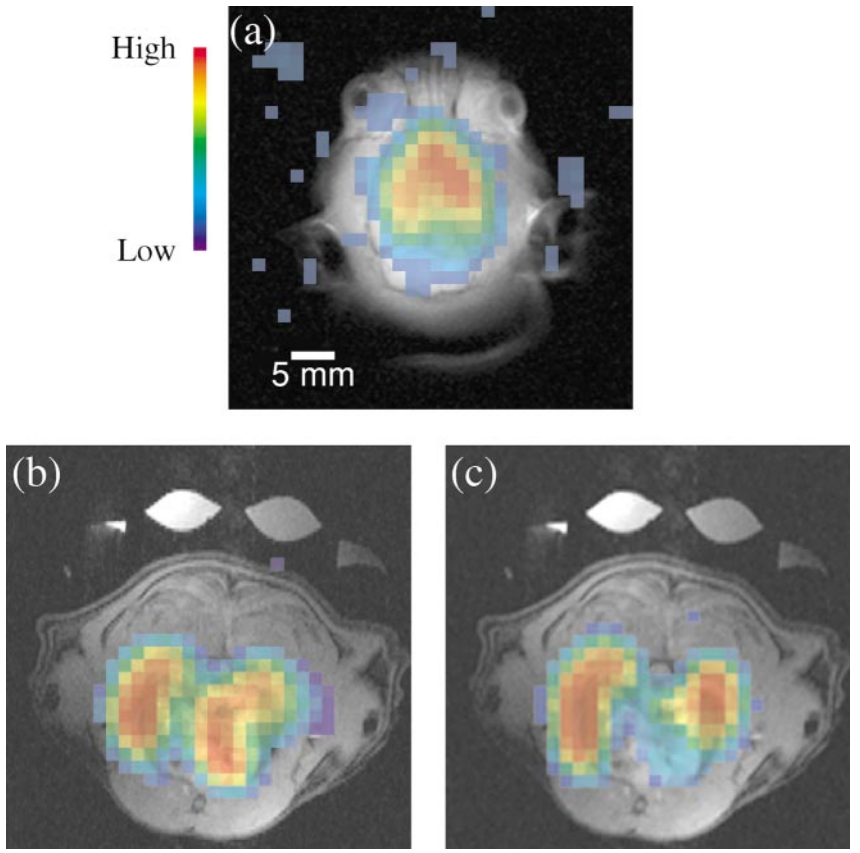

FIG. 35. (Color) *In vivo* ^{129}Xe chemical-shift images from tissues in rats following laser-polarized xenon respiration, with each ^{129}Xe image shown as a false-color overlay of the corresponding gray-scale ^{1}H image. (a) Xenon in brain tissue (*251*). (b,c) Axial, cross-sectional CS images taken from a rat's thorax, respectively showing xenon in blood (b) and in lung tissue and myocardium environments (c) (*253*). Figures courtesy of Scott Swanson.

resonance downfield (i.e., to higher frequency); additionally, the largest downfield shift was observed in blood poisoned with carbon monoxide. However, the extracellular (plasma) resonance was not observed to have a significant dependence upon blood oxygenation or upon which gas was in equilibration with blood (air, nitrogen, oxygen, or carbon monoxide).

The observed dependence of the ^{129}Xe shift on the blood oxygenation level was nonlinear, with the shift becoming far more pronounced at higher values of oxygenation. The range of shifts observed for the RBC resonance was over 5 ppm. This large range, in addition to its nonlinear behavior, suggested that the effect cannot be explained only by bulk suceptibility effects in RBCs or a direct paramagnetic shift arising from the reduced paramagnetism of hemoglobin. Indeed, previous studies of the dependence of the ^{129}Xe shift on the heme iron's paramagnetism in hemoglobin solutions was shown to be considerably weaker (*86*); moreover, unlike the case with myoglobin, X-ray crystallography studies have shown that the primary xenon binding site in hemoglobin is distant from the heme (*133*). Instead, the authors believe that their results point to an oxygenation-dependent hemoglobin affinity for xenon—possibly resulting from the conformational changes in hemoglobin known to occur upon oxygen binding (*246*)—echoing one suggested origin of the T_1 dependence mentioned above. Certainly, the molecular origin of the dependence of xenon's relaxation and chemical-shift behavior on blood oxygenation warrants further study.

Regardless of its exact origin, the highly sensitive oxygenation dependence of the ^{129}Xe shift in the physiologically relevant range of blood oxygenation (i.e., between venous and arterial blood), in addition to the convenient internal reference provided by the oxygenation-insensitive extracellular resonance, demonstrates that the ^{129}Xe chemical shift could be a sensitive, quantitative probe of blood oxygenation in tissues. Possible applications may include functional MRI and the identification of cancerous tumors by their steep variation in local oxygenation.

D. Enhanced *In Vivo* NMR and MRI via Xenon Respiration

1. Temporal Dynamics of ^{129}Xe Resonances in Tissues

The respiration of a breathing mixture containing laser-polarized xenon by rats permitted enhanced ^{129}Xe NMR spectra to be obtained *in vivo* (*213*); a series of *in vivo* ^{129}Xe spectra

are shown in Fig. 34. The spectrum in Fig. 34a shows three separate tissue resonances downfield from the gas-phase signal originating from xenon in the rat's lungs (at 0 ppm); these tissue resonances were tentatively assigned to xenon residing in red blood cells (at ≈213 ppm), lung tissue (at ≈199 ppm), and blood plasma/adipose tissue (at ≈191 ppm).

Clearly, the xenon exchange is slow enough to permit the four distinct resonances from the different compartments to be observed. Moreover, by rapidly acquiring ^{129}Xe NMR signals following the rat's breathing cycle, the dynamics of the different xenon resonances could be observed (Fig. 34b). The observed time dependence reflects the "wash-in"/"wash-out" dynamics of the xenon as it passes through the lungs to different tissues in the body, modulated by the spin–lattice relaxation of the laser-polarized xenon and the polarization destruction originating from RF observation pulses. Intrinsic ^{129}Xe T_1 values are difficult to measure in such circumstances because the concentration of laser-polarized xenon is changing with time. Instead, the "apparent" decay constants, T_1^*, of the ^{129}Xe NMR signals were obtained directly from the spectra in (Fig. 34b): 12 s for the xenon/RBC resonance, 26 s for the xenon/lung tissue resonance, and 50 s for the xenon/plasma/adipose tissue resonance. These results demonstrated the feasibility of using laser-polarized xenon to perform *in vivo* ^{129}Xe chemical-shift imaging and to characterize local blood flow in living tissues.

2. *Xenon in Brain Tissue and Its Potential for Probing Brain Function*

Arguably, the organ that has attracted the greatest interest for study via MRI is the brain. It has been proposed that differences in the relaxation parameters, chemical shift, and solubility of xenon in various tissues under different physiological conditions may provide considerable contrast enhancement that could be exploited for several purposes, including functional MRI of the brain (*57*). A number of approaches have been suggested to exploit the characteristics of laser-polarized xenon to probe brain function. For example, one potential method would combine two effects expected to increase local ^{129}Xe signal in a manner that would correlate with increased brain activity: (1) a rise in regional blood flow that will result in a transient increase in local polarized xenon concentration, and (2) the longer spin–lattice relaxation time of xenon in oxygenated versus deoxygenated blood (discussed previously) (*57*). This method would therefore be somewhat similar to BOLD (blood oxygenation level dependent) contrast experiments (see, for example, Refs. (*248–250*), where the higher paramagnetism of deoxygenated hemoglobin is exploited to deplete MR signal from blood water protons via (transverse) relaxation-weighted methods. Another approach would exploit the apparent chemical shift difference between xenon in oxygenated versus deoxygenated blood (*139, 245, 247*), a prospect discussed at length in Ref. (*247*). By using polarized xenon for such studies, it is hoped that changes resulting from brain function could be observed with higher dynamic range (i.e., greater contrast) and without background signal.

Additionally, the differential solubility of xenon in various tissue compartments could provide a novel form of contrast. The concentration of protons differs little across various regions of the body, often giving poor contrast when simply mapping proton density via MRI; however, the xenon concentration can vary by over an order of magnitude between aqueous and lipid-rich environments. Moreover, lipid-rich tissues are typically difficult to image via conventional ^{1}H MRI, because lipid protons usually suffer from rapid transverse relaxation (T_2). Thus, polarized xenon may be potentially useful for studying lipid-rich regions of the body, such as neural tissue (*57*).

^{129}Xe OPMRI of the brain was first performed by the Michigan group, who imaged the head region of a laboratory rat following respiration of laser-polarized xenon (*251*). The first such ^{129}Xe brain image is shown in Fig. 35a as a false-color overlay upon the corresponding gray-scale ^{1}H MR image. From the image it is clear that the ^{129}Xe signal clearly originates from the rat's brain, predominantly in the cerebrum. A lower limit for T_1^* for the brain tissue resonance was estimated to be ∼30 s (*252*). Additionally, respiration of laser-polarized xenon by human patients has also produced detectable ^{129}Xe NMR signals originating from the patient's head region, most likely in the brain tissue (*228*).

3. *Xenon in Vivo Chemical-Shift Imaging*

Recently, the resolved differences in chemical shifts for xenon residing in different tissues have been exploited to demonstrate *in vivo* ^{129}Xe chemical-shift imaging (CSI) following respiration of laser-polarized xenon by laboratory rats (*253*). Two ^{129}Xe CS images can be found in Figs. 35b, 35c, which respectively show false-color images of xenon residing in blood (Figs. 35b) and tissue (Fig. 35c), each overlaid upon a gray-scale ^{1}H MR image corresponding to the same region in the rat's thorax. The ^{129}Xe signal in Fig. 35b corresponds to xenon residing in blood in the rat's heart and lung vasculature, while the ^{129}Xe signal in Fig. 35c was attributed to xenon residing in the rat's lung tissue and myocardium.

It is interesting to note that in this study, only one resonance was observed that could be assigned to blood in the ^{129}Xe NMR spectra (with a chemical shift of ∼210 ppm, obtained, for example, from localized NMR spectroscopy from the rat's heart region) (*253*). This result suggests that under the conditions of their experiment (e.g., xenon dissolved in rat blood *in vivo* at 37°C and 2 T) the xenon exchange between RBCs and plasma was fast with respect to the the NMR time scale, in contrast to the previous *in vitro* results described above (*240, 241*). Indeed, this result is particularly surprising considering the new results from the ICR/London group (*139*), where the xenon exchange in human blood was still slow on the NMR time scale even though the experiments were performed at 37°C (body temperature)

and only 1.5 T. The origin of this disparity is uncertain, but the possibility that it originates from some differences in sample preparation (e.g., *in vitro* vs *in vivo* samples), or even some difference between the behavior of xenon exchange in human and rat RBCs, has yet to be determined. Nevertheless, based on their results the authors of the *in vivo* rat work suggest a slight alteration of the assignment of the three tissue resonances (like those observed in Fig. 34); 210 ppm, blood; 199 ppm, tissue (e.g., lung parenchyma); and 192 ppm, epicardial fat. Certainly, such ^{129}Xe CSI experiments could become a powerful diagnostic tool, permitting lung ventilation and perfusion to be studied simultaneously.

E. Injection Delivery of Laser-Polarized Gases

In certain circumstances, the use of polarized gases for tissue studies may be limited by the difficulty of delivering the gas to targeted regions with high enough local concentration and polarization. Indeed, overcoming such difficulties may be critical to the ultimate viability of many proposed *in vivo* studies. Respiration delivery can suffer from many factors that may ultimately limit the concentration and polarization of laser-polarized gas that can be achieved in tissues, especially those distant from the lungs. When delivered by respiration, polarized xenon is diluted throughout the body. More worrisome, however, are the short spin–lattice relaxation times of ^{129}Xe in some living tissues (e.g., blood). Thus, much of the polarization may be destroyed in transit before the xenon has reached tissues distant from the lungs. Respiration also requires the preparation and use of large volumes of polarized xenon for human tissue studies, making it financially impractical to use isotopically enriched xenon to increase the signal; the cost of ~80% ^{129}Xe-enriched xenon is roughly two orders of magnitude higher than xenon with natural ^{129}Xe abundance. Additionally, the anesthetic properties of xenon may in some circumstances limit its concentration in breathing mixtures. Finally, respiration delivery is limited to xenon because of the low solubility of helium in tissues.

At the cost of increasing the invasiveness of the experiment, the injection of biologically compatible polarized gas carriers may prove useful for combating all of the difficulties concerning tissue delivery mentioned above (*12, 254*). Various solvents can be chosen which possess high xenon solubility, and which partition xenon away from paramagnetic centers in the body, thereby increasing the *in vivo* ^{129}Xe MR signal. Instead of dissolving the noble gas, it has also been shown that stable gas bubbles and gas-filled microspheres can be formed in certain solutions, thereby permitting helium gas to be administered to the body in relatively large amounts for use as an MRI tracer. The injection methods permit rapid, efficient, and localized delivery of the polarized gas to a targeted region in the body. However, it is important that the advantages of injection delivery be weighed carefully against the possible danger of increasing the invasiveness of any study (diagnostic or otherwise) involving human subjects.

Models predicting the amount of polarized xenon that could be delivered to tissues via respiration and injection can be found respectively in Refs. (*255–257*). The simple injection model in Ref. (*257*) suggests that injection delivery of laser-polarized xenon dissolved in a lipid suspension (described later) could improve the local concentration of polarized xenon in the brain by severalfold over what could be achieved by respiration (as predicted by a model for respiration delivery (*256*)). This predicted increase in peak polarized xenon concentration primarily originates from rapid, localized xenon delivery, high initial concentration (obtained with high xenon solubility in the injectable carrier solution) and extended *in vivo* ^{129}Xe relaxation time. However, it should be noted that the peak polarized xenon concentrations predicted by such models depend greatly upon the values of the experimental and physiological parameters used in the calculations, some of which are not well-known for all physiological conditions.

1. Experimental Methods

The original implementation of noble gas injection dates back to the 1960s and involved the injection of saline solutions containing dissolved radioactive xenon isotopes (e.g., ^{133}Xe) to study local blood flow in muscular tissue (*258, 259*). However, only recently was injection explored in conjunction with delivering laser-polarized xenon (*241*) to exploit the intrinsic advantages of magnetic resonance techniques (e.g., high spatial resolution, improved contrast and signal-to-noise, and lack of ionizing radiation).

Injectable polarized gas carrier solutions may be prepared according to the simple procedure described below. Following batch optical pumping, polarized xenon is frozen into the cold-finger of the storage vessel (dubbed the "shaker") for the gas solvent and stored while exposed to a magnetic field provided, for example, by a strong permanent magnet. Once the shaker has been transported to the NMR spectrometer, the xenon is rapidly sublimated and delivered at moderately high pressure (a few atm) to a degassed, nontoxic solution. Such solutions are chosen in light of their respective gas spin-relaxation, solubility, and partitioning properties. Degassing the solution removes paramagnetic oxygen from the solution, thereby increasing the polarization lifetime of the dissolved xenon. Following vigorous shaking, the xenon-saturated solution is withdrawn through a high-pressure septum with a syringe, and subsequently injected into the sample of interest. For *in vivo* studies, the injection can be administered intravenously, intraarterially, or directly into the target organ, depending on the application. Intraarterial injection is often the most efficient route for tissue delivery, but is also generally the most invasive.

2. Investigations of Potential Noble Gas Carriers

Saline is a good carrying agent for laser-polarized xenon because it possesses a long ^{129}Xe T_1 (≈66 s, ~1000 s when deuterated (*241*)) and high biological compatibility. However, it

possesses a xenon Ostwald solubility coefficient of only 0.0945 at 27°C (*260*), yielding a concentration of only ~4 mM/atm. The Ostwald coefficient is derived from the volume, at standard temperature and pressure, of a gas that can be dissolved in 1 L of liquid at 1 atm of gas pressure for a given temperature. For comparison, the Ostwald solubility of xenon in blood is about 0.18 (*260*). Furthermore, in many circumstances it would be desirable to partition the xenon away from paramagnetic centers in the body, thereby increasing the observed T_1 following injection. For these reasons, a variety of alternative noble gas carriers have been investigated for potential *in vivo* use.

One class of noble gas carriers is lipid emulsions. The first such carrier to be investigated was Intralipid (Pharmacia), an aqueous suspension of lipid vesicles known to be well-tolerated biologically; in fact, Intralipid emulsions are used clinically as nutrient supplements in hospitals. The ^{129}Xe T_1 in 20% Intralipid solutions was determined in different studies to be 40 s (*241*) and 49 s (*261*). The ^{129}Xe spectrum taken from a xenon/Intralipid solution injected into a test tube of human blood shows a strong resonance at ≈194 ppm (corresponding to xenon in the Intralipid), over six times greater than the signal from xenon residing in red blood cells at ≈216 ppm. This observation is consistent with the lipophilic nature of xenon and is responsible for two desirable effects: (1) higher xenon concentration (roughly 4 times that of saline) and (2) extended polarization lifetime in the blood, with a new ^{129}Xe T_1 of 16 s (for the Intralipid resonance).

Another class of substances that has been investigated for carrying xenon is perfluorocarbon compounds and their emulsions. These substances are of particular interest in the medical community because of their ability to dissolve and transport oxygen and carbon dioxide, making them potentially useful as blood substitutes (*262*). The first perfluorocarbon substance studied was Fluosol (Green Cross), a 20% perfluorodecalin emulsion. The *in vitro* injection of a polarized xenon/Fluosol solution into human blood yields two peaks in the enhanced ^{129}Xe spectrum: A now-familiar peak at 216 ppm corresponds to xenon in the red blood cells, and a second signal from xenon residing in the Fluosol that is significantly broader (roughly 80 ppm wide, most likely broadened from exchange). The width of this second peak makes Fluosol unfavorable for carrying polarized xenon for the purposes of tracing local blood flow. However, it is interesting to note that the T_1 of the ^{129}Xe red blood cell signal was 13 s, a significant increase from that observed when xenon is delivered in saline. This T_1 extension suggests that Fluosol may be useful as a xenon "reservoir" for chemical-shift imaging and localized spectroscopy of tissues.

Numerous other perfluorinated compounds have since been studied for use as possible polarized xenon carriers. Pure perfluorooctyl bromide (PFOB) possesses a high xenon Ostwald solubility (~1.2 (*263*)) and can be injected in relatively small volumes (*261*); xenon residing in the PFOB produces a strong signal at 106 ppm (*263*). No signal is observed that could be assigned to xenon residing in the tissues (*261*). Thus, pure PFOB appears to be very effective at partitioning the xenon away from paramagnetic species in the blood and other tissues, a fact especially evident in the long effective ^{129}Xe T_1 of 94 s (*261*). However, the perfluorocarbon substances must ultimately be emulsified in order to facilitate tissue absorption. Thus, other work has been directed towards optimizing the emulsions of perfluorinated compounds. For example, the composition of PFOB emulsions was varied in order to maximize xenon concentration, while minimizing the broad linewidth of the ^{129}Xe signal normally observed in perfluorocarbon emulsions (*263, 264*). By varying the concentration of the emulsifying agent (egg lechithin) in a 90% (weight/volume) PFOB emulsion, the exchange rate of xenon between the PFOB "droplets" and their surroundings could be altered. The lower the emulsifier concentration, the larger the droplet size, and the slower the exchange, yielding a narrower Xe/PFOB signal. With 0.85% emulsifier, the average PFOB droplet size was roughly 2 μm and gave a relatively narrow linewidth for the ^{129}Xe/PFOB resonance ($\leq$3 ppm). Lowering the emulsifier concentration further yielded larger PFOB droplet sizes and narrower lines, but made the emulsions more unstable.

Instead of dissolving the polarized noble gas in a solution, it has also been suggested that injection could be used to deliver it in *gaseous* form. For example, it has been shown that liposomes can be stably prepared to contain polarized xenon gas (*265*). Solutions of these xenon-filled liposomes can then be safely injected into living organisms. The observed ^{129}Xe T_1 of xenon gas in the liposomes once intravenously injected into a laboratory rat was as long as 54 s (*265*).

By flushing polarized helium gas through Hexabrix (Mallinckrodt), a viscous, commercially available radiographic contrast agent, polarized helium microbubbles could be formed and stably suspended (*266*). The ^{3}He T_1 was measured to be at least 42 s in the microbubble suspension. While the sizes of the microbubbles were larger than what would be desired for clinical use (≈32 μm, with a standard deviation of about 10 μm), this approach demonstrates the feasibility of utilizing the higher signal afforded by laser-polarized ^{3}He as a magnetic resonance tracer of blood flow. In order for the helium injection approach to be clinically feasible, the average dimension of the microbubbles must be decreased toward the size of red blood cells to ensure safe circulatory passage; therefore, future attempts will be directed towards decreasing the microbubble size and increasing their effective concentration, while retaining a suitably long ^{3}He T_1. Indeed, the same group has recently demonstrated the creation and *in vivo* use of solutions containing polarized helium-filled microspheres (*267*). The microspheres (Point Biomedical), each comprised of a bioabsorbable polymer sphere surrounded by a shell of cross-linked human serum albumin, can be created with different sizes (microspheres with diameters of 5.3 ± 1.3 and 10.9 ± 3.0 μm were used in this study) with relatively narrow size distributions. A summary of experimental data regarding a number of potential polarized noble gas carriers is reprinted in Table 5 (*12*).

TABLE 5
Summary of Properties of Potential Noble Gas Carriers

Carrier	Ostwald solubility	Gas T_1[a]	Gas T_1 in tissue[a]	Chemical shift[a]
Saline	0.0945 (*260*) (27°C)	66 s (*241*)	5 s (blood) (*241*)	~192 ppm (*241*)
DMSO	~0.66 (*268*) (25°C)	100's of seconds	n/a	245.8 ppm (*269*)
Olive oil[b]	2.04 (*260*) (27°C)	n/a	n/a	198 ppm (*79*)
Intralipid (20%)	~0.4 (*241*)	40 s (9.4 T) (*241*) 49 s (4.7 T) (*261*)	16 s (blood) (*241*)	194 ppm (*241*)
Intralipid (30%)	~0.6 (*270*)	25 S[c] (2 T) (*271*)	n/a	194.5 ppm (*270*)
Lyposyn II	~0.4 (*270*)	23 S[c] (2 T) (*270*)	n/a	194.5 ppm (*270*)
Lecithin[b]	1.477 (*268*) (37°C)	n/a	n/a	200.6 ppm (*79*)
PFOB	~1.2 (*263*)	n/a	97 s (rat) (*261*)	106 ppm (*263*)
PFOB (20%)	~0.22[d]	110 s (*261*)	34 s/67 s (blood: RBC/PFOB) (*261*)	~110 ppm (*261*)
PFOB (90%)	~0.62[d]	n/a	n/a	111 ppm (*263*)
Perfluortributylamin	1.513 (*272*) (20°C)	n/a	n/a	n/a
Fluosol (20%)	~0.3	n/a	13 s (blood: RBC) (*241*)	~110 ppm (*241*)
Oxyphenol (20%)	0.251 (*272*)	n/a	n/a	n/a
Gas-filled liposomes	n/a	118 s (114 s in saline) (*265*)	45 s blood); 54 s (rat) (*261*)	~0.5 ppm (*265*)
Hexabrix/^{3}He gas	[e]	~42 s (for ^{3}He) (*266*)	n/a	~0 ppm (^{3}He)
Microspheres/^{3}He gas	[f]	64 s (for ^{3}He) (*267*)	13 s (blood) (*267*)	~0 ppm (^{3}He)

[a] For ^{129}Xe, unless otherwise stated.
[b] Listed for comparison.
[c] Lower value than that determined for Intralipid (20%) may indicate a field-dependent relaxation rate.
[d] Estimated from the xenon solubility in pure PFOB and the volume/volume ratio of the mixture.
[e] About 20% of the injected volume was polarized helium gas in the form of microbubbles.
[f] About 7% of the injected volume was polarized helium gas.

3. In Vivo Studies

The feasibility of using injectable carriers of laser-polarized xenon to perform *in vivo* NMR and MRI was first demonstrated at Berkeley in living laboratory rats (*257*). In one experiment, a saturated polarized xenon/Intralipid (20%) solution was injected intravenously into a rat's tail vein. The surface coil was used to monitor ^{129}Xe NMR signals from the rat's liver region, permitting the wash-in/wash-out dynamics of the xenon in this region to be observed.

In a second experiment, ^{129}Xe MR images were obtained following intramuscular injection of a saturated polarized xenon/saline solution into the upper hind leg of a laboratory rat. Figure 36a shows one of a series of 10 near-axial, cross-sectional images taken at intervals of 6–7 s. The ^{129}Xe images were obtained with the FLASH pulse sequence (*92*), with pulse tipping angle $\approx 5^\circ$. Despite the relatively low resolution of these preliminary images, the position of the rat's femur can be observed, corresponding to the signal void near the center of the image. The signal remained strong enough to be seen through the final acquisition, 70 s into the experiment. The signal decay was mostly due to the RF observation pulses, with only small contributions from relaxation and xenon wash-out.

More recently, the Duke group has used Intralipid (30%) solutions to deliver polarized xenon to the vasculature of rats, permitting ^{129}Xe MR images to be obtained with significantly improved resolution (*270, 271*). In one study, magnetic resonance angiograms (MRAs) were obtained following separate injections into the tail vein of a laboratory rat. The local blood flow rate was also quantitatively measured in different veins, giving results that agreed well with previous measurements—once the artificial increase caused by the injection was considered. Using polarized xenon injection permitted high-contrast images and measurements to be obtained without background signal, obviating the need for background suppression techniques. A relatively large amount of the polarized xenon/Intralipid solution was injected to perform these studies (5–6 ml in ~10 s delivered to rats weighing ~400–500 g). This amount corresponds to a higher value than what would be practical for future clinical applications in humans (*271*). While this volume and injection rate was well-tolerated by the rats, higher injection rates led to reduced heart rates and subsequent death. However, by using carriers with higher xenon solubilities and improved xenon polarization, it should be possible to perform identical experiments with the same signal-to-noise while using much lower injected volumes.

Finally, by encapsulating microbubbles of laser-polarized ^{3}He gas in an injectable solution, it should be possible to exploit the advantages provided by ^{3}He for use as an MRI tracer (e.g., brighter signal resulting from higher gyromagnetic ratio and greater ease in creating higher nuclear polarization). The promise of this technique was recently demonstrated by

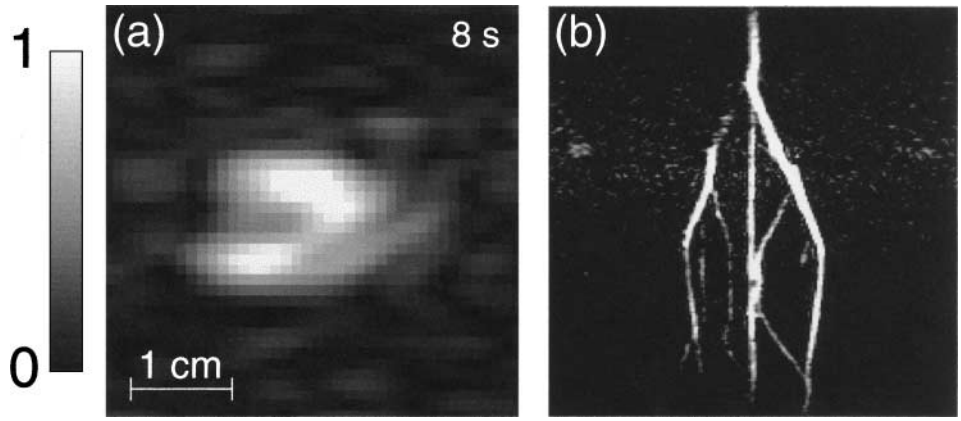

FIG. 36. *In vivo* OPMRI of noble gases obtained following injection of polarized gas carriers. (a) ^{129}Xe MR image selected from a series of images taken following the injection of a laser-polarized xenon/saline solution into the upper hind leg of a living rat (*257*). Image as shown (taken 8 s after injection) was prepared by zero-filling in both dimensions (giving a 256×256 matrix), and 50-Hz Gaussian apodization along the frequency-encoding dimension. Image was acquired using the FLASH method (*92*). The image resolution was approximately 1×5 mm, with a 10-mm slice depth. The signal void near the center of the image corresponds to the rat's femur. (b) High-resolution *in vivo* vascular image taken following intra-arterial injection of a polarized helium microbubble/Hexabrix suspension (*266*). ^{3}He signal was obtained from the abdominal region (showing the abdominal aorta, common iliac arteries, and external iliac arteries). Digital in-plane resolution: 0.31×0.31 mm. Figure courtesy of Mark Chawla and G. Allan Johnson. Reprinted, by permission, from Ref. (*266*), © 1998 National Academy of Sciences, U.S.A.

the injection of a polarized ^{3}He/Hexabrix microbubble solution into the vasculature of rats (*266*). This approach permitted high-resolution images to be obtained following both intraarterial (as shown in Fig. 36b) and intravenous injection. Figure 36b shows laser-polarized ^{3}He signal from the abdominal aorta, common iliac arteries, and external iliac arteries (readers can find a detailed description of the anatomical features of laboratory rats in Ref. (*273*)). Naturally, performing such tissue studies with laser-polarized helium would be extremely difficult using respiration delivery, because the solubility of helium in tissues is 10–100 times lower than that of xenon (*54*). As was the case with the above *in vivo* Intralipid imaging experiments, an impracticably large volume (∼7 ml) of the microbubble suspension was injected to obtain these ^{3}He images. Again, however, increasing the effective helium concentration and polarization should greatly reduce the injected volume necessary to obtain the same excellent signal-to-noise and resolution of the image in Fig. 36. The Duke group has also recently demonstrated *in vivo* ^{3}He OPMRI using injectable solutions containing microspheres filled with polarized helium gas (*267*).

IX. LOW/ZERO-FIELD OPNMR/MRI

A. Introduction

Because the nuclear polarization of laser-polarized noble gases is endowed by the optical pumping process, and not by the external magnetic field, high magnetic fields are not necessary to obtain strong NMR signals or bright magnetic resonance images. Therefore, the nonequilibrium polarization of laser-polarized noble gases can be exploited to perform NMR and MRI experiments at low fields. The intriguing possibility of performing "MRI without the magnet" has attracted increasing interest for a variety of reasons, not the least of which is the fact that the savings obtained by not having to purchase and maintain an MRI magnet well outweighs the cost of the optical pumping equipment. This final section discusses some of the recent work demonstrating the potential of low/zero-field OPNMR/MRI to perform novel experiments of interest in materials science and biomedicine.

B. Conventional Detection

The potential of laser-polarized gases for performing low-field NMR was demonstrated in studies at Princeton investigating the field dependence of ^{129}Xe relaxation in solid laser-polarized xenon (*38*). ^{129}Xe NMR spectra were obtained from samples of frozen laser-polarized xenon at fields as low as 50 G (0.005 T) at 4.2 K, a field roughly a thousand times weaker than what is typically used in conventional magnetic resonance experiments. Optically detected signals from laser-polarized xenon at low field within optical pumping cells were reported about a year later (*274*).

Low-field imaging of polarized noble gases was first demonstrated when 1D MR images were obtained from glass cells containing 0.2–2.5 atm of laser-polarized ^{3}He gas at room temperature and only 31 G (*195*). As described in Section VII, the resolution of these images was sufficient to resolve edge enhancements caused by restricted diffusion of helium at the sample boundaries.

More recently, laser-polarized gases have been used to image the void spaces in human lungs at moderate field strengths, as shown in Fig. 37. In this work, large quantities (∼1 L) of laser-polarized ^{3}He gas were prepared via metastability exchange

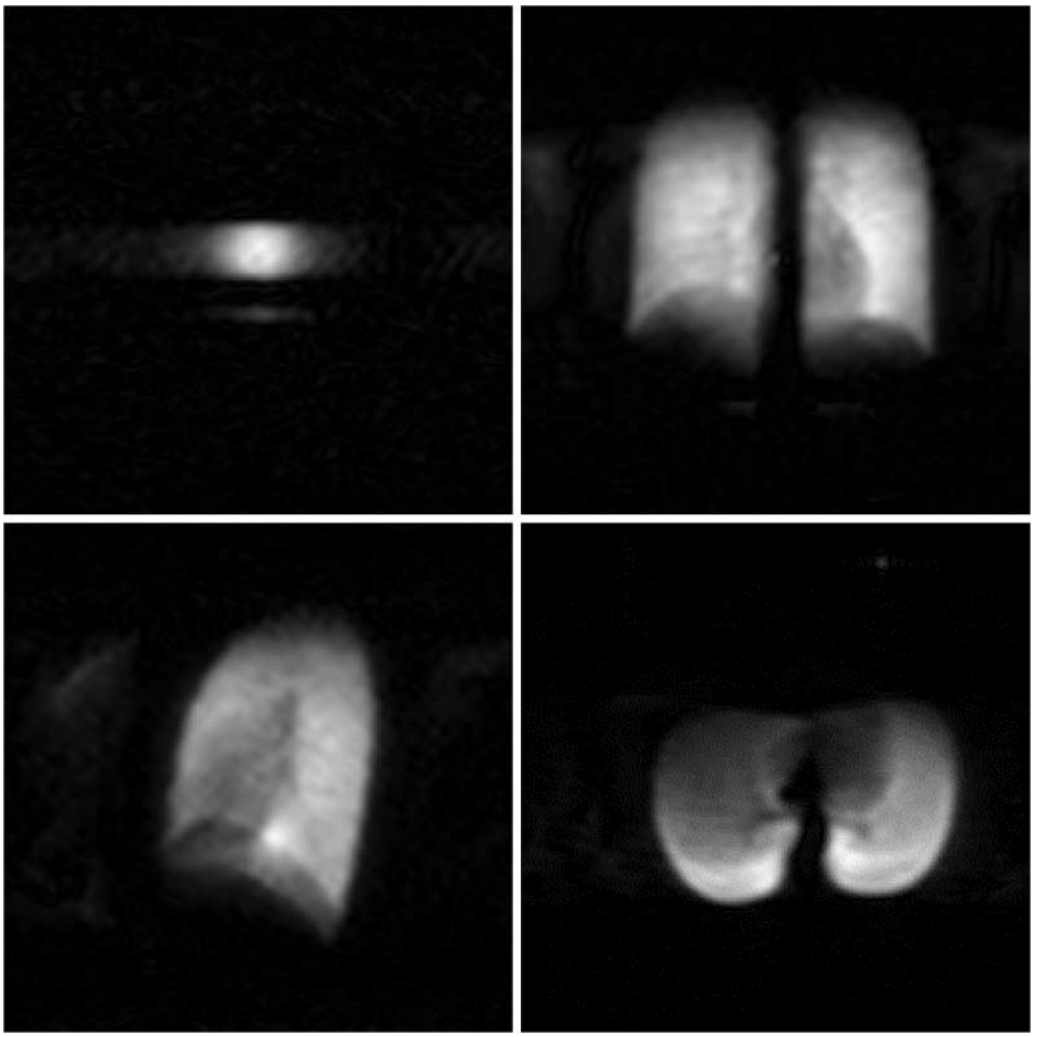

FIG. 37. ^{3}He OP MRI of human lungs at 0.1 T (*276*). Images (clockwise, from upper left): cylindrical (test) cell (5 cm diam.); and lung images through Coronal, Sagittal, and Transverse planes. The blurring artefacts caused by diffusion in the test image are greatly reduced in the lung images (see discussion in previous sections). Figures courtesy of Genevieve Tastevin.

optical pumping. Following respiration of laser-polarized helium by a healthy human volunteer, ^{3}He MR images were obtained from the patient's lungs in a field of only 0.1 T (*275, 276*). This field strength is over an order of magnitude lower than those normally employed in conventional MRI (greatly improving upon the cost and ease of management of the MRI apparatus); nevertheless, there are potential advantages to performing such experiments at fields $\geq$100 times weaker. Specifically, by eliminating the need for strong, enormous magnets to generate nuclear polarization, the cost, comfort, flexibility, safety, and portability of MRI could be greatly improved.

A low-field MRI apparatus was recently built by the Harvard–Smithsonian/MIT collaboration to obtain multidimensional high-resolution images of laser-polarized gases (*93, 277*). A collection of test images obtained with this apparatus is shown in Fig. 38. Specifically, the images in this figure demonstrate an additional advantage of low-field MRI—reduced magnetic susceptibility distortions. Figure 38a shows a high-field (4.7 T) ^{1}H MR image from a water-filled W-shaped cell; Fig. 38b, however, shows the detrimental effect of placing sealed tubes of paramagnetic substances nearby the cell during an otherwise-identical imaging experiment. Figure 38c shows a ^{3}He image obtained at only 21 G by placing a triangle-shaped cell filled with laser-polarized helium gas within the low-field imaging apparatus. Finally, Fig. 38d shows the minimal effect of placing the paramagnetic sample tubes nearby when imaging polarized helium gas at such low fields. Ongoing work using this apparatus has recently produced low-field (20.6 G) images of laser-polarized helium in excised mouse lungs (*93*). The authors of this work suggest an additional future application of such a low-field OPMRI apparatus that some readers may find particularly intriguing: medical diagnoses on space stations.

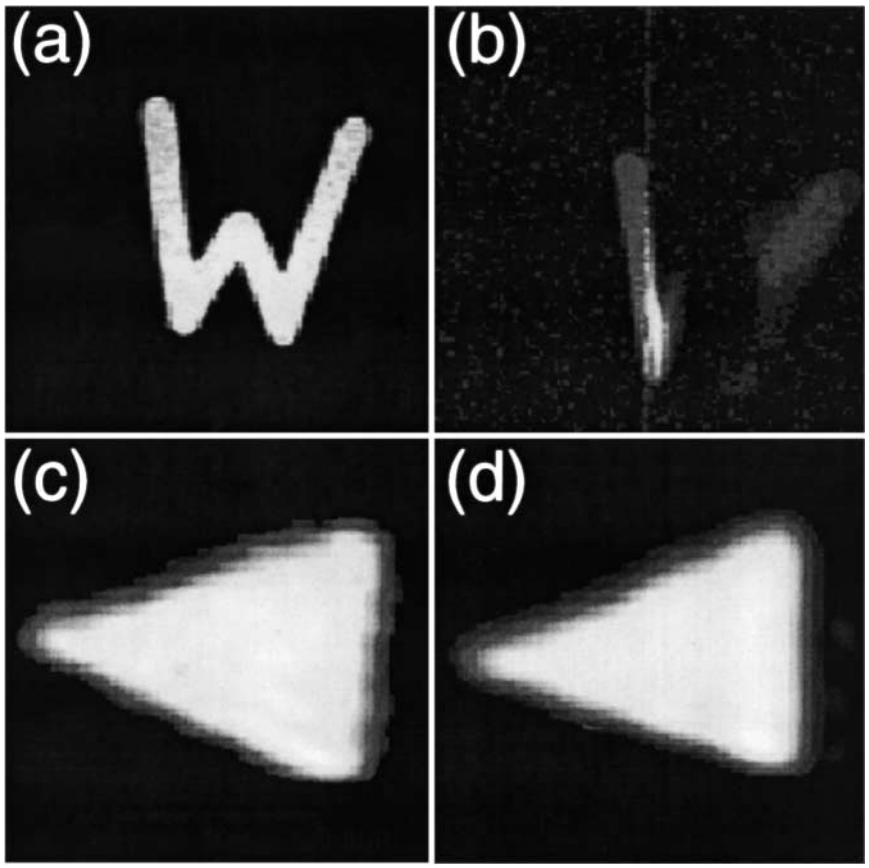

FIG. 38. Demonstration of low-field MRI of polarized gases with greatly reduced magnetic susceptibility distortions (*277*). (a) Room-temperature high-field ^{1}H MR image from a water-filled W-shaped cell. (b) Same as (a), but with paramagnetic materials placed near the cell. (c) Low-field (21 G) ^{3}He MR image from a triangular glass cell containing laser-polarized helium gas. (d) Same as (c), but with the cell placed near the paramagnetic materials. Images were obtained with a standard gradient echo imaging sequence, and the signal was detected with a conventional Faraday induction coil. Figures courtesy of Glenn Wong and Ronald Walsworth.

C. SQUID Detection of Polarized Gases

Conventional detection of nuclear magnetic resonance signals is performed by measuring the voltage induced in a coil by the change in magnetic flux caused by the precession of nuclear spins. For a given sample, the NMR signal detected is proportional to both the polarization and the frequency, i.e., to B_0^2 (if the sample is thermally polarized) or ω_0^2. Thus, the sensitivity of conventional Faraday detectors is highly dependent upon the strength of the external magnetic field; a Faraday detector will be less sensitive when detecting the slower precession of nuclei in weaker magnetic fields.

An alternative approach enabling one to obtain NMR signals at much lower frequencies (and thus much lower fields) employs a super-conducting quantum interference device (SQUID) detector (for a review of SQUID fundamentals and applications, the reader is directed to Ref. (*278*)). While conventional Faraday detectors measure the changes in the oscillating magnetic flux as a function of time ($d\Phi/dt$), a SQUID measures the magnetic flux directly; independent of nuclear polarization, a SQUID's sensitivity does not (in principle) scale with frequency at low frequencies. Thus, SQUIDs may be advantageous for lower-frequency NMR and MRI experiments. Recent work is described below combining SQUID detection with optical pumping to further increase the sensitivity of NMR and MRI of laser-polarized xenon and helium at low magnetic fields.

1. Low-Temperature Experiments

A series of ^{129}Xe NMR spectra are shown in Figs. 39a, 39b taken of frozen laser-polarized xenon at 4.2 K at incrementally lower external magnetic field strengths, permitting the field dependence of the ^{129}Xe T_1 to be studied in great detail (*279*). As shown in the figure, it was possible to obtain ^{129}Xe NMR spectra with Larmor frequencies as low as $\sim$200 Hz, corresponding to a field strength of only 0.19 G (Earth's field, $\sim$0.6 G).

Figure 39c shows a 2D ^{129}Xe MR image of laser-polarized xenon frozen within a Pyrex tube, taken at 4.2 K with an external field of 10 G (corresponding to a Larmor frequency of 11.8 kHz), and with an applied imaging gradient strength of

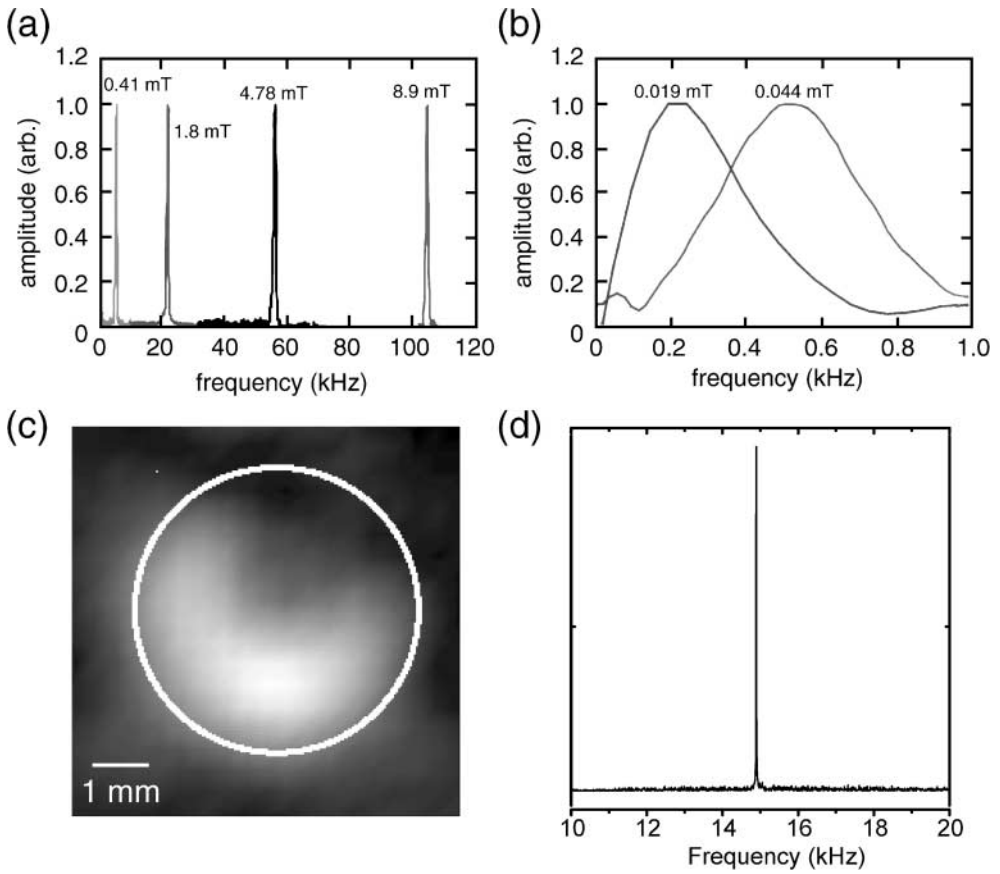

FIG. 39. (a,b) SQUID-detected ^{129}Xe NMR spectra of frozen laser-polarized xenon at 4.2 K obtained with external magnetic field strengths of (a) 0.41, 1.8, 4.78, and 8.9 mT; (b) 0.019 and 0.044 mT (*279*). Figures courtesy of Dinh TonThat. (c) ^{129}Xe MR image taken of laser-polarized xenon frozen to the side of a glass tube immersed in liquid helium (4.2 K) at 10 G (0.001 T) with a low-T_c SQUID (*280*). (d) ^{129}Xe OPNMR from a single scan from laser-polarized xenon gas at 12.6 G; $S:N \sim 100:1$ (*281*). Figures courtesy of Annjoe Wong-Foy.

0.046 T/m (*280*). Because the imaging gradient could be applied in only one direction (due only to technical limitations of the first-generation apparatus), the image in Fig. 39c was obtained by sequentially rotating the cylindrical sample tube along an axis perpendicular to the gradient field, making it possible to reconstruct the distribution of spins in the *xy* plane from the radial sampling and subsequent projection reconstruction. From the figure, it is obvious that xenon was frozen to one side of the sample tube. From the calibrated gradient strength and the known apparent linewidth of frozen xenon without the application of the gradient (520 Hz), the resolution was estimated to be $\sim 1 \times 1$ mm for the 2D image.

2. *Room-Temperature Experiments*

The spectra and images shown in Figs. 39a–39c were obtained with low-T_c SQUID detectors (meaning that the SQUID's threshold for superconduction was only several Kelvin), requiring the sample to be at liquid helium temperatures (4.2 K) in order for the SQUID to remain superconducting. Naturally, this temperature regime prohibits many of the types of experiments that could be performed, particularly ones involving living organisms. However, a high-T_c SQUID detector dewared to permit room-temperature experiments has recently been developed at Berkeley; this apparatus has since been used to obtain room-temperature signals from laser-polarized xenon gas (*281*), as shown in Fig. 39d.

To test the sensitivity of the SQUID detector, samples containing high concentrations of *thermally polarized* protons were also studied; the high sensitivity of the SQUID even permitted the observation of an extremely weak thermal proton signal (signal-to-noise, $\sim 2:1$) from a proton-rich mineral oil sample of 20 G in a single scan (*281*), and could obtain similar signals in thousands of scans at Earth's field. The addition of multidimensional imaging capabilities (i.e., a complete x, y, z gradient set) is under way.

In the future, the combination of laser-polarized xenon delivery with polarization transfer to other nuclei in solution (*36, 91, 103, 124*) and on surfaces (*48, 167*) may be useful for enhancing *their* NMR signals at low fields, thereby permitting

novel magnetic resonance experiments with a variety of potential biomedical and materials science applications.

ACKNOWLEDGMENTS

It is a pleasure to acknowledge Alexander Pines for his guidance, encouragement, and support. The author is grateful for data and figures from the optical pumping NMR/MRI groups at Duke, ENS Paris, Harvard (HSCfA and Brigham and Women's Hospital), Berkeley/LBNL, Michigan, MIT, Princeton, SUNY Stony Brook, and Virginia. The author thanks Thomas Meersmann for helpful discussions. Portions of this work were supported by the Director, Office of Energy Research, Office of Basic Energy Sciences, Materials Sciences Division of the U.S. Department of Energy under Contract DE-AC03-76SF00098.

Note added in proof. One of the primary goals of this review is to provide a reasonably comprehensive survey of NMR spectroscopy and imaging using laser-polarized gases—from the field's inception, up to the present day. As this review was drafted prior to the summer of 2000, more recent contributions have consequently been left out up to this point. However, such recent work has given rise to a number of exciting developments—in the last year alone—that readers of this review should find of particular interest; indeed, such advances include the realization of many predictions described above. Therefore, to direct the interested reader to such recent work, I have briefly summarized below many of the key developments that have been documented since this review was originally completed. Additionally, it is hoped that this summary will help illustrate many of the directions this growing field is taking as we head into the future.

For example, recent polarized gas experiments have permitted novel studies of fundamental behavior (*1*)—including spin relaxation mechanisms (*2–6*)—of polarized xenon and helium under various conditions; novel dynamic studies of hydrate structure (clathrate) formation (*7, 8*); the observation of an enhanced ^{129}Xe CSA signal from a single crystal (silicalite) (*9*); the use of "functionalized" (encapsulated) polarized xenon as a MR biosensor (*10*); the polarization enhancement (via the SPINOE) of solutes dissolved in supercritical laser-polarized xenon (*11*); the selective SPINOE enhancement of NMR signals from xenon-binding molecules in aqueous solutions (*12*), including the first such result for a protein (*13*); and "polarization-enhanced" rudimentary NMR quantum computation (*14*). Also, recent low-field studies have included the demonstration of assignable ^{129}Xe chemical shift measurements using a SQUID at $\sim$2.5 mT (*15*), and the detection of significantly enhanced (up to factors of $\sim$1000 at $\sim$1 mT) proton signals via the SPINOE (*16*).

Other materials-oriented work has used polarized gases to perform enhanced studies of diffusion (*17*) in porous materials (*18, 19*) (including aerogels (*20, 21*)); *in situ* monitoring of the transformation of sorbent functionality in porous materials (*22*); the transfer of polarization from laser-polarized xenon to materials surfaces under OPMAS conditions at ambient (and higher) temperatures (*23*); investigations of the optimal conditions for using polarized xenon under continuous-flow conditions (*24*); the characterization of purified samples of carbon nanotubes (*25*); and the enhanced imaging of diffusion, convection, and flow in void spaces and porous media (*26–28*).

Recent developments in biomedicine include significant improvements in the quality, efficiency, spatiotemporal resolution, and clinical applicability of lung space imaging (see for example, Refs. (*29–40*)); the expansion of polarized gas studies to new target organs (*41, 42*); the investigation of using enhanced xenon NMR spectroscopy to probe tumors following localized injection (*43*); and novel *in vivo* imaging and perfusion studies in the brain (*44–46*) and pulmonary tissue (*47*) using both injection and respiration delivery of laser-polarized xenon and helium.

Additional reviews of biomedical applications of polarized gases can be found in Refs. (*48–50*); biomedically oriented readers should also see the recent special issue of *NMR in Biomedicine* dedicated to MR applications of polarized gases (Vol. 13, 2000). Recent polarized gas MR work of particular relevance to chemistry, biophysics, and materials science will be highlighted in an upcoming review currently under development (*51*). Finally, work continues in the development of improved apparatus for polarizing gases, including a recent report of $>$40% polarization for large-scale production of laser-polarized xenon (*52*).

References: (1) Sauer, K. L., Marion, F., Nacher, P. J., and Tastevin, G. *Phys. Rev. B* **6318**:4427 (2001); (2) Breeze, S. R., Lang, S., Moudrakovski, I., Ratcliffe, C. I., Ripmeester, J. A., Santyr, G., Simard, B., and Zuger, I. *J. Appl. Phys.* **87**:8013–8017 (2000); (3) Moudrakovski, I. L., Breeze, S. R., Simard, B., Ratcliffe, C. I., Ripmeester, J. A., Seideman, T., Tse, J. S., and Santyr, G. *J. Chem. Phys.* **114**:2173–2181 (2001); (4) Fujiwara, H., Kimura, A., Yanagawa, Y., Kamiya, T., Hattori, M., and Hiraga, T. *J. Magn. Reson.* **150**:156–160 (2001); (5) Romalis, M. V., and Ledbetter, M. P. *Phys. Rev. Lett.* **8706**:7601–7604 (2001); (6) Jacob, R. E., Morgan, S. W., Saam, B., and Leawoods J. C. *Phys. Rev. Lett.* **8714**:3004–3007 (2001); (7) Moudrakovski, I. L., Ratcliffe, C. I., and Ripmeester, J. A. *Angew. Chem. Int. Ed. Engl.* **40**:3890–3892 (2001); (8) Moudrakovski, I. L., Sanchez, A. A., Ratcliffe, C. I., and Ripmeester, J. A. *J. Phys. Chem. B* **105**:12338–12347 (2001); (9) Terskikh, V. V., Moudrakovski, I. L., Du, H. B., Ratcliffe, C. I., and Ripmeester, J. A. *J. Am. Chem. Soc.* **123**:10399–10400 (2001); (10) Spence, M. M., Rubin, S. M., Dimitrov, I. E., Ruiz, E. J., Wemmer, D. E., Pines, A, Yao, S. Q., Tian, F., and Schultz, P. G. *Proc. Natl. Acad. Sci. USA* **98**:10654–10657 (2001); (11) Leawoods, J. C., Saam, B. T., and Conradi, M. S. *Chem. Phys. Lett.* **327**:359–364 (2000); (12) Desvaux, H., Gautier, T., Le Goff, G., Petro, M., and Berthault, P. *Eur. Phys. J. D* **12**:289–296 (2000); (13) Landon, C., Berthault, P., Vovelle, F., and Desvaux, H. *Protein Sci.* **10**:762–770 (2001); (14) Verhulst, A. S., Liivak, O., Sherwood, M. H., Vieth, H. M., and Chuang, I. L. *Appl. Phys. Lett.* **79**:2480–2482 (2001); (15) Saxena, S., Wong-Foy, A., Moule, A. J., Seeley, J. A., McDermott, R, Clarke, J, Pines, A. *J. Am. Chem. Soc.* **123**:8133–8134 (2001); (16) Appelt, S., Haesing, F. W., Baer-Lang, S., Shah, N. J., and Blumich, B. *Chem. Phys. Lett.* **348**:263–269 (2001); (17) Wong, G. P., Mair, R. W., Walsworth, R. L., and Cory, D. G. *Phys. Rev. Lett.* **86**:4156–4159 (2001); (18) Meersmann, T., Logan, J. W., Simonutti, R., Caldarelli, S., Comotti, A., Sozzani, P., Kaiser, L. G., and Pines, A. *J. Phys. Chem. B* **104**:11665–11670 (2000); (19) Moudrakovski, I. L., Sanchez, A., Ratcliffe, C. I., and Ripmeester, J. A. *J. Phys. Chem. B* **104**:7306–7310 (2000); (20) Tastevin, G., Nacher, P. J., and Guillot, G. *Physica B* **284**:291–292 (2000); (21) Guillot, G., Nacher, P. J., and Tastevin, G. *Magn. Reson. Imaging* **19**:391–394 (2001); (22) Nossov, A. V., Soldatov, D. V., and Ripmeester, J. A. *J. Am. Chem. Soc.* **123**:3563–3568 (2001); (23) Smith, J., Smith, L. J., Knagge, K., MacNamara, E., and Raftery, D. *J. Am. Chem. Soc.* **123**:2927–2928 (2001); (24) Kneller, J. M., Soto, R. J., Surber, S. E., Colomer, J. F., Fonseca, A., Nagy, J. B., and Pietrass, T. *J. Magn. Reson.* **147**:261–265 (2000); (25) Kneller, J. M., Soto, R. J., Surber, S. E., Colomer, J. F., Fonseca, A., Nagy, J. B., Van Tendeloo, G., and Pietrass, T. *J. Am. Chem. Soc.* **122**:10591–10597 (2000); (26) Mair, R. W., Tseng, C. H., Wong, G. P., Cory, D. G., and Walsworth, R. L. *Phys. Rev. E* **61**:2741–2748 (2000); (27) Kaiser, L. G., Meersmann, T., Logan, J. W., and Pines, A. *Proc. Natl. Acad. Sci. USA* **97**:2414–2418 (2000); (28) Moudrakovski, I. L., Lang, S., Ratcliffe, C. L., Simard, B., Santyr, G., and Ripmeester, J. A. *J. Magn. Reson.* **144**:372–377 2000; (29) Guenther, D., Hanisch, G., and Kauczor, H. U. *Act. Radiol.* **41**:519–528 (2000); (30) Chen, X. J., Hedlund, L. W., Moller, H. E., Chawla, M. S., Maronpot, R. R., and Johnson, G. A. *Proc. Natl. Acad. Sci. USA* **97**:11478–11481 (2000); (31) Ruppert, K., Brookeman, J. R., Hagspiel, K. D., and Mugler, J. P. *Magn. Reson. Med.* **44**:349–357 (2000); (32) Roberts, D. A., Rizi, R. R., Lipson, D. A., Aranda, M., Baumgardner, J., Bearn, L., Hansen-Flaschen, J., Gefter, W. B., Hatabu, H. H., Leigh, J. S., and Schnall, M. D. *Magn. Reson. Med.* **44**:379–382 (2000); (33) Saam, B. T., Yablonskiy, D. A., Kodibagkar, V. D., Leawoods, J. C., Gierada, D. S., Cooper, J. D., Lefrak, S. S., and Conradi, M. S. *Magn. Reson. Med.* **44**:174–179 (2000); (34) Viallon, M., Berthezene, Y., Decorps, M., Wiart, M., Callot, V., Bourgeois, M., Humblot, H., Briguet, A., and Cremillieux, Y. *Magn. Reson. Med.* **44**:1–4 (2000); (35) Schreiber, W. G., Weiler, N., Kauczor, H. U., Markstaller, K., Eberle, B., Hast, J., Surkau, R., Grossmann, T., Deninger, A., Hanisch, G., Otten, E. W., and Thelen, M. *ROFO-Fortschr. Rontg.* **172**:129–133 (2000); (36) Salerno, M., De Lange, E. E., Brookeman, J. R., and Mugler, J. P. *Radiol.* **217**:596 (2000); (37) Salerno, M., Altes, T. A., Brookeman, J. R., de Lange, E. E., and Mugler, J. P. *Magn. Reson. Med.* **46**:667–677 (2001); (38) Altes, T. A., Powers, P. L., Knight-Scott, J., Rakes, G., Platts-Mills, T. A. E., de Lange, E. E., Alford, B. A.,

Mugler, J. P., and Brookeman, J. R. *J. Magn. Reson. Imaging* **13**:378–384 (2001); (39) Zhao, L., Venkatesh, A. K., Albert, M. S., and Panych, L. P., *J. Magn. Reson.* **148**:314–326 (2001); (40) Johnson, G. A., Cofer, G. P., Hedlund, L. W., Maronpot, R. R., and Suddarth, S. A. *Magn. Reson. Med.* **45**:365–370 (2001); (41) Hagspiel, K. D., Altes, T. A., Mugler, J. P., Spellman, M. J., Mata, J. F., Tustison, N. J., and Brookeman, J. R. *Magn. Reson. Med.* **44**:813–816 (2000); (42) Hagspiel, K. D., Altes, T. A., Mugler, J. P., Brookeman, J. R. *J. Magn. Reson. Imaging* **12**:1009–1013 (2000); (43) Wolber, J., McIntyre, D. J. O., Rodrigues, L. M., Carnochan, P., Griffiths, J. R., Leach, M. O., and Bifone, A. *Magn. Reson. Med.* **46**:586–591 (2001); (44) Duhamel, G., Choquet, P., Grillon, E., Lamalle, L., Leviel, J. L., Ziegler, A., and Constantinesco, A. *Magn. Reson. Med.* **46**:208–212 (2001); (45) Duhamel, G., Choquet, P., Grillon, E., Leviel, J. L., Ziegler, A., and Constantinesco, A. *C. R. Acad. Sci. II C* **4**:789–794 (2001); (46) Hong, K. S., Venkatesh, A. K., Kubatina, L. V., Sun, Y., Mulkern, R. V., and Albert, M. S. *Radiol.* **221**:480–480 (2001); (47) Callot, V., Canet, E., Brochot, J., Viallon, M., Humblot, H., Briguet, A., Tournier, H., and Cremillieux, Y. *Magn. Reson. Med.* **46**:535–540 (2001); (48) Kauczor, H. U., and Kreitner, K. F. *Eur. J. Radiol.* **34**:196–207 (2000); (49) Salerno, M., Altes, T. A., Mugler, J. P., Nakatsu, M., Hatabu, H., and de Lange, E. E. *Eur. J. Radiol.* **40**:33–44 (2001); (50) Chupp, T., and Swanson, S. *Adv. Atom. Mol. Opt. Phys.* **45**:41 (2001); (51) Goodson, B. M., Spence, M. M., and Logan, J., Manuscript in preparation. (52) Zook, A. L., and Bowers, C. R. *NHMFL Reports*, Fall (2001).

REFERENCES

1. B. M. Goodson, Ph.D. thesis, University of California, Berkeley, 1999.
2. B. M. Goodson, L. Kaiser, and A. Pines, *in* "Proceedings of the International School of Physics, Enrico Fermi" (B. Maraviglia, Ed.), 1999.
3. A. Abragam, "Principles of Nuclear Magnetism," Oxford (1961).
4. M. Mehring, "High Resolution NMR Spectroscopy in Solids," 2nd ed., Springer-Verlag, Berlin, 1983.
5. R. R. Ernst, G. Bodenhausen, and A. Wokaun, "Principles of Nuclear Magnetic Resonance in One and Two Dimensions," Oxford (1994).
6. L. Emsley and A. Pines, *in* "Proceedings of the International School of Physics, Enrico Fermi" (B. Maraviglia, Ed.), 1994.
7. C. P. Slichter, "Principles of Magnetic Resonance," 3rd ed., Springer-Verlag, Berlin (1996).
8. P. T. Callaghan, "Principles of Nuclear Magnetic Resonance Microscopy," Oxford (1991).
9. Y. Xia, *Concepts Magn. Reson.* **8,** 205–225 (1996).
10. F. W. Wehrli, *Prog. NMR Spectrosc.* **28,** 87–135 (1995).
11. W. S. Price, *Annu. Rep. NMR Spectrosc.* **35,** 140–191 (1998).
12. B. M. Goodson, *Concepts Magn. Reson.* **11,** 203–223 (1999).
13. R. A. Bernheim, "Optical Pumping: An Introduction," Benjamin, New York (1965).
14. J. Brossel and A. Kastler, *Compt. Rend.* **229,** 1213–1215 (1949).
15. A. Kastler, *J. Phys. Radium.* **11,** 255–265 (1950).
16. A. Kastler, *J. Opt. Soc. Am.* **47,** 460–165 (1957).
17. M. R. Bouchiat, T. R. Carver, and C. M. Varnum, *Phys. Rev. Lett.* **5,** 373–375 (1960).
18. B. C. Grover, *Phys. Rev. Lett.* **40,** 391 (1978).
19. N. D. Bhaskar, W. Happer, and T. McClelland, *Phys. Rev. Lett.* **49,** 25 (1982).
20. W. Happer, E. Miron, S. Schaefer, D. Schreiber, W. A. van Wijngaarden, and X. Zeng, *Phys. Rev. A* **29,** 3092–3110 (1984).
21. T. G. Walker and W. Happer, *Rev. Mod. Phys.* **69,** 629–642 (1997).
22. F. D. Colegrove, L. D. Schearer, and G. K. Walters, *Phys. Rev.* **132,** 2561–2572 (1963).
23. G. Eckert, W. Heil, M. Meyerhoff, E. W. Otten, R. Surkau, M. Werner, M. Leduc, P. J. Nacher, and L. D. Schearer, *Nucl. Instrum. Methods. Phys. Res. A* **320,** 53–65 (1992).
24. E. Stolz, M. Meyerhoff, N. Bigelow, M. Leduc, P. J. Nacher, and G. Tastevin, *Appl. Phys. B* **63,** 629–633 (1996).
25. J. Becker, J. Bermuth, M. Ebert, T. Grossmann, W. Heil, D. Hofmann, H. Humblot, M. Leduc, E. W. Otten, D. Rohe, and R. Surkau, *Nucl. Instrum. Methods. Phys. Res. A* **402,** 327–336 (1998).
26. R. Tycko and J. A. Reimer, *J. Phys. Chem.* **100,** 13240–13250 (1996).
27. S. E. Barrett, G. Dabbagh, L. N. Pfeiffer, K. W. West, and R. Tycko, *Semicond. Sci. Tech.* **11,** 1488–1492 (1996).
28. R. Tycko, *Solid State Nucl. Magn. Reson.* **11,** 1–9 (1998).
29. G. Frossati, *J. Low Temp. Phys.* **111,** 521–532 (1998).
30. G. Frossati, *Nucl. Instrum. Methods. Phys. Res. A* **402,** 479–483 (1998).
31. M. E. Wagshul and T. E. Chupp, *Phys. Rev. A* **40,** 4447–4454 (1989).
32. E. Brunner, *Concepts Magn. Reson.* **11,** 313–335 (1999).
33. B. T. Saam and M. S. Conradi, *J. Magn. Reson.* **134,** 67–71 (1998).
34. T. R. Gentile, G. L. Jones, A. K. Thompson, R. R. Rizi, D. A. Roberts, I. E. Dimitrov, R. Reddy, D. A. Lipson, W. Gefter, M. D. Schnall, and J. S. Leigh, *Magn. Reson. Med.* **43,** 290–294 (2000).
35. D. Raftery, H. Long, T. Meersmann, P. J. Grandinetti, L. Reven, and A. Pines, *Phys. Rev. Lett.* **66,** 584–587 (1991).
36. M. Luhmer, B. M. Goodson, Y.-Q. Song, D. D. Laws, L. Kaiser, M. C. Cyrier, and A. Pines, *J. Am. Chem. Soc.* **121,** 3502–3512 (1999).
37. T. Pietraß and H. C. Gaede, *Adv. Mat.* **7,** 826–838 (1995).
38. M. Gatzke, G. D. Cates, B. Driehuys, D. Fox, W. Happer, and B. Saam, *Phys. Rev. Lett.* **70,** 690–693 (1993).
39. G. D. Cates, D. R. Benton, M. Gatzke, W. Happer, K. C. Hasson, and N. R. Newbury, *Phys. Rev. Lett.* **65,** 2591–2594 (1990).
40. X. Z. Zeng, C. J. Wu, M. X. Zhao, S. L. Li, L. Y. Li, X. T. Zhang, Z. D. Liu, and W. Y. Liu, *Chem. Phys. Lett.* **182,** 538–540 (1991).
41. Z. Liu, M. Zhao, C. Wu, L. Li, S. Li, X. Zeng, and W. Xiong, *Chem. Phys. Lett.* **194,** 440–445 (1992).
42. M. P. Augustine and K. W. Zilm, *J. Chem. Phys.* **105,** 2998–3011 (1996).
43. M. P. Augustine and K. W. Zilm, *Mol. Phys.* **89,** 737–752 (1996).
44. M. P. Augustine and K. W. Zilm, *Chem. Phys. Lett.* **280,** 24–30 (1997).
45. H. J. Jänsch, T. Hof, U. Ruth, J. Schmidt, D. Stahl, and D. Fick, *Chem. Phys. Lett.* **296,** 146–150 (1998).
46. U. Ruth, T. Hof, J. Schmidt, D. Fick, and H. J. Jänsch, *Appl. Phys. B* **68,** 93–97 (1999).
47. B. Driehuys, G. D. Cates, E. Miron, K. Sauer, D. K. Walter, and W. Happer, *Appl. Phys. Lett.* **69,** 1668–1670 (1996).
48. M. Haake, A. Pines, J. A. Reimer, and R. Seydoux, *J. Am. Chem. Soc.* **119,** 11711–11712 (1997).
49. R. Seydoux, M. Haake, A. Pines, and J. A. Reimer, *J. Phys. Chem. B* **103,** 4629–4637 (1999).
50. J. N. Zerger, M. J. Lim, K. P. Coulter, and T. E. Chupp, *Appl. Phys. Lett.* **76,** 1798–1800 (2000).
51. M. S. Rosen, T. E. Chupp, K. P. Coulter, R. C. Welsh, and S. D. Swanson, *Rev. Sci. Instrum.* **70,** 1546–1552 (1999).
52. M. Poliakoff, S. M. Howdle, and S. G. Kazarian, *Angew. Chem.* **34,** 1275–1295 (1995).
53. M. Haake, B. M. Goodson, D. D. Laws, E. Brunner, M. C. Cyrier, R. H. Havlin, and A. Pines, *Chem. Phys. Lett.* **292,** 686–690 (1998).
54. P. K. Weathersby and L. D. Homer, *Undersea Biomed. Res.* **7,** 277–296 (1980).
55. S. C. Cullen and E. G. Gross, *Science* **113,** 580–582 (1951).
56. R. R. Kennedy, J. W. Stokes, and P. Downing, *Anaesth. Intens. Care* **20,** 66–70 (1992).

57. M. S. Albert and D. Balamore, *Nucl. Instrum. Methods. Phys. Res. A* **402,** 441–453 (1998).
58. A. M. Bidabé, D. G. de Beaufort, A. M. Gin, and J. M. Caillé, *J. Neuroradiol.* **17,** 103–124 (1990).
59. D. M. Schmidt, J. S. George, S. I. Penttila, A. Caprihan, and E. Fukushima, *J. Magn. Reson.* **129,** 184–187 (1997).
60. P. W. E. Peereboom, H. Luigjes, and K. O. Prins, *Phys. A* **156,** 260–276 (1989).
61. M. Bock, *Magn. Reson. Med.* **38,** 890–895 (1997).
62. R. W. Mair, D. G. Cory, S. Peled, C.-H. Tseng, S. Patz, and R. L. Walsworth, *J. Magn. Reson.* **135,** 478–486 (1998).
63. S. Peled, C.-H. Tseng, A. A. Sodickson, R. W. Mair, R. Walsworth, and D. G. Cory, *J. Magn. Reson.* **140,** 320–324 (1999).
64. R. W. Mair, G. P. Wong, D. Hoffmann, M. D. Hurlimann, S. Patz, L. M. Schwartz, and R. L. Walsworth, *Phys. Rev. Lett.* **83,** 3324–3327 (1999).
65. G. R. Davies, T. K. Halstead, R. C. Greenhow, and K. J. Packer, *Chem. Phys. Lett.* **230,** 237–242 (1994).
66. B. R. Patyal, J.-H. Gao, R. H. Williams, J. Roby, B. Saam, B. A. Rockwell, R. J. Thomas, D. J. Stolarski, and P. T. Fox, *J. Magn. Reson.* **126,** 58–65 (1997).
67. D. Raftery and B. Chmelka, *in* "NMR Basic Principles and Progress" (P. Diehl, E. Fluck, H. Günther, R. Kosfeld, and J. Seelig, Eds.), Vol. 30, pp. 111–158, Springer-Verlag, Berlin (1994).
68. C. I. Ratcliffe, *Ann. Rep. NMR Spectrosc.* **36,** 124–208 (1998).
69. Y.-Q. Song, B. M. Goodson, and A. Pines, *Spectroscopy* **14,** 26–33 (1999).
70. T. Pietraß, *Colloid Surface A* **158,** 51–57 (1999).
71. J. P. Mugler, III, P. L. Bogorad, B. Driehuys, and J. R. Brookeman, *J. Magn. Reson. Anal.*, in press.
72. E. R. Hunt and H. Y. Carr, *Phys. Rev.* **130,** 2306 (1963).
73. X. Zeng, E. Miron, W. A. van Wijngaarden, D. Schreiber, and W. Happer, *Phys. Lett. A* **96,** 191 (1983).
74. B. Driehuys, G. D. Cates, and W. Happer, *Phys. Rev. Lett.* **74,** 4943–4946 (1995).
75. M. A. Bouchiat and J. Brossel, *Phys. Rev.* **147,** 41 (1966).
76. S. R. Breeze, S. Lang, I. Moudrakovski, C. I. Ratcliffe, J. A. Ripmeester, B. Simard, and G. Santyr, *J. Appl. Phys.* **86,** 4040–4042 (1999).
77. R. L. Streever and H. Y. Carr, *Phys. Rev.* **121,** 20–25 (1961).
78. C. J. Jameson, A. K. Jameson, and S. M. Cohen, *J. Chem. Phys.* **59,** 4540–4546 (1973).
79. K. W. Miller, N. V. Reo, A. J. M. S. Uiterkamp, D. P. Stengle, T. R. Stengle, and K. L. Williamson, *Proc. Natl. Acad. Sci. U.S.A.* **78,** 4946–4949 (1981).
80. J. Fraissard and T. Ito, *Zeolites* **8,** 350–361 (1988).
81. P. J. Barrie and J. Klinowski, *Prog. NMR Spectrosc.* **24,** 91–108 (1992).
82. J. Jokisaari, *Prog. NMR. Spectrosc.* **26,** 1–26 (1994).
83. C. Dybowski and N. Bansal, *Annu. Rev. Phys. Chem.* **42,** 433–464 (1991).
84. J. L. Bonardet, J. Fraissard, A. Gedeon, and M. A. Springuel-Huet, *Catal. Rev.* **41,** 115–225 (1999).
85. J. Sandström, "Dynamic NMR Spectroscopy," Academic Press, London (1982).
86. R. F. Tilton, Jr. and I. D. Kuntz, Jr., *Biochemistry* **21,** 6850–6857 (1982).
87. L. Zhao and M. S. Albert, *Nucl. Instrum. Methods. Phys. Res. A* **402,** 454–460 (1998).
88. L. Zhao, R. Mulkern, C.-H. Tseng, D. Williamson, S. Patz, R. Kraft, R. L. Walsworth, F. A. Jolesz, and M. S. Albert, *J. Magn. Reson. B* **113,** 179–183 (1996).
89. J. Wolber, S. J. Doran, M. O. Leach, and A. Bifone, *Chem. Phys. Lett.* **296,** 391–396 (1998).
90. P. Berthault, H. Desvaux, G. Le Goff, and M. Petro, *Chem. Phys. Lett.* **314,** 52–56 (1999).
91. Y.-Q. Song, B. M. Goodson, R. E. Taylor, D. D. Laws, G. Navon, and A. Pines, *Angew. Chem., Intl. Ed. Engl.* **36,** 2368–2370 (1997).
92. A. Haase, J. Frahm, D. Matthaei, W. Hanicke, and K. D. Merboldt, *J. Magn. Reson.* **67,** 258–266 (1986).
93. G. P. Wong, C. H. Tseng, V. R. Pomeroy, R. W. Mair, D. P. Hinton, D. Hoffmann, R. E. Stoner, F. W. Hersman, D. G. Cory, and R. L. Walsworth, *J. Magn. Reson.* **141,** 217–227 (1999).
94. M. Garwood and Y. Ke, *J. Magn. Reson.* **94,** 511–525 (1991).
95. T. L. Hwang, P. C. M. van Zijl, and M. Garwood, *J. Magn. Reson.* **133,** 200–203 (1998).
96. C. R. Bowers, H. W. Long, T. Pietraß, H. C. Gaede, and A. Pines, *Chem. Phys. Lett.* **205,** 168–170 (1993).
97. B. Driehuys, G. D. Cates, W. Happer, H. Mabuchi, B. Saam, M. S. Albert, and A. Wishnia, *Phys. Lett. A* **184,** 88–92 (1993).
98. S. R. Hartmann and E. L. Hahn, *Phys. Rev.* **128,** 2042 (1962).
99. A. Pines, M. G. Gibby, and J. S. Waugh, *J. Chem. Phys.* **56,** 1776–1777 (1972).
100. A. Pines, M. G. Gibby, and J. S. Waugh, *J. Chem. Phys.* **59,** 569–590 (1973).
101. H. W. Long, H. C. Gaede, J. Shore, L. Reven, C. R. Bowers, J. Kritzenberger, T. Pietraß, A. Pines, P. Tang, and J. A. Reimer, *J. Am. Chem. Soc.* **115,** 8491–8492 (1993).
102. H. C. Gaede, Y.-Q. Song, R. E. Taylor, E. J. Munson, J. A. Reimer, and A. Pines, *Appl. Magn. Reson.* **8,** 373–384 (1995).
103. G. Navon, Y.-Q. Song, T. Rõõm, S. Appelt, R. E. Taylor, and A. Pines, *Science* **271,** 1848–1851 (1996).
104. A. W. Overhauser, *Phys. Rev.* **92,** 411–415 (1953).
105. T. R. Carver and C. P. Slichter, *Phys. Rev.* **92,** 212–213 (1953).
106. I. Solomon, *Phys. Rev.* **99,** 559–565 (1955).
107. J. H. Noggle and R. E. Shirmer, "The Nuclear Overhauser Effect: Chemical Applications," Academic Press, New York/London (1971).
108. D. Neuhaus and M. P. Williamson, "The Nuclear Overhauser Effect in Structural and Conformational Analysis," VCH, New York/Cambridge (1989).
109. J. Cavanagh, W. J. Fairbrother, A. G. Palmer, and N. J. Skelton, "Protein NMR Spectroscopy: Principles and Practice," Academic Press, San Diego (1996).
110. Y.-Q. Song, *Concepts Magn. Reson.* **12,** 6–20 (2000).
111. M. Luhmer, A. Moschos, and J. Reisse, *J. Magn. Reson. A* **113,** 164–168 (1995).
112. M. Luhmer and J. Reisse, *Prog. Nucl. Magn. Reson. Spectrosc.* **33,** 57–76 (1998).
113. J. Stonehouse, P. Adell, J. Keeler, and A. J. Shaka, *J. Am. Chem. Soc.* **116,** 6037–6038 (1994).
114. K. Stott, J. Keeler, Q. N. Van, and A. J. Shaka, *J. Magn. Reson.* **125,** 302–324 (1997).
115. P. M. Rentzepis and D. C. Douglass, *Nature* **293,** 165–166 (1981).
116. M. B. Sponsler, B. H. Weiller, P. O. Stoutland, and R. G. Bergman, *J. Am. Chem. Soc.* **111,** 6841–6843 (1989).
117. L. D. Field, A. V. George, B. A. Messerle, and H. Ionn, *Anal. Chem.* **63,** 184–186 (1991).
118. P. E. Savage, S. Gopalan, T. I. Mizan, C. J. Martino, and E. E. Brock, *AIChE J.* **41,** 1723–1778 (1995).
119. S. M. Howdle, M. Jobling, and M. Poliakoff *ACS Sympos. Ser.* **488,** 121–131 (1992).
120. H. Destaillats and R. Fernndez-Prini, *J. Chem. Thermod.* **29,** 1209–1221 (1997).
121. K. L. Sauer, R. J. Fitzgerald, and W. Happer, *Chem. Phys. Lett.* **277,** 153–158 (1997).

122. M. Haake, R. Seydoux, J. A. Reimer, and A. Pines, *in* "39th Rocky Mountain Conference on Analytical Chemistry, Denver, CO, 1997."

123. C. H. Tseng, R. W. Mair, G. P. Wong, D. Williamson, D. G. Cory, and R. L. Walsworth, *Phys. Rev. E* **59,** 1785–1789 (1999).

124. R. J. Fitzgerald, K. L. Sauer, and W. Happer, *Chem. Phys. Lett.* **284,** 87–92 (1998).

125. S. Ikawa and Y. Fujita, *J. Phys. Chem.* **97,** 10607–10612 (1993).

126. E. Castillo, A. Marty, D. Combes, and J. S. Condoret, *Biotech. Lett.* **16,** 169–174 (1994).

127. I. T. Horvath and J. M. Millar, *Chem. Rev.* **91,** 1339–1351 (1991).

128. J. W. Rathke, R. J. Klingler, and T. R. Krause, *Organometallics* **10,** 1350–1355 (1991).

129. J. W. Rathke, R. J. Klingler, and T. R. Krause, *Organometallics* **11,** 585–588 (1992).

130. F. Okada and V. A. Apkarian, *J. Chem. Phys.* **94,** 133–144 (1991).

131. E. R. Hunt and H. Y. Carr, *Phys. Rev.* **130,** 2302–2305 (1963).

132. B. P. Schoenborn, H. C. Watson, and J. C. Kendrew, *Nature* **207,** 28–30 (1965).

133. B. P. Schoenborn, *Nature* **208,** 760–762 (1965).

134. R. F. Tilton, Jr., I. D. Kuntz, Jr., and G. A. Petsko, *Biochemistry* **23,** 2849–2857 (1984).

135. S. McKim and J. F. Hinton, *Biochim. Biophys. Acta* **1193,** 186–198 (1994).

136. M. Shlitz, T. Prangé, and R. Fourme, *J. Appl. Crystallogr.* **27,** 950–960 (1994).

137. M. Shlitz, R. Fourme, I. Broutin, and T. Prangé, *Structure* **3,** 309–316 (1995).

138. T. Prangé, M. Shlitz, L. Pernot, N. Colloc'h, S. Longhi, W. Bourget, and R. Fourme, *Prot. Struc. Funct.* **30,** 61–73 (1998).

139. J. Wolber, A. Cherubini, A. S. K. Dzik-Jurasz, M. O. Leach, and A. Bifone, *Proc. Natl. Acad. Sci. U.S.A.* **96,** 3664–3669 (1999).

140. J. A. Ripmeester, C. I. Ratcliffe, and J. S. Tse, *J. Chem. Soc. Faraday Trans. 1* **84,** 3731–3745 (1988).

141. T. Pietraß, H. C. Gaede, A. Bifone, A. Pines, and J. A. Ripmeester, *J. Am. Chem. Soc.* **117,** 7520–7525 (1995).

142. Y. Xu and P. Tang, *Biochim. Biophys. Acta* **1323,** 154–162 (1997).

143. D. J. Cram, M. E. Tanner, and C. B. Knobler, *J. Am. Chem. Soc.* **113,** 7717–7727 (1991).

144. T. A. Robbins, C. B. Knobler, D. R. Bellew, and D. J. Cram, *J. Am. Chem. Soc.* **116,** 111–122 (1994).

145. N. Branda, R. M. Grotzfeld, C. Valdés, and J. Rebek, Jr., *J. Am. Chem. Soc.* **117,** 85–88 (1995).

146. K. Bartik, M. Luhmer, S. J. Heyes, R. Ottinger, and J. Reisse, *J. Magn. Reson. B* **109,** 164–168 (1995).

147. E. B. Brouer, J. Enright, and J. A. Ripmeester, *Chem. Commun.* 939–940 (1997).

148. T. K. Hitchens and R. G. Bryant, *J. Magn. Reson.* **124,** 227 (1997).

149. K. Bartik, M. Luhmer, J.-P. Dutasta, A. Collet, and J. Reisse, *J. Am. Chem. Soc.* **120,** 784–791 (1998).

150. P. Seeman, *Pharmacol. Rev.* **24,** 583–655 (1972).

151. K. W. Miller, *Int. Rev. Neurobiol.* **27,** 1–61 (1985).

152. N. P. Franks and W. R. Leib, *Trends Pharmacol. Sci.* **8,** 169–174 (1987).

153. N. P. Franks and W. R. Leib, *Nature* **367,** 607–614 (1994).

154. J. Szejtli, "Cyclodextrin Technology," Kluwer Academic, Dordrecht (1988).

155. F. C. Cramer and F. M. Henglein, *Chem. Ber.* **90,** 2561–2571 (1957).

156. F. C. Cramer and F. M. Henglein, *Chem. Ber.* **90,** 2572–2575 (1957).

157. A. Stith, T. K. Hitchens, D. P. Hinton, S. S. Berr, B. Driehuys, J. R. Brookeman, and R. G. Bryant, *J. Magn. Reson.* **139,** 225–231 (1999).

158. W. Saenger and M. Noltenmeyer *Angew. Chem.* **13,** 552–553 (1974).

159. P. D. Kirchhoff, M. B. Bass, B. A. Hanks, J. M. Briggs, A. Collet, and J. A. McCammon, *J. Am. Chem. Soc.* **118,** 3237–3246 (1996).

160. C. R. Bowers, V. Storhaug, C. E. Webster, J. Bharatam, A. Cottone III, R. Gianna, K. Betsey, and B. J. Gaffney, *J. Am. Chem. Soc.* **121,** 9370–9377 (1999).

161. S. M. Rubin, M. M. Spence, B. M. Goodson, D. Wemmer, and A. Pines, *Proc. Natl. Acad. Sci.* USA **97,** 9472–9475 (2000).

162. P. A. Jennings, M. J. Stone, and P. E. Wright, *J. Biomol. NMR* **6,** 271–276 (1995).

163. M. Luhmer, personal communication.

164. C. R. Bowers, J. Bharatam, V. Storhaug, C. E. Webster, A. Cottone, R. Gianna, and B. J. Gaffney, *Biophys. J. A* **76,** 136 (1999).

165. D. Raftery, H. Long, L. Reven, P. Tang, and A. Pines, *Chem. Phys. Lett.* **191,** 385–390 (1992).

166. D. Raftery, L. Reven, H. Long, A. Pines, P. Tang, and J. A. Reimer, *J. Phys. Chem.* **97,** 1649–1655 (1993).

167. T. Rõõm, S. Appelt, R. Seydoux, A. Pines, and E. L. Hahn, *Phys. Rev. B* **55,** 11604–11610 (1997).

168. T. Pietraß, R. Seydoux, and A. Pines, *J. Magn. Reson.* **133,** 299–303 (1998).

169. D. Raftery, E. MacNamara, G. Fisher, C. V. Rice, and J. Smith, *J. Am. Chem. Soc.* **119,** 8746–8747 (1997).

170. E. Brunner, *Magn. Reson. Chem.* **314,** 52–56 (1999).

171. P. Sozzani, A. Comotti, R. Simonutti, T. Meersmann, J. W. Logan, and A. Pines, *Angew. Chem., Intl. Ed. Engl.* **39,** 2695–2698 (2000).

172. M. A. Springuel-Huet and J. Fraissard, *Chem. Phys. Lett.* **154,** 299–302 (1989).

173. J. A. Ripmeester and C. I. Ratcliffe, *J. Chem. Phys.* **99,** 619–622 (1995).

174. E. Brunner, R. Seydoux, M. Haake, A. Pines, and J. A. Reimer, *J. Magn. Reson.* **130,** 145–148 (1998).

175. E. Brunner, M. Haake, A. Pines, J. A. Reimer, and R. Seydoux, *Chem. Phys. Lett.* **290,** 112–116 (1998).

176. E. MacNamara, G. Fisher, J. Smith, C. V. Rice, S. J. Hwang, and D. Raftery, *J. Phys. Chem. B* **103,** 1158–1160 (1999).

177. R. D. Johnson, C. S. Yannoni, H. C. Dorn, J. R. Salem, and D. S. Bethune, *Science* **255,** 1235–1238 (1992).

178. R. Tycko, G. Dabbagh, R. M. Fleming, R. C. Haddon, A. V. Makhija, and S. M. Zahurak, *Phys. Rev. Lett.* **67,** 1886–1889 (1991).

179. R. Tycko, G. Dabbagh, G. M. B. Vaughan, P. A. Heiney, R. M. Strongin, M. A. Cichy, and A. B. Smith, III, *J. Chem. Phys.* **99,** 7554–7564 (1993).

180. R. Blinc, J. Seliger, J. Dolinšek, and D. Arčon, *Phys. Rev. B* **49,** 4993–5002 (1994).

181. E. MacNamera, C. V. Rice, J. Smith, L. J. Smith, and D. Raftery, *Chem. Phys. Lett.* **317,** 165–173 (2000).

182. D. M. Gregory, R. E. Gerald, II, and R. E. Botto, *J. Magn. Reson.* **131,** 327–335 (1998).

183. M. S. Albert, G. D. Cates, B. Driehuys, W. Happer, B. Saam, C. S. Springer, Jr., and A. Wishnia, *Nature* **370,** 199–201 (1994).

184. H. Middleton, R. D. Black, B. Saam, G. D. Cates, C. P. Cofer, R. Guenther, W. Happer, L. W. Hedlund, G. A. Johnson, K. Juvan, and J. Swartz, *Magn. Reson. Med.* **33,** 271–275 (1995).

185. Y.-Q. Song, H. C. Gaede, T. Pietraß, G. A. Barrall, G. C. Chingas, M. R. Ayers, and A. Pines, *J. Magn. Reson. A* **115,** 127–130 (1995).

186. Y.-Q. Song, R. E. Taylor, and A. Pines, *Solid State Nucl. Magn. Reson.* **10,** 247–250 (1998).

187. R. W. Mair, C. H. Tseng, G. P. Wong, D. G. Cory, and R. L. Walsworth, *Phys. Rev. E* **61,** 2741–2748 (2000).

188. W. B. Hyslop and P. C. Lauterbur, *J. Magn. Reson.* **94,** 501–510 (1991).

189. B. Putz, D. Barsky, and K. Schulten, *J. Magn. Reson.* **97,** 27–53 (1992).

190. D. Barsky, B. Putz, K. Schulten, J. Schoeniger, E. W. Hsu, and S. Blackband, *Chem. Phys. Lett.* **200,** 88–96 (1992).

191. P. T. Callaghan, A. Coy, L. C. Forde, and C. J. Rofe, *J. Magn. Reson. A* **101,** 347–350 (1993).

192. S. D. Stoller, W. Happer, and F. J. Dyson, *Phys. Rev. A* **44,** 7459–7477 (1991).

193. T. M. de Swiet and P. N. Sen, *J. Chem. Phys.* **100,** 5597–5604 (1994).

194. T. M. de Swiet, *J. Magn. Reson. B* **109,** 12–18 (1995).

195. B. Saam, N. Drukker, and W. Happer, *Chem. Phys. Lett.* **263,** 481–487 (1996).

196. Y.-Q. Song, B. M. Goodson, B. Sheridan, T. M. de Swiet, and A. Pines, *J. Chem. Phys.* **108,** 6233–6239 (1998).

197. J. Karger and W. Heink, *J. Magn. Reson.* **51,** 1 (1983).

198. R. E. Taylor, Y.-Q. Song, T. Rõõm, S. Appelt, R. Seydoux A. Bifone, D. de Graw, B. Goodson, D. Laws, and A. Pines, *in* "37th Experimental Nuclear Magnetic Resonance Conference, Pacific Grove, CA, 1996."

199. D. Le Bihan, E. Breton, D. Lallemand, P. Grenier, E. Cabanis, and M. Laval-Jeantet, *Radiology* **161,** 401 (1986).

200. R. Turner and D. Le Bihan, *J. Magn. Reson.* **86,** 445–452 (1990).

201. E. Brunner, M. Haake, L. Kaiser, A. Pines, and J. A. Reimer, *J. Magn. Reson.* **138,** 155–159 (1999).

202. P. T. Callaghan, C. D. Eccles, and Y. Xia, *J. Phys. E* **21,** 820–822 (1988).

203. A. E. Sheidegger, "The Physics of Flow Through Porous Media," Macmillan, New York (1957).

204. I. F. Golubev, "Viscosity of Gases and Gas Mixtures," translation, Israel Program for Scientific Translation, Jerusalem, 1970.

205. L. G. Kaiser, T. Meersmann, J. W. Logan, and A. Pines, *Proc. Natl. Acad. Sci. U.S.A.* **97,** 2414–2418 (2000).

206. B. T. Saam, *Nat. Med.* **2,** 358–359 (1996).

207. A. Constantinesco, P. Choquet, M. Wioland, M. Leduc, P. J. Nacher, and G. Tastevin, *Med. Nucl.* **21,** 285–292 (1997).

208. M. Leduc, P. J. Nacher, and G. Tastevin, *Laser Phys.* **8,** 799–802 (1998).

209. H. U. Kauczor, R. Surkau, and T. Roberts, *Eur. Radiol.* **8,** 820–827 (1998).

210. H. E. Moller, X. J. Chen, M. S. Chawla, B. Driehuys, L. W. Hedlund, and G. A. Johnson, *J. Magn. Reson.* **135,** 133–143 (1998).

211. A. J. Deninger, B. Eberle, M. Ebert, T. Großmann, W. Heil, H. U. Kauczor, L. Lauer, K. Markstaller, E. Otten, J. Schmiedeskamp, W. Schreiber, R. Surkau, M. Thelen, and N. Weiler, *J. Magn. Reson.* **141,** 207–216 (1999).

212. R. D. Black, H. L. Middleton, G. D. Cates, G. P. Cofer, B. Driehuys, W. Happer, L. W. Hedlund, G. A. Johnson, M. D. Shattuck, and J. C. Swartz, *Radiology* **199,** 867–870 (1996).

213. K. Sakai, A. M. Bilek, E. Oteiza, R. L. Walsworth, D. Balamore, F. Jolesz, and M. S. Albert, *J. Magn. Reson. B* **111,** 300–304 (1996).

214. M. E. Wagshul, T. M. Button, H. F. F. Li, Z. R. Liang, C. S. Springer, Jr., K. Zhong, and A. Wishnia, *Magn. Reson. Med.* **36,** 183–191 (1996).

215. G. A. Johnson, G. Cates, X. J. Chen, C. P. Cofer, B. Driehuys, W. Happer, L. W. Hedlund, B. Saam, M. D. Shattuck, and J. Swartz, *Magn. Reson. Med.* **38,** 66–71 (1997).

216. X. L. Chen, M. S. Chawla, G. P. Cofer, L. W. Hedlund, H. E. Möller, and G. A. Johnson, *Magn. Reson. Med.* **40,** 61–65 (1998).

217. H. E. Moller, X. J. Chen, M. S. Chawla, G. P. Cofer, B. Driehuys, L. W. Hedlund, S. A. Suddarth, and G. A. Johnson, *Magn. Reson. Med.* **41,** 800–808 (1999).

218. M. Viallon, G. P. Cofer, S. A. Suddarth, H. E. Moller, X. J. Chen, M. S. Chawla, L. W. Hedlund, Y. Cremillieux, and G. A. Johnson, *Magn. Reson. Med.* **41,** 787–792 (1999).

219. Y. Cremillieux, Y. Berthezene, H. Humblot, M. Viallon, E. Canet, M. Bourgeois, T. Albert, W. Heil, and A. Briguet. *Magn. Reson. Med.* **41,** 645–648 (1999).

220. X. J. Chen, H. E. Moller, M. S. Chawla, G. P. Cofer, B. Driehuys, L. W. Hedlund, J. R. MacFall, and G. A. Johnson, *Magn. Reson. Med.* **42,** 729–737 (1999).

221. X. J. Chen, H. E. Moller, M. S. Chawla, G. P. Cofer, B. Driehuys, L. W. Hedlund, and G. A. Johnson, *Magn. Reson. Med.* **42,** 721–728 (1999).

222. B. Eberle, N. Weiler, K. Markstaller, H. U. Kauczor, A. Deniger, M. Ebert, T. Großmann, W. Heil, L. O. Lauer, T. P. L. Roberts, W. G. Schreiber, R. Surkau, W. F. Dick, E. W. Otten, and M. Thelen, *J. Appl. Physiol.* **87,** 2043–2052 (1999).

223. P. Bachert, L. R. Schad, M. Bock, M. V. Knopp, M. Ebert, T. Großmann, W. Heil, D. Hofmann, E. W. Otten, R. Surkau, G. van Kaick, and W. J. Lorenz, *J. Nucl. Med.* **37,** 1320 (1996).

224. J. R. Macfall, H. C. Charles, R. D. Black, H. Middleton, J. C. Swartz, B. Saam, B. Driehuys, C. Erickson, W. Happer, G. D. Cates, G. A. Johnson, and C. E. Ravin, *Radiology* **200,** 553–558 (1996).

225. M. Ebert, T. Großmann, W. Heil, W. E. Otten, R. Surkau, M. Leduc, P. Bachert, M. V. Knopp, L. R. Schad, and M. Thelen, *Lancet* **347,** 1297–1299 (1996).

226. P. Bachert, L. R. Schad, M. Bock, M. V. Knopp, M. Ebert, T. Großmann, W. Heil, D. Hofmann, R. Surkau, and E. W. Otten, *Magn. Reson. Med.* **36,** 192–196 (1996).

227. H. U. Kauczor, D. Hofmann, K. F. Kreitner, H. Nilgens, R. Surkau, W. Heil, A. Potthast, M. V. Knopp, E. W. Otten, and M. Thelen, *Radiology* **201,** 564–568 (1996).

228. J. P. Mugler, III, B. Driehuys, J. R. Brookeman, G. D. Cates, S. S. Berr, R. G. Bryant, T. M. Daniel, E. E. del Lange, J. H. Downs, III, C. J. Erickson, W. Happer, D. P. Hinton, N. F. Kassel, T. Maier, C. D. Phillips, B. T. Saam, K. L. Sauer, and M. E. Wagshul, *Magn. Reson. Med.* **37,** 809–815 (1997).

229. X. J. Chen, M. S. Chawla, L. W. Hedlund, H. E. Möller, J. R. MacFall, and G. A. Johnson, *Magn. Reson. Med.* **39,** 79–84 (1998).

230. E. E. de Lange, J. P. Mugler, J. R. Brookeman, J. Knight-Scott, J. D. Truwit, C. D. Teates, T. M. Daniel, P. L. Bogorad, and G. D. Cates, *Radiology* **210,** 851–857 (1999).

231. B. Saam, D. A. Yablonskiy, D. S. Gierada, and M. S. Conradi, *Magn. Reson. Med.* **42,** 507–514 (1999); respiration ciné loop is available or viewing at www.physics.wustl.edu/saam/hemri.htm.

232. L. F. Donnelly, J. R. MacFall, H. P. McAdams, J. M. Majure, J. Smith, D. P. Frush, P. Bogorad, H. C. Charles, and C. E. Ravin, *Radiology* **212,** 885–889 (1999).

233. C. D. Teates, J. R. Brookeman, T. M. Daniel, J. D. Truwit, J. S. Parekh, J. P. Mugler, and E. de Lange, *Clin. Nucl. Med.* **24,** 747–750 (1999).

234. H. P. McAdams, S. M. Palmer, L. E. Donnelly, H. C. Charles, V. F. Tapson, and J. R. MacFall, *Am. J. Roentgenol.* **173,** 955–959 (1999).

235. E. E. de Lange, J. P. Mugler, III, J. R. Brookeman, J. Knight-Scott, J. D. Truwit, C. D. Teates, T. M. Daniel, P. L. Bogorad, and G. D. Cates, *Radiology* **210,** 851–857 (1999).

236. M. S. Albert, C. H. Tseng, D. Williamson, E. R. Oteiza, R. L. Walsworth, B. Kraft, D. Kacher, B. L. Holman, and F. A. Jolesz, *J. Magn. Reson. B* **111,** 204–207 (1996).

237. R. R. Rizi, I. E. Dimitrov, A. Thompson, G. Jones, T. R. Gentile, M. Ishii, R. Reddy, M. D. Schnall, and J. S. Leigh, *Magn. Reson. Med.* **39,** 865–868 (1998).

238. C. D. Phillips, J. H. Goldstein, J. R. Brookeman, J. P. Mugler, and T. Maier, *Riv. Neuroradiol.* **12,** 183–185 (1999).

239. M. D. Shattuck, S. L. Gewalt, G. H. Glover, L. W. Hedlund, and G. A. Johnson, *Magn. Reson. Med.* **38,** 938–942 (1997).

240. M. S. Albert, V. D. Schepkin, and T. F. Budinger, *J. Comput. Assisted Tomogr.* **19,** 975–978 (1995).

241. A. Bifone, Y.-Q. Song, R. Seydoux, R. E. Taylor, B. M. Goodson, T. Pietraß, T. F. Budinger, G. Navon, and A. Pines, *Proc. Natl. Acad. Sci. U.S.A.* **93,** 12932–12936 (1996).

242. H. Weingartner, R. Haselmeier, and M. Holz, *Chem. Phys. Lett.* **195,** 596–601 (1992).

243. J. B. West, "Respiratory Physiology," Williams & Wilkins, Baltimore (1995).

244. C. H. Tseng, S. Peled, L. Nascimben, E. Oteiza, R. L. Walsworth, and F. A. Jolesz, *J. Magn. Reson.* **126,** 79–86 (1997).

245. M. S. Albert, D. F. Kacher, D. Balamore, A. K. Venkatesh, and F. A. Jolesz, *J. Magn. Reson.* **140,** 264–273 (1999).

246. M. F. Perutz, *Nature* **228,** 726–739 (1970).

247. J. Wolber, A. Cherubini, M. O. Leach, and A. Bifone, *Magn. Reson. Med.* **43,** 491–496 (2000).

248. K. R. Thulborn, J. C. Waterton, P. M. Matthews, and G. K. Radda, *Biochim. Biophys. Acta* **714,** 265–270 (1982).

249. R. Turner, D. Le-Bihan, C. T. W. Moonen, D. Despres, and J. Frank, *Magn. Reson. Med.* **22,** 159–166 (1991).

250. S. J. Ogawa, D. W. Tank, R. Menon, J. M. Ellemann, S. G. Kim, H. Merkle, and K. Ugurbil, *Proc. Natl. Acad. Sci. U.S.A.* **89,** 5951–5955 (1992).

251. S. D. Swanson, M. S. Rosen, B. W. Agranoff, K. P. Coulter, R. C. Welsh, and T. E. Chupp, *Magn. Reson. Med.* **38,** 695–698 (1997).

252. R. C. Welsh, T. E. Chupp, K. P. Coulter, M. S. Rosen, S. D. Swanson, and B. W. Agranoff, *Nucl. Instrum. Methods Phys. Res. A* **402,** 461–463 (1998).

253. S. D. Swanson, M. S. Rosen, K. P. Coulter, R. C. Welsh, and T. E. Chupp, *Magn. Reson. Med.* **42,** 1137–1145 (1999).

254. J. Wolber, I. J. Rowland, M. O. Leach, and A. Bifone, *Appl. Magn. Reson.* **15,** 343–352 (1998).

255. S. Peled, F. A. Jolesz, C. H. Tseng, L. Nascimben, M. S. Albert, and R. L. Walsworth, *Magn. Reson. Med.* **36,** 340–344 (1996).

256. C. C. Martin, R. F. Williams, J.-H. Gao, L. D. H. Nickerson, J. Xiong, and P. T. Fox, *J. Magn. Reson. Imag.* **7,** 848–854 (1997); an interactive Web site containing a xenon respiration model can be found at http://ric.uthscsa.edu/staff/charlesmartinphd.html.

257. B. M. Goodson, Y.-Q. Song, R. E. Taylor, V. D. Schepkin, K. M. Brennan, G. C. Chingas, T. F. Budinger, G. Navon, and A. Pines, *Proc. Natl. Acad. Sci. U.S.A.* **94,** 14725–14729 (1997).

258. N. A. Lassen, J. Lindbjerg, and O. Munck, *Lancet* **1,** 686–689 (1964).

259. R. V. Pozderac, T. A. Miller, and S. M. Lindenauer, *Radiology* **117,** 633–635 (1975).

260. R. Y. Z. Chen, F.-C. Fan, S. Kim, K.-M. Jan, S. Usami, and S. Chien, *J. Appl. Physiol.* **49,** 178–183 (1980).

261. L. Zhao, A. Venkatesh, D. Balamore, F. A. Jolesz, and M. S. Albert, *in* "Proc. ISMRM, 6th Scientific Meeting, Sydney, 1998."

262. D. Beauregard, *Chem. Ind.* **12,** 459–460 (1995).

263. J. Wolber, I. J. Rowland, M. O. Leach, and A. Bifone, *Magn. Reson. Med.* **41,** 442–449 (1999).

264. J. Wolber, I. J. Rowland, T. Prock, D. J. Collins, G. S. Payne, M. O. Leach, and A. Bifone, *in* "Proc. ISMRM, 6th Scientific Meeting, Sydney, 1998."

265. A. Venkatesh, L. Zhao, D. Balamore, F. A. Jolesz, and M. S. Albert, *in* "Proc. ISMRM, 6th Scientific Meeting, Sydney, 1998."

266. M. S. Chawla, X. J. Chen, H. E. Möller, G. P. Cofer, C. T. Wheeler, L. W. Hedlund, and G. A. Johnson, *Proc. Natl. Acad. Sci. U.S.A.* **95,** 10832–10835 (1998).

267. M. S. Chawla, X. J. Chen, G. P. Cofer, L. W. Hedlund, M. B. Kerby, T. B. Ottoboni, and G. A. Johnson, *Magn. Reson. Med.* **43,** 440–445 (2000).

268. H. L. Clever, (Ed.), "Krypton, Xenon and Radon—Gas Solubilities, Vol. 2," Pergamon, Oxford (1979).

269. T. R. Stengle, N. V. Reo, and K. L. Williamson, *J. Phys. Chem.* **88,** 3225–3228 (1984).

270. H. E. Möller, M. S. Chawla, X. J. Chen, B. Driehuys, K. C. Hasson, L. W. Hedlund, C. T. Wheeler, and G. A. Johnson, *in* "Proc. ISMRM, 6th Scientific Meeting, Sydney, 1998."

271. H. E. Möller, M. S. Chawla, X. J. Chen, B. Driehuys, L. W. Hedlund, C. T. Wheeler, and G. A. Johnson, *Magn. Reson. Med.* **41,** 1058–1064 (1999).

272. G. L. Pollack, R. P. Kennan, and G. T. Holm, *Biomat. Artif. Cell. Im.* **20,** 1101–1104 (1992).

273. E. C. Greene, "Anatomy of the Rat," Hafner, New York (1963).

274. D. Raftery, H. W. Long, D. Shykind, P. J. Grandinetti, and A. Pines, *Phys. Rev. A* **50,** 567–574 (1994).

275. L. Darrasse, G. Guillot, P. J. Nacher, and G. Tastevin, *C.R. Acad. Sci. IIB* **324,** 691–700 (1997).

276. E. Durand, G. Guillot, L. Darrasse, G. Tastevin, P. J. Nacher, A. Vignaud, D. Vattolo, and J. Bittoun, *Magn. Reson. Med.* **47,** 75–81 (2002).

277. C. H. Tseng, G. P. Wong, V. R. Pomeroy, R. W. Mair, D. P. Hinton, D. Hoffmann, R. E. Stoner, F. W. Hersman, D. G. Cory, and R. L. Walsworth, 1998.

278. J. Clarke, *in* "SQUID Sensors: Fundamentals, Fabrication and Applications" (H. Weinstock, Ed.), pp. 1–62, Kluwer Academic, Dordrecht, 1996.

279. D. M. TonThat, M. Ziegeweid, Y.-Q. Song, E. J. Munson, S. Appelt, A. Pines, and J. Clarke, *Chem. Phys. Lett.* **272,** 245–249 (1997).

280. M. P. Augustine, A. Wong-Foy, J. L. Yarger, M. Tomaselli, A. Pines, D. M. TonThat, and J. Clarke, *Appl. Phys. Lett.* **72,** 1908–1910 (1998).

281. K. Schlenga, R. F. McDermott, J. Clarke, R. E. de Souza, A. Wong-Foy, and A. Pines, *IEEE Trans. Appl. Supercond.* **9,** 4424–4427 (1999).